

Master's Thesis

# Shot Noise Measurements in High-Power Modelocked Thin-Disk Lasers



Marcel Köberlin

Ultrafast Laser Physics Group  
ETH Zürich

Supervision: Moritz Seidel, Dr. Christopher Phillips

Supervising Professor: Prof. Dr. Ursula Keller

Date: September 16, 2024

Ultrafast Laser Physics



# Abstract

This thesis presents the design, construction, and characterization of a mode-locked thin disk laser (TDL) with an average output power of 60 W, a pulse duration of 1030 fs, and a repetition rate of 20 MHz. Mode-locking is achieved using a sapphire-bonded SESAM, and beam stabilization is implemented with a two-actuator, two-detector system, reducing beam position fluctuations significantly. The stabilized laser is input to a hollow-core photonic crystal fibre (HCPCF). This results in a fibre coupling efficiency of 82% at 36 W input power.

Simulations of spectral broadening in the fibre are conducted, incorporating fluctuations in average output power and pressure-dependent nonlinear refractive indices, predicting a noise gain peak of 35 dBc and a spectral broadening of 25 nm FWHM. A grating spectrometer is also designed and built to achieve a wavelength resolution of up to half a nanometer. Two silicon photodiodes are characterized, and a comprehensive noise characterization is performed, measuring shot noise at -162 dBc/Hz, limited by the photodiode.

Due to a gas leak in the pressure system, final noise measurements could not be completed, but steps for future work are clearly outlined. After repairs and final measurements are conducted, the project sets the stage for further exploration, potentially achieving a record-low shot noise level of -197 dBc/Hz.

# Contents

---

Chapter 1	<b>Introduction</b>	1
Chapter 2	<b>Theory</b>	5
2.1	Soliton modelocking	5
2.2	Saturable Absorbers and Passive Modelocking	8
2.3	Power Spectral Density, Relative Intensity Noise, and Signal-to-Noise Ratio	10
2.4	Noise of Mode-Locked Lasers	13
2.5	Shot Noise in Lasers	15
2.6	Influence of spectral broadening on noise	16
Chapter 3	<b>Setup, Characterization and Results</b>	26
3.1	Oscillator	26
3.2	Beam Diagnostics	30
3.3	Fibre Coupling	33
3.4	Grating Spectrometer	37
3.5	Characterization	39
3.6	Technical Considerations	53
Chapter 4	<b>Conclusion and Outlook</b>	60
	<b>Acknowledgements</b>	62
	<b>Bibliography</b>	66
	<b>Appendix</b>	67

# CHAPTER 1

# Introduction

---

## History of Lasers and Modelocking

The history of laser technology began with the groundbreaking theories proposed by Albert Einstein in the early 20th century on stimulated emission, which laid the foundational principles of laser physics [1]. The practical realization of these theories began with Theodore Maiman's creation of the first ruby laser in 1960 [2]. Since then, lasers have revolutionized numerous fields [3], from communication and medicine to manufacturing and scientific research. The evolution of lasers has been characterized by significant breakthroughs, particularly in the domain of pulse generation techniques such as modelocking. Introduced in the 1960s [4], modelocking has enabled a new realm of precision and control in various applications, including spectroscopy, material processing, and medical diagnostics [5]–[7].

## The Rise of Thin-Disk Lasers

In the realm of high-power laser applications, thin-disk lasers (TDLs) have emerged as a prominent solution due to their unique design and operational advantages. Traditional laser amplification chains, while effective, often face challenges such as non-linear effects, pulse distortion, and system complexity. These chains start with low-power oscillators whose output passes through amplifiers to achieve high-power levels. Common amplifier systems include fibre amplifiers [8], slab amplifiers [9], and thin-disk amplifiers [10]. However, amplifiers introduce additional noise sources, such as amplified spontaneous emission (ASE).

In contrast, TDLs maintain excellent beam quality while effectively dissipating heat, even at high power levels [11], [12]. They achieve high output power directly from the oscillator without amplifiers, making TDLs highly suitable for applications requiring high power and precision, such as material processing [13], medical procedures [14], and scientific research, particularly in high-harmonic generation [15]. Low noise at MHz repetition rates is essential for specific applications, such as pump-probe measurements requiring low noise and a high

signal-to-noise ratio. Another application of high-power oscillators is frequency-conversion at MHz repetition rates, for example, generating attosecond pulses at MHz repetition rates.

### Noise in different architectures

The noise characteristics of high-power laser systems depend significantly on whether a high-power oscillator or a master oscillator power amplifier (MOPA) system is used. In the typical MOPA concept, a low-power oscillator is combined with an amplifier. Here, the initial oscillator shot noise fundamentally limits the system noise. However, amplifiers can also add significantly more noise above the initial shot noise.

As done in this thesis, one must start with a high-power oscillator to achieve the theoretically lowest shot noise. However, not all oscillator architectures support shot-noise-limited performance; in particular, there is a distinction between two competing well-established architectures: Fibre and solid-state. Fibre laser oscillators can typically only provide very limited output power and thus must be combined with an amplifier to achieve meaningful powers ( $> 1 \text{ W}$ ). However, this system cannot reach shot-noise-limited performance because of the high contribution to the noise from amplified spontaneous emission (ASE) from the system's geometry. Furthermore, reabsorption effects in high-power amplifiers can also play a role in further deteriorating noise performance [16].

Solid-state lasers can be built as a high-power oscillator (typically with thin-disk lasers, as done here) or with an amplifier system. Several noise contributions are present here [17], but typically do not outweigh the shot-noise at high frequencies. Therefore, these lasers are shot-noise limited and thus have an architectural advantage over fibre laser systems. The reason ASE does not play an important role here is due to the shorter gain interaction length and less guiding of the spontaneous emission than in fibre lasers. While one needs to be more careful in designing these solid-state systems well in regard to mechanical noise, the ultimate limit is only the shot noise of the solid-state oscillator used.

### Final Goal of This Thesis

The primary objective of this thesis is to demonstrate that high-power oscillators can achieve the lowest shot noise limit among high-power lasers by avoiding amplifiers. To achieve this, we employ a nonlinear process using a hollow-core gas-filled fibre at high pressure. This strong spectral broadening allows us to infer noise levels that are below the detection threshold of conventional instruments. The key to this approach is that small fluctuations in oscillator power inherently induce significant variations in the broadened spectrum, resulting in a substantial noise gain.

The current record for the lowest measured shot noise level is -183 dBc/Hz, achieved by using photodetection in reflection in combination with optical ac coupling [18]. We aim to infer a shot noise level of -191 dBc/Hz, potentially setting a new benchmark for noise measurement in high-power lasers. This advances us closer to the anticipated true shot noise level of the oscillator, estimated at around -202 dBc/Hz.

## The Structure of the Thesis

The thesis is organized as follows:

Chapter 2 presents the theoretical framework essential for this research. It begins with an in-depth explanation of soliton mode-locking, starting from the nonlinear Schrödinger equation. A refresher on key concepts such as power spectral densities, relative intensity noise, and signal-to-noise ratio is provided. This chapter also includes an examination of shot noise in lasers and the theory behind spectral broadening, along with its simulation methods.

Chapter 3 describes the design and characterization of the TDL cavity, including its stability and the rationale behind various design choices. The characterization process is detailed, covering beam diagnostics, power slope measurements, and noise characterization. The chapter also explains fibre coupling techniques, such as beam stabilization, power tuning, and polarization control. Additionally, the design and analysis of the grating spectrometer's spectral resolution are discussed. The methodology for obtaining accurate noise measurements is presented, with an emphasis on signal processing techniques.

Chapter 4 concludes the thesis by summarizing the key findings, outlining the contributions of this research, and suggesting potential directions for future studies.

# CHAPTER 2

# Theory

---

## 2.1 Soliton modelocking

Soliton modelocking is a frequently used method to produce ultrashort pulses utilizing the formation of solitons [19]. When the effects of self-phase modulation (SPM) and negative group delay dispersion (GDD) balance out, a soliton pulse is formed, which can propagate without pulse or spectral broadening in a dispersive medium [6]. Since SPM depends on peak power, while GDD does not, variations in pulse length lead to the automatic formation of a stable solution. This inherent stability makes solitons robust against distortions.

The starting point for any discussion on solitons is that they are the fundamental solution to the **nonlinear Schrödinger equation** (NLSE)

$$\frac{\partial}{\partial z} A(z, \tau) = i \frac{k_n''}{2} \frac{\partial^2}{\partial \tau^2} A(z, \tau) - ikn_2 |A(z, \tau)|^2 A(z, \tau) \quad (2.1)$$

where  $k_n'' = \frac{\partial^2 k_n}{\partial \omega^2}$  is the second-order dispersion,  $\tau = t - \frac{z}{v_g}$  the retarded time with  $v_g = \frac{\partial \omega}{\partial k_n}$  the group velocity, which is generally frequency-dependent.

The fundamental soliton has the form

$$A_S(z, \tau) = A_0 \cdot \operatorname{sech} \left( \frac{t}{\tau} \right) e^{-i\phi_0(z)}, \quad (2.2)$$

with  $\phi_0(z) = \frac{1}{2} kn_2 I_p z$  being the nonlinear phase shift and  $I_p$  the peak intensity. The pulse length is given by

$$\tau = 2 \frac{|k_n''|}{kn_2 F_p}, \quad (2.3)$$

where  $F_p$  is the pulse fluence. The full-width-at-half-maximum (FWHM) can then be obtained as  $\tau_p = 1.7627\tau$ . A soliton has a time-bandwidth product of  $\tau_p \Delta\omega_p = 0.3148$  with  $\Delta\omega_p$  being the FWHM of the Fourier transform [6].

Figures 2.1 and 2.2 compare the cases of negative and positive SPM, showing how positive GDD requires negative SPM to create a soliton.

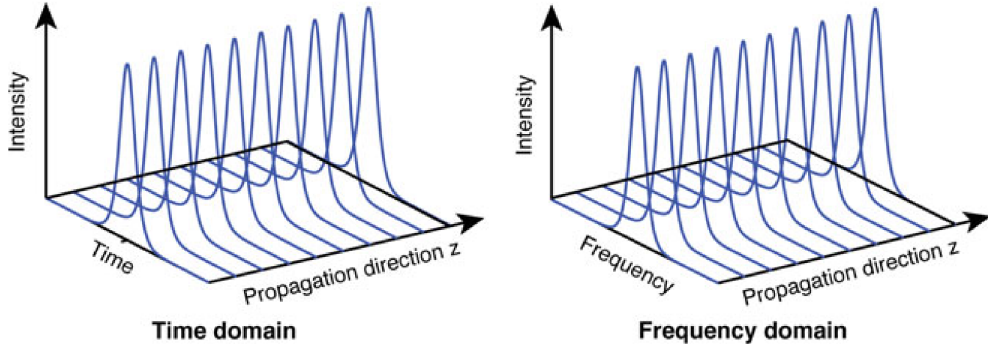


Figure 2.1: A soliton can only form if the SPM has the opposite sign of the GDD. In this case, positive GDD requires negative SPM for a stable wavepacket (a soliton) to form. The shape remains unchanged in the time and frequency domain [6].

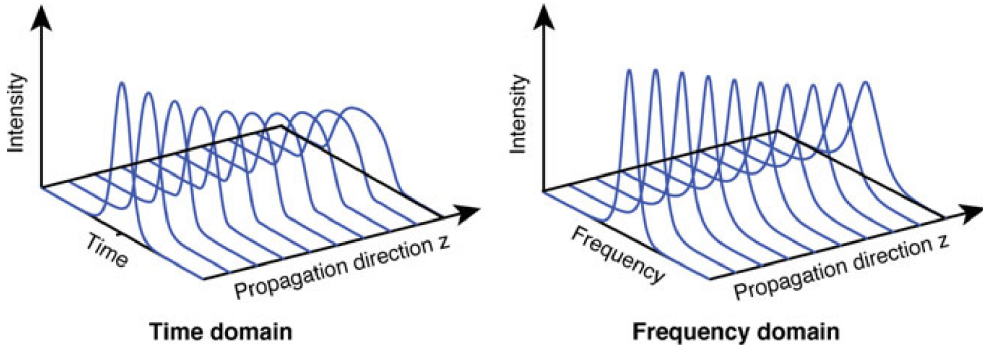


Figure 2.2: Positive SPM amplifies the broadening effect of the already positive GDD. A soliton cannot form, and the pulse will keep broadening [6].

It is important to note that the preceding discussion assumes a uniform distribution of SPM and GDD. However, in practice, this uniformity is not always maintained within the laser cavity. Consequently, the pulse shape is only fully restored after a complete roundtrip through the cavity. During this roundtrip, the pulse may deviate from its ideal form, leading to temporary distortions.

### Periodic Perturbations of Solitons

In lasers, solitons within the cavity are subjected to recurrent perturbations, for example, due to losses at the output coupler. This section delves into the ef-

fects of these periodic perturbations on solitons and closely follows the discussion in [6]. Consider a soliton experiencing periodic perturbations within a system, represented by:

$$i\xi \sum_{m=-\infty}^{\infty} \delta(z - mz_a) A(z, t), \quad (2.4)$$

where  $\xi \ll 1$  is a small perturbation coefficient and  $z_a$  is the periodicity of the perturbation. This model captures the essence of phenomena such as gain recovery in amplifiers or loss modulation in laser cavities.

From the nonlinear Schrödinger equation, incorporating the periodic perturbation gives:

$$\frac{\partial}{\partial z} A(z, t) = i\frac{\beta_2}{2} \frac{\partial^2}{\partial t^2} A(z, t) - i\gamma |A(z, t)|^2 A(z, t) + i\xi \sum_{m=-\infty}^{\infty} \delta(z - mz_a) A(z, t), \quad (2.5)$$

where  $\beta_2$  is the group velocity dispersion and  $\gamma$  is the nonlinear parameter.

For the analysis, we use the Ansatz:

$$A(z, t) = A_s(z, t) + u(z, t), \quad (2.6)$$

where  $A_s(z, t)$  is the unperturbed soliton solution, and  $u(z, t)$  represents the perturbation. Substituting this into the NLSE and linearizing, we obtain:

$$\frac{\partial}{\partial z} u(z, t) \approx i\frac{\beta_2}{2} \frac{\partial^2}{\partial t^2} u(z, t) + i\xi \sum_{m=-\infty}^{\infty} \delta(z - mz_a) A_s(z, t). \quad (2.7)$$

Neglecting higher-order terms, the equation simplifies under the assumption  $|u(z, t)| \ll |A_s(z, t)|$ .

The periodicity introduces the possibility of resonance, where the perturbation frequency aligns with the natural frequencies of the system, potentially leading to significant growth in the amplitude of  $u(z, t)$ . This is the case if

$$mk_a = \frac{|k''_n|}{2} \left( \frac{1}{\tau^2} + \omega_m^2 \right), \quad (2.8)$$

where  $k_a = \frac{2\pi}{z_a}$ . To avoid such resonance, it is crucial that the perturbation period  $z_a$  is much smaller than the soliton's characteristic length scale  $z_0$ , ensuring:

$$z_a \ll 8z_0. \quad (2.9)$$

Under this condition, the perturbation behaves almost as if it were continuous, allowing us to treat it with standard perturbation techniques.

## 2.2 Saturable Absorbers and Passive Modelocking

Until now, modelocking has been primarily explained through the nonlinear Schrödinger equation, highlighting the balancing effects of group delay dispersion and self-phase modulation. While the NLSE provides a powerful framework for understanding the formation and stability of soliton pulses, it does not fully capture all aspects of the laser dynamics. For example, the influence of gain, loss, and the initial pulse formation within the laser cavity are not addressed. In this section, passive modelocking is described from the perspective of saturable absorbers, such as the SESAM, with a particular focus on the formation of pulses.

The primary function of a saturable absorber (SA) is to implement self-amplitude modulation (SAM): it induces high losses for low-intensity light and low losses for high-intensity light [6]. This results in loss modulation, as the pulse peak saturates the absorber more strongly than its wings. The starting point is the equation for the saturable loss coefficient:

$$\frac{dq}{dt} = -\frac{q(t) - q_0}{\tau_A} - q(t) \frac{P(t)}{E_{\text{sat},A}}, \quad (2.10)$$

where  $\tau_A$  is the recovery time of the saturable absorber, indicating how long it takes for the losses to return to high values after the SA has been saturated, and  $P(t)$  is the pulse shape. The SESAM used in this thesis has a recovery time of 9 ps, classifying it as a slow saturable absorber since  $\tau_p \ll \tau_A$ . This allows the neglect of recovery during the pulse duration. It can be shown [6] that the saturable loss coefficient becomes

$$q(t) = q_0 \exp \left( -\frac{E_P}{E_{\text{sat},A}} \int_0^t dt' f(t') \right), \quad (2.11)$$

where  $f(t)$  is a function normalized to 1 over the roundtrip time. In this formulation,  $q(t)$  is independent of the pulse length, and it can further be shown that the total loss of a pulse passing through the absorber is independent of the pulse shape:

$$q_p(E_P) = \int_0^{T_R} q(t) f(t) dt. \quad (2.12)$$

In discussing passive modelocking, three cases are typically distinguished: (1) A slow saturable absorber with dynamic gain saturation, (2) a fast saturable absorber, or (3) a slow saturable absorber with no dynamic gain saturation. The last case is commonly referred to as soliton modelocking. The SESAM in this thesis operates in this regime as a slow, saturable absorber. To account for aspects such as gain and loss, the starting point is the *Haus Master equation* [20]:

$$T_R \frac{\partial A(T, t)}{\partial T} = \sum \Delta A_i = 0, \quad (2.13)$$

which holds at steady-state over a "long" timescale  $T$ , encompassing many roundtrips. The linearized operators  $\Delta A_i$  represent changes due to gain, loss, and constant loss (such as output coupler losses). This description is valid for small changes per roundtrip, implying that the sum of changes balances out. By incorporating linearized operators for SPM and GDD, it is unsurprising that the solution to this equation is again a soliton pulse. However, the solution can be written in a slightly different form:

$$A(t) = A_0 \operatorname{sech} \left( \frac{t}{\tau} \right) e^{i\phi_0 T/T_R} + \text{continuum.} \quad (2.14)$$

Here, the continuum refers to a weak and temporally spread-out pulse, as depicted in Figure 2.3.

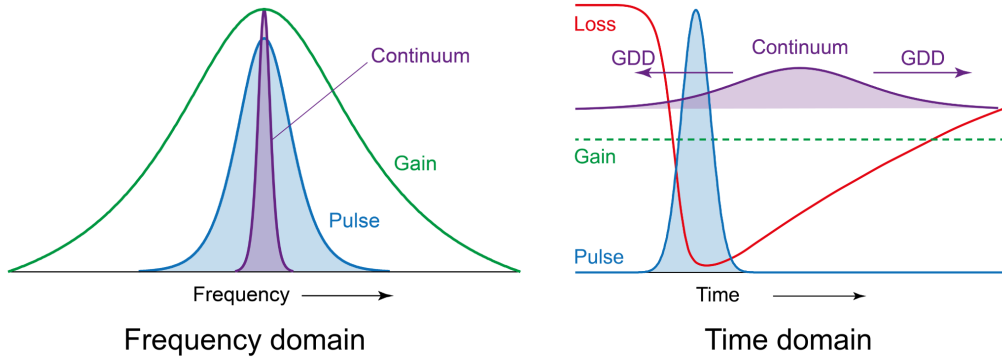


Figure 2.3: Illustration of soliton modelocking with gain and loss dynamics. The main soliton pulse (left) is stabilized by the interplay of gain and saturable absorption, while a weak, temporally spread-out continuum (right) is suppressed due to low intensity and the absence of self-phase modulation (SPM). The slow saturable absorber prevents the continuum from reaching the gain threshold, thereby maintaining a stable pulse within the laser cavity.

Due to its low intensity, the continuum does not experience SPM, resulting in its spread over time due to GDD (as shown on the right side of Figure 2.3). Because it is spectrally narrow, it experiences high gain. The slow SA is still fast enough to ensure that the continuum experiences enhanced losses, preventing it from reaching the threshold where gain equals losses. This stabilization mechanism gradually removes the continuum or noise, thereby stabilizing the soliton pulse. This explains how passive modelocking produces stable pulses despite the presence of the continuum. Passive modelocking ideally starts from noise fluctuations within the laser, where a noise spike is amplified more than others until it reaches a steady state.

As mentioned, the SESAM used in this thesis is a slow, saturable absorber. Figure (2.4) depicts the reflectivity behaviour as a function of the incident fluence.

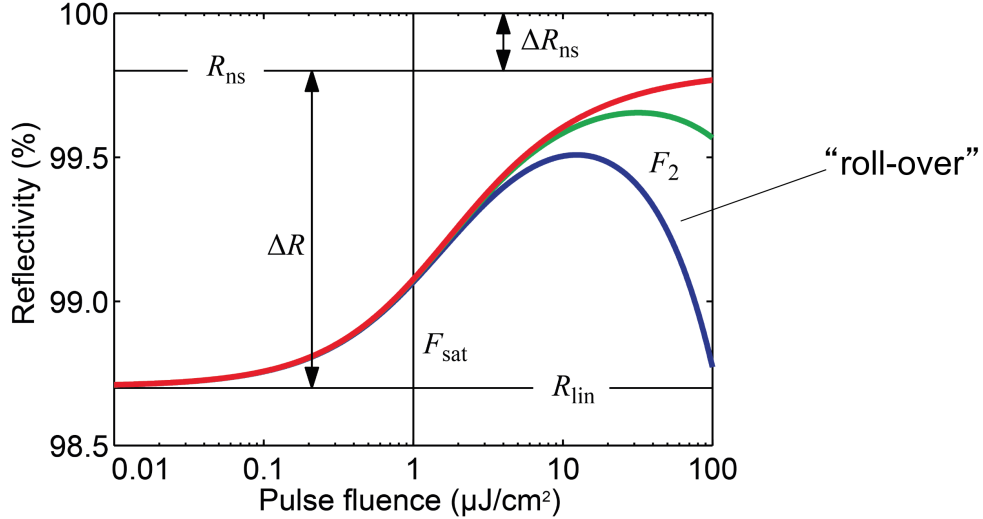


Figure 2.4: The characteristic reflectivity behaviour of a SESAM for three different values of inverse saturable absorption. [6]

As expected, the reflectivity initially increases with increasing fluence. However, eventually, the reflectivity decreases again due to second-order processes such as two-photon absorption. This leads to a rollover in the curve, typical of SESAMs, and is also called inverse saturable absorption.

### 2.3 Power Spectral Density, Relative Intensity Noise, and Signal-to-Noise Ratio

This section delves into several fundamental concepts essential to this thesis, including signal processing and optical communication: Power Spectral Density, Relative Intensity Noise and Signal-to-Noise Ratio. To avoid confusion between various notations, this thesis adheres to the IEEE standard on random instabilities [21].

#### Power Spectral Density

The power spectral density (PSD) is a measure of the power content distributed across different frequencies within a signal. To illustrate, consider a general signal  $x(t)$ , such as voltage as a function of time. We aim to understand how different frequencies contribute to its variance:

$$\text{Var}(x) = \langle x^2 \rangle - \langle x \rangle^2. \quad (2.15)$$

In the context of digital signal processing, the energy  $E$  of a continuous-time signal  $x(t)$  is defined as [22]

$$E = \int_{-\infty}^{\infty} |x(t)|^2 dt. \quad (2.16)$$

From *Parseval's theorem*, we further find that the energy in time is equal to the energy in frequency:

$$E = \int_{-\infty}^{\infty} |x(t)|^2 dt = \int_{-\infty}^{\infty} |\mathcal{F}(x)(f)|^2 df, \quad (2.17)$$

where  $\mathcal{F}(x)(f)$  denotes the Fourier transform of  $x(t)$ .

Therefore, power is simply energy divided by time:

$$P[x] = \langle x(t)^2 \rangle. \quad (2.18)$$

It is natural to define the energy spectral density as

$$E_x(f) = |\mathcal{F}(x)(f)|^2, \quad (2.19)$$

and consequently the (one-sided) power spectral density (PSD) as

$$S_x(f) = \lim_{T \rightarrow \infty} \frac{2}{T} |\mathcal{F}(x)(f)|^2 = \lim_{T \rightarrow \infty} \frac{2}{T} \left\langle \left| \int_{-T/2}^{T/2} x(t) e^{i2\pi f t} dt \right|^2 \right\rangle. \quad (2.20)$$

The units of PSD are  $[x]^2/\text{Hz}$ , implying power per unit bandwidth. Here, "power" does not necessarily refer to watts; for instance, in the context of voltage versus time, it denotes volts squared. Note that from now on, the PSD is always one-sided unless explicitly stated otherwise.

Another useful result comes from the *Wiener-Khinchin theorem*, stating that the power spectral density is the Fourier transform of the autocorrelation function  $\mathcal{R}_x(\tau) = \langle x(t)x(t+\tau) \rangle$ :

$$S_x(f) = 2 \int_{-\infty}^{\infty} \mathcal{R}_x(\tau) e^{-i2\pi f \tau} d\tau = 2\mathcal{F}(\mathcal{R}_x)(f). \quad (2.21)$$

By applying the Wiener-Khinchin theorem, we can utilize autocorrelation measurements—often more straightforward to obtain experimentally—to derive the PSD. This is particularly useful in intensity noise measurements, where the autocorrelation function of the laser's intensity fluctuations is recorded over time. By transforming this autocorrelation data using the Wiener-Khinchin theorem, we can determine the PSD of the noise.

## Relative Intensity Noise

Relative Intensity Noise (RIN) quantifies the intensity fluctuations of a signal relative to its mean intensity. For a signal  $x(t) = \bar{x} + \delta x(t)$ , where  $\delta x(t)$  represents fluctuations around the signal mean  $\bar{x}$ , RIN is commonly defined as [23]:

$$\text{RIN}_x(f) = \frac{2}{\bar{x}^2} \int_{-\infty}^{\infty} \langle \delta x(t) \delta x(t + \tau) \rangle e^{-i2\pi f \tau} d\tau = 2 \frac{\mathcal{F}(\mathcal{R}_{\delta x})(f)}{\bar{x}^2} = \frac{S_{\delta x}(f)}{\bar{x}^2}, \quad (2.22)$$

where the units are  $\text{Hz}^{-1}$ , and  $S_{\delta x}(f)$  refers to the Power Spectral Density of the fluctuations  $\delta x(t)$ .

The total PSD of the signal can be decomposed into the PSD of its mean and the PSD of its fluctuations:

$$S_x(f) = S_{\bar{x}}(f) + S_{\delta x}(f), \quad (2.23)$$

where  $S_{\bar{x}}(f)$  is the PSD of the mean. However, since the mean is constant,  $S_{\bar{x}}(f) = 0$  for all non-zero frequencies. Thus, for all practical purposes,  $S_x(f) \approx S_{\delta x}(f)$ . RIN is often expressed in logarithmic units as "decibels relative to the carrier" (dBc) per Hz, indicating how many decibels the noise is below the carrier level  $\bar{x}$ .

## Signal-to-Noise Ratio

The Signal-to-Noise Ratio (SNR) is a critical metric for evaluating the quality of a signal. It quantifies the ratio of the power of the signal to the power of background noise:

$$\text{SNR} = \frac{\bar{x}^2}{\sigma_x^2[f_1, f_2]}, \quad (2.24)$$

where  $\sigma_x^2[f_1, f_2]$  represents the variance of the signal's fluctuations, computed from the PSD across a specific frequency band  $[f_1, f_2]$ . Here, the measurement duration typically sets the lower frequency limit  $f_1$ , while the detection bandwidth determines the upper limit  $f_2$ .

It is essential to specify these frequency limits because the variance, or root mean square (RMS) value, of the signal's fluctuations  $\sqrt{\sigma_x^2}$ , is meaningful only within a defined frequency range. Therefore, defining the bandwidth is crucial for accurately assessing noise and, consequently, the SNR.

## 2.4 Noise of Mode-Locked Lasers

As this work primarily concerns noise, it is essential to discuss the noise characteristics of mode-locked lasers. When light intensity  $I(t)$  is detected by a photodetector. Ideally, it produces an electric current  $J(t) \sim I(t)$ , and a spectrum analyzer measures the power spectral density.

$$S_I(\omega) \sim |I(\omega)|^2 = \mathcal{F}(R_I(\tau)). \quad (2.25)$$

Therefore, the detector captures intensity noise originating from shot noise, Johnson (thermal) noise, and excess laser noise.

### Noiseless Mode-Locked Laser Intensity

We begin with the intensity of an ideal, noiseless mode-locked laser, which can be described by a delta-comb function:

$$I_{\text{ideal}}(t) = I_0 T_{\text{rep}} \sum_n \delta(t - nT_{\text{rep}}) \iff \tilde{I}_{\text{ideal}}(\omega) = 2\pi I_0 \sum_n \delta(\omega - n\omega_{\text{rep}}), \quad (2.26)$$

where  $\omega_{\text{rep}} = \frac{2\pi}{T_{\text{rep}}}$  is the repetition frequency, and  $T_{\text{rep}}$  is the round-trip time. Consequently, the PSD for the ideal case becomes:

$$\tilde{S}_{\text{ideal}}(\omega) = (2\pi I_0)^2 \sum_n \delta(\omega - n\omega_{\text{rep}}). \quad (2.27)$$

### Timing jitter

Any fluctuation in the optical path length results in timing jitter, as the repetition frequency is the inverse of the cavity round-trip time. Timing jitter  $\Delta T(t)$  can be mathematically described by:

$$\delta(t - nT_{\text{rep}}) \rightarrow \delta(t - nT_{\text{rep}} - \Delta T(t)), \quad (2.28)$$

which shifts the temporal position of each comb line. This transforms the PSD of the ideal comb into:

$$\tilde{S}_{\Delta T}(\omega) = (2\pi I_0 T_{\text{rep}})^2 \sum_n \left[ \delta(\omega - n\omega_{\text{rep}}) + \left( \frac{n\omega_{\text{rep}}}{2\pi} \right)^2 \Delta T^2(\omega - n\omega_{\text{rep}}) \right]. \quad (2.29)$$

The scaling goes as  $\sim n^2$ , indicating that timing jitter increases more dramatically for higher harmonics. The standard deviation of timing jitter is then given by:

$$\sigma_{\Delta T} = \sqrt{\langle \Delta T^2(t) \rangle} = \frac{1}{\pi} \sqrt{\int_0^\infty d\omega \tilde{S}_{\Delta T}(\omega)}. \quad (2.30)$$

When considering limits, we obtain:

$$\sigma_{\Delta T}[f_1, f_2] = \frac{1}{\pi} \sqrt{2 \int_{f_1}^{f_2} df \frac{P_{sb}^{(n)}(f)}{P_c^{(n)}(f)}}, \quad (2.31)$$

where the index *sb* stands for sideband and *c* for carrier. The superscript  $(n)$  denotes the  $n$ -th harmonic. Due to the  $n^2$  scaling, timing jitter has a more pronounced effect on higher harmonics, making them a crucial measurement point for accurately characterizing the jitter in mode-locked lasers. It's important to note that phase noise, which represents fluctuations in the phase of the comb lines, also contributes to timing jitter and is a key factor in determining the overall stability of the frequency comb.

### Intensity noise

Normalized intensity noise is a significant type of noise in mode-locked lasers. It's important to note that intensity noise and phase noise are often closely related, as the same underlying noise sources can induce both through coupling effects. Its effect changes the intensity as

$$I_0 \rightarrow I_0(1 + N(t)). \quad (2.32)$$

The corresponding PSD is:

$$\tilde{S}_N(\omega) = (2\pi I_0)^2 \sum_n \left[ \delta(\omega - n\omega_{rep}) + \tilde{N}^2(\omega - n\omega_{rep}) \right], \quad (2.33)$$

which, in contrast to timing jitter PSD, is independent of the harmonic order  $n$ . The standard deviation of intensity noise is:

$$\sigma_N = \sqrt{\langle N^2(t) \rangle} = \frac{1}{\pi} \sqrt{\int_0^\infty d\omega \tilde{S}_N(\omega)}. \quad (2.34)$$

However, it is crucial to note that calculating this standard deviation without specifying frequency boundaries is not just less meaningful—it is effectively

meaningless. The standard deviation must always be provided with well-defined frequency limits for accurate and practical measurements. This ensures that the noise characteristics are appropriately quantified and relevant to the specific application or measurement scenario:

$$\sigma_N[f_1, f_2] = \sqrt{\frac{P_{\text{sb}}[f_1, f_2]}{P_c}}, \quad (2.35)$$

where  $P_{\text{sb}}[f_1, f_2]$  is the power from the integration over the noise sidebands within the specified frequency boundaries.

## 2.5 Shot Noise in Lasers

Shot noise is a fundamental type of noise in electronic and optical devices, arising from the discrete nature of charge carriers (electrons) and light (photons). In lasers, shot noise is a consequence of the quantum statistical nature of photon emission. Although photon emission in lasers primarily occurs through stimulated emission, which leads to correlated emission events, the underlying processes are inherently probabilistic. The random nature of these processes, which follow a Poisson distribution, results in intrinsic fluctuations in the number of photons detected over a given interval. These fluctuations are inherent to the light itself, regardless of the stability of the light source.

For a photodiode detecting light, the photocurrent  $I(t)$  generated is proportional to the number of incident photons per unit of time. Assuming a constant average number of photons arriving per unit time, the resulting photocurrent will exhibit fluctuations due to the Poisson nature of photon arrival times. The root mean square (RMS) value of the shot noise current can be described by:

$$I_{\text{shot}} = \sqrt{2e\bar{I}\Delta f}, \quad (2.36)$$

where  $e$  is the elementary charge,  $\bar{I}$  is the average photocurrent, and  $\Delta f$  is the bandwidth of the measurement system.

According to Schottky's theorem [24], the power spectral density (PSD) of shot noise is given by:

$$S_{\text{shot}} = 2e\bar{I}, \quad (2.37)$$

which highlights the frequency independence of shot noise, classifying it as white noise. For a derivation of this theorem, please see the appendix (4). The PSD can also be related to the average optical power  $\bar{P}$ :

$$S_{\text{shot}} = 2\hbar\omega\bar{P}, \quad (2.38)$$

where  $\hbar$  is the reduced Planck's constant and  $\omega$  is the angular frequency of the light.

Using the definitions above, the Relative Intensity Noise for shot noise can be expressed as:

$$\text{RIN}_{\text{shot}} = \frac{2e}{\bar{I}} \quad \text{RIN}_{\text{shot}} = \frac{2\hbar\omega}{\bar{P}}. \quad (2.39)$$

From these results, we can deduce the following behaviour: Attenuating the laser output increases the relative intensity noise (RIN) due to shot noise. This is because reducing the power of a coherent beam makes quantum fluctuations more significant relative to the signal. Conversely, increasing the power reduces the relative impact of shot noise as the signal strength increases; however, this also increases the absolute level of shot noise due to the higher photon count. Additionally, increasing the bandwidth increases shot noise power, as more noise fluctuations are detected within the broader frequency range. Detector efficiency is also crucial: lower efficiency leads to fewer detected photons, which may reduce the absolute shot noise but increase the relative shot noise per detected signal, thereby degrading the signal-to-noise ratio.

While shot noise tends to dominate at high frequencies, the specific frequency at which this occurs can vary widely depending on the laser architecture, gain medium, and other factors. For instance, in solid-state lasers, shot noise may become significant at frequencies around 1 MHz or higher. In contrast, shot noise might dominate at much lower frequencies in other systems or may never become the dominant noise source, such as fibre lasers.

At lower frequencies, various other noise sources become significant, including relaxation oscillations, pump noise, thermal noise, and  $1/f$  noise. These sources contribute to the overall noise profile of the laser and can overshadow shot noise at these frequencies. To illustrate this effect, Figure 2.5 shows the RIN and timing noise of a SESAM mode-locked Ytterbium doped solid-state laser with a GHz repetition rate [25]. Relaxation oscillations can clearly be seen as a prominent peak, whereas the laser noise approaches the shot noise limit at higher frequencies.

A detector is said to be "shot noise-limited" when the predominant noise source affecting its performance is shot noise rather than thermal or electronic noise. In such systems, improving the SNR primarily involves increasing the optical power, as shot noise scales with the square root of power. In contrast, other types of noise may not follow this scaling. Achieving shot noise-limited performance is desirable in applications requiring high precision and sensitivity, such as quantum optics and spectroscopy.

## 2.6 Influence of spectral broadening on noise

Spectral broadening is a significant nonlinear optical effect utilized in various applications, such as supercontinuum generation [26], pulse compression [27], and potentially in enhancing noise measurement techniques. During spectral

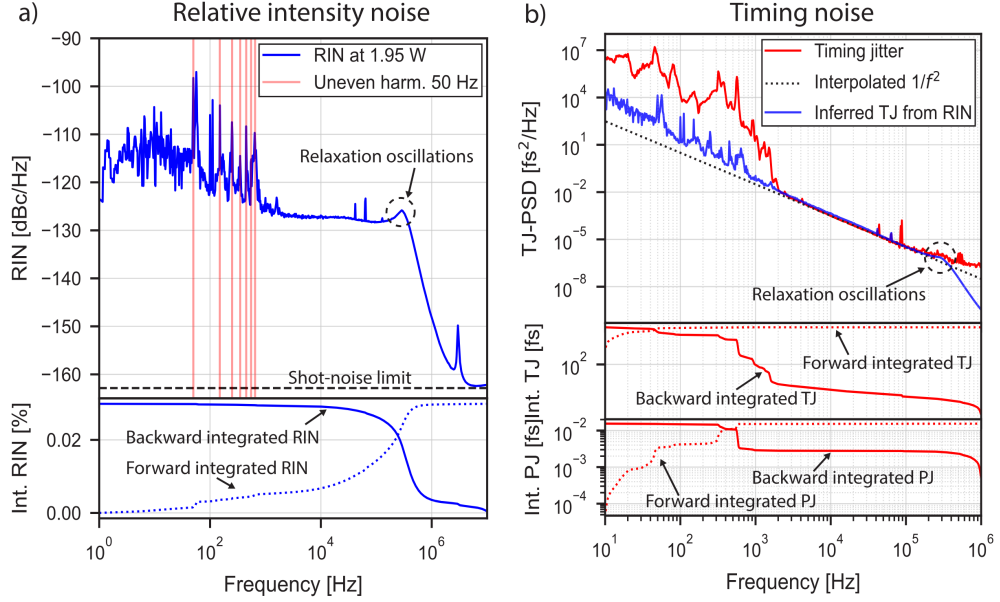


Figure 2.5: Relative intensity noise (RIN) and timing noise characteristics of a SESAM mode-locked Ytterbium-doped solid-state laser operating at a GHz repetition rate [25]. The figure illustrates various noise sources, with relaxation oscillations appearing as a prominent peak at lower frequencies. At higher frequencies, the noise level approaches the shot noise limit, indicating the dominance of quantum noise in this region.

broadening, noise is influenced: In the frequency range where shot noise is the dominant noise source of the unbroadened laser system, spectral broadening can cause an increase in the noise PSD.

This chapter explores the potential of using spectral broadening to influence noise, particularly emphasising the Kerr effect in high-pressure Xenon gas-filled hollow-core fibres. While not traditionally associated with noise measurement, this approach offers a novel perspective on how nonlinear effects can interact with and potentially manage different noise contributions in optical systems.

## The Optical Kerr Effect

The optical Kerr effect [28] causes the refractive index of a material to become intensity-dependent. To the first order, this can be expressed as:

$$n(I) = n + n_2 I, \quad (2.40)$$

where  $n_2$  is the nonlinear refractive index coefficient, typically [29] of the order of  $10^{-16} \text{ cm}^2/\text{W}$ , making this effect observable only at high intensities. This leads

to a nonlinear phase shift:

$$\varphi(t) = k_n n(I)L = k_n nL + \delta I(t), \quad (2.41)$$

with  $\delta = k_n n_2 L$  being the self-phase modulation coefficient. Consequently, the instantaneous frequency becomes non-zero:

$$\omega(t) = \frac{d\varphi}{dt} = \delta \frac{dI}{dt}, \quad (2.42)$$

indicating that SPM broadens the bandwidth of a pulse. In the leading edge of the pulse, where  $\frac{dI}{dt} > 0$ , lower frequencies are generated, and on the trailing edge, higher frequencies are produced. This phenomenon does not occur in linear optics and is intrinsic to nonlinear effects.

Various methods exist for spectral broadening, such as the previously discussed self-phase modulation resulting from intensity-dependent phase shifts. Additionally, cross-phase modulation, four-wave mixing, Raman scattering, and supercontinuum generation are significant contributors to spectral broadening, thoroughly detailed in [30]. Spectral broadening has applications in optical communication, metrology, and microscopy, among other fields.

### 2.6.1 Simulation

In the experiment, we utilize a high-power laser and high-pressure Xenon gas, chosen for its large [31], [32] nonlinear refractive index of  $n_2^{(\text{Xe})} = 8.1 \cdot 10^{-23} \text{ m}^2/\text{W}$ . This value is approximately six times larger than that of air or the noble gas Argon, both at  $n_2^{(\text{Ar, Air})} = 1.4 \cdot 10^{-23} \text{ m}^2/\text{W}$ . Additionally, since the nonlinear refractive index scales linearly with pressure [32], the effect becomes even more pronounced at high pressures, making Xenon an excellent choice for achieving strong spectral broadening. A method is required to propagate the laser light through a medium to simulate the spectral broadening. This needs to be done by solving the non-linear Schrödinger equation, which is not analytically solvable, however, there exists a powerful method to solve this problem numerically:

#### Laser Propagation in a Fibre: Split-Step Method

When analyzing the propagation of a laser pulse through an optical fibre, it is crucial to predict the output characteristics of the pulse, such as average power, pulse length, and spectral width, given specific input conditions. The nonlinear Schrödinger equation (NLSE) must be solved, which is inherently challenging due to its nonlinearity and complexity.

One of the most effective numerical techniques for solving the NLSE is the *Split-Step method*. This elegant approach allows the equation to be solved approximately by separating the linear and nonlinear components. This method

involves computing the solution in small steps, treating the linear and nonlinear effects alternately and independently. The linear propagation is performed in the frequency domain, while the nonlinear propagation is executed in the time domain, necessitating repeated Fourier transforms between these domains. The following description closely follows [30].

The starting point is the NLSE:

$$\frac{\partial A(z, \tau)}{\partial z} = i \frac{k_n''}{2} \frac{\partial^2 A(z, \tau)}{\partial \tau^2} - i k n_2 |A(z, \tau)|^2 A(z, \tau), \quad (2.43)$$

which can be rewritten in a more compact form as:

$$\frac{\partial A}{\partial z} = [\hat{L} + \hat{N}] A \quad \iff \quad A = \exp [\hat{L} + \hat{N}] A. \quad (2.44)$$

Here,  $\hat{L}$  represents the linear operator, while  $\hat{N}$  captures the nonlinear effects:

$$\frac{\partial A_L}{\partial z} = i \frac{k_n''}{2} \frac{\partial^2 A}{\partial t^2} = \hat{L} A, \quad \frac{\partial A_N}{\partial z} = -i k n_2 |A|^2 A = \hat{N} A. \quad (2.45)$$

Although the linear and nonlinear parts have analytical solutions when considered independently, the full NLSE does not. The critical assumption of the Split-Step method is that the optical field's dispersive and nonlinear effects can be treated separately when propagating a small distance  $h$ . This can be expressed as:

$$A(\tau, z + h) \approx \exp [h \hat{L}] \exp [h \hat{N}] A(z, \tau) \quad (2.46)$$

which is generally only true for commuting operators. The assumption is that the nonlinear part acts first, followed by the linear part. Due to the *Baker-Hausdorff formula*, this method is accurate to the second order in the step size  $h$ :

$$\exp(\hat{A}) \exp(\hat{B}) = \exp \left( \hat{A} + \hat{B} + \frac{1}{2} [\hat{A}, \hat{B}] + \frac{1}{12} [\hat{A} - \hat{B}, [\hat{A}, \hat{B}]] + \dots \right). \quad (2.47)$$

This can be seen by replacing  $\hat{A} \rightarrow h \hat{L}$  and  $\hat{B} \rightarrow h \hat{N}$ , such that the dominant error is  $\frac{1}{2} h^2 [\hat{L}, \hat{N}]$ . In the frequency domain, where  $\frac{\partial}{\partial t} \simeq -i(\omega - \omega_0)$ , the linear operator can be expressed as  $\hat{L}(\omega) = -i \frac{k_n''}{2} (\omega - \omega_0)^2$ , leading to the propagation step for the linear part:

$$\frac{\partial \tilde{A}_L}{\partial z} = -i \frac{k_n''}{2} (\omega - \omega_0)^2 A. \quad (2.48)$$

Thus, the linear propagation over a small step  $h$  is given by:

$$\tilde{A}_L(\omega, z + h) = e^{-i \frac{k_n''}{2} (\omega - \omega_0)^2 h} A(\omega, z). \quad (2.49)$$

By combining the linear and nonlinear propagation steps, we obtain the overall solution over a small distance  $h$ :

$$A(z + h, t) = \mathcal{F}^{-1} \left( e^{\hat{L}(\omega)h} \mathcal{F} \left( e^{\hat{N}h} A(z, t) \right) \right). \quad (2.50)$$

Iteratively applying this sequence allows the pulse to be propagated through the fibre.

### Simulation predictions

To understand how intensity fluctuations of the laser influence the spectral broadening, the output spectrum of the fibre at 100% of the laser's output power is compared with that at 100% plus small fluctuations. Since the shot noise of a TDL with an average output power of 60 W is expected to lie at around -210 dBc/Hz, the simulation ideally requires setting the fluctuation in average power to  $10^{-21}$ . However, at this precision level, computational limitations arise due to rounding errors. Consequently, the simulation was performed using a variation of  $10^{-10}$ , as no significant change in the spectrum was observed for fluctuations ranging from  $10^{-6}$  to  $10^{-12}$ . While a fluctuation of  $10^{-12}$  is still usable for most of the spectrum, the simulation fails in the spectral wings where the power density is low due to rounding errors. Henceforth, these small fluctuations will be referred to as (intensity) noise.

Moreover, since fluctuations in power also cause changes in pulse width and peak power, this effect should be considered in the simulation. Any approach should be consistent with the following equation:

$$\bar{P} = P_{\text{peak}}(\bar{P}) \cdot \tau_p(\bar{P}) \cdot f_{\text{rep}}, \quad (2.51)$$

where the dependence of peak power  $P_{\text{peak}}$  and pulse width  $\tau_p$  on the average power  $\bar{P}$  is explicitly highlighted. The simulation should be based on actual measurements rather than assumptions about the relationship between pulse width and average power to ensure it accurately reflects real-world behaviour. Therefore, the pulse width is measured as a function of average power using an autocorrelator (see Chapter 3.2), and the peak power is calculated using Eq. 2.51.

Figure 2.6 shows the measured pulse width for average laser output powers ranging from 34 W to 60 W. As the soliton pulse width follows the relationship [6]

$$\tau_p \sim \frac{1}{F_p} \sim \frac{1}{E_p} \sim \frac{1}{\bar{P}}, \quad (2.52)$$

where  $F_p$  is the pulse fluence, an inverse average power fit ( $1/P_{av}$ ) is applied across the range of 25 W to 60 W. This range corresponds to the operating conditions where the TDL is mode-locked without continuous wave (CW) breakthrough or other artefacts.

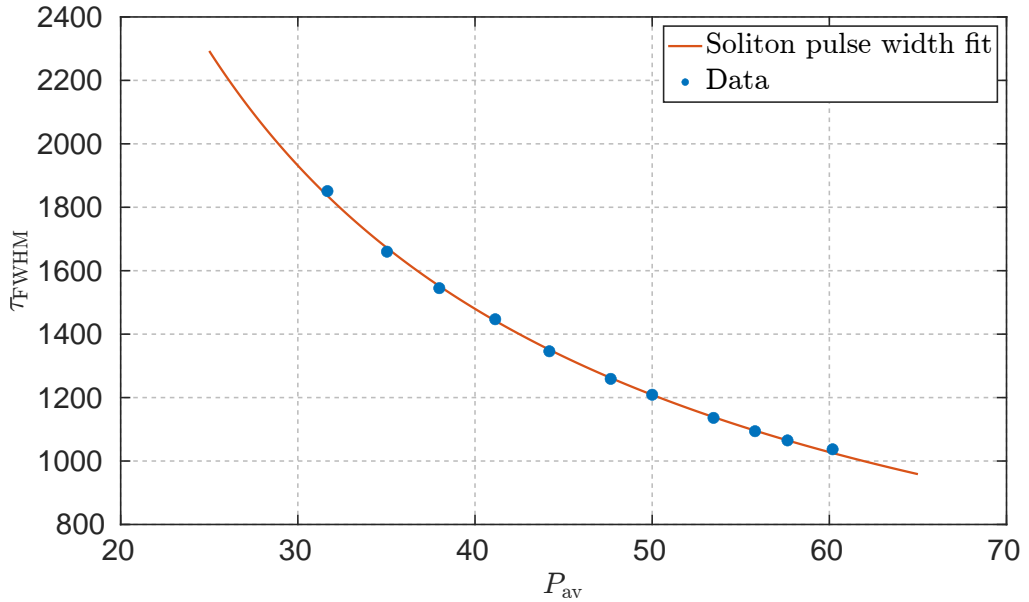


Figure 2.6: Measured pulse width as a function of average laser output power, fitted with an inverse power law ( $1/\bar{P}$ ). The data represents the operating range of the laser between 33 W and 60 W, where stable mode-locking occurs without CW breakthrough or other artefacts.

Using this method, we can incorporate fluctuating peak powers and pulse widths into the simulation. Next, we compare the spectra with and without fluctuations. Figure 2.7 illustrates this comparison, showing that the ratio between these two spectra can be significant at specific wavelengths, resulting in substantial noise amplification, which we will refer to as noise gain moving forward. As the title indicates, "power contributing to SPM" refers to the power that efficiently couples into the fibre. The pulse width is determined from the fit by back-calculating the measured power, considering the presence of an output coupler for the diagnostics beam and an isolator.

It is essential to note that the vertical axes represent gain and power *per slice*

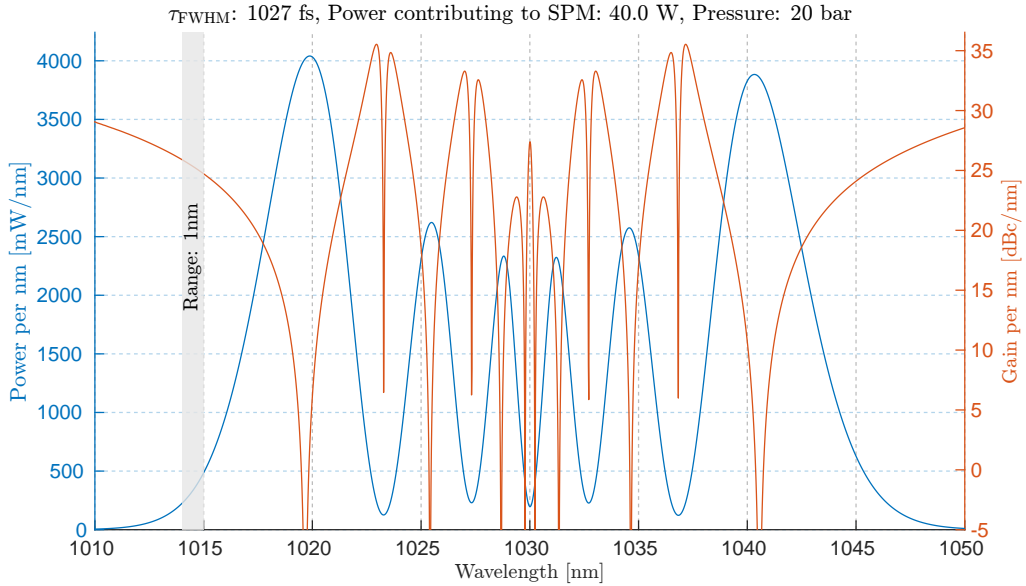


Figure 2.7: Power density per nanometer (left, blue) and noise gain per nanometer (right, orange) as a function of wavelength. The power density reaches 4 W, while the noise gain peaks at 35 dBc and maintains around 29 dBc in the spectral wings. The fibre coupling efficiency is 82%.

*of one nanometer.* This is significant because any measurement setup can only capture a finite spectral range. Increasing the slice interval to 2 nm will double the power within this range but will not necessarily result in a higher noise gain, as illustrated in Figure 2.8. At larger intervals, spectral features become smeared, diminishing the distinct features of spectral broadening. Simulations indicate that a 1 nm spectral slice provides sufficient gain while remaining relatively simple to isolate.

We observe that at specific wavelengths, the relative change in intensity is significant (e.g., on the order of 35 dB). We could potentially infer a lower shot noise level if we can measure the intensity change at these wavelengths. However, many high-gain points, especially on the spectrum's wings, correspond to low-intensity wavelengths, making them challenging to detect with the photodetectors used in this thesis. Even more critically, the reduced power at these outer wavelengths means that the power is counteracting the potential benefits of the high gain. To illustrate this effect, Figure 2.9 shows that most points in the wings disappear once we assume the detector requires a specific amount of power to measure a signal reliably.

Some high-gain points vanish due to low intensity, which numerical calculations and inherent rounding errors may artificially introduce. For the laser parameters ( $\bar{P} = 60$  W,  $t_{\text{FWHM}} = 1027$  fs, and  $p = 20$  bar), up to 29 dB of gain

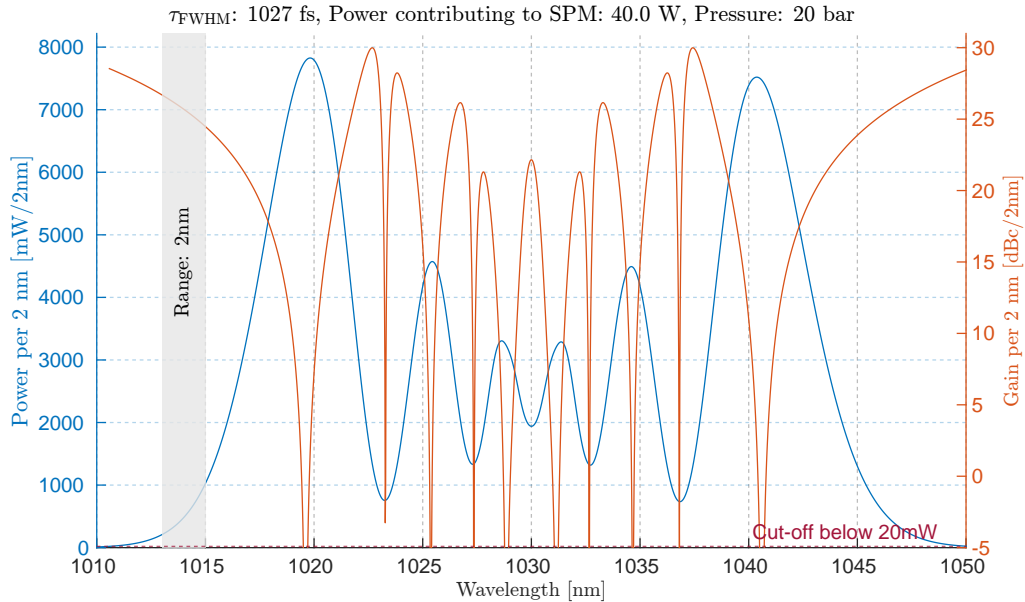


Figure 2.8: Power density per two nanometers (left, blue) and noise gain per two nanometers (right, orange) as a function of wavelength. As expected, the power density reaches 8 W (doubling from the 1 nm slice), while the noise gain slightly decreases, peaking at 30 dBc and 28 dBc in the spectral wings. The fibre coupling efficiency is 82%.

can still be achieved in the spectral wings. Interestingly, even when assuming a minimum required power per spectral slice and keeping all parameters constant except for the pressure, higher pressure does not necessarily result in a larger gain.

To illustrate this effect, Figure 2.10 presents a pressure scan ranging from 1 to 30 bars in increments of 0.1 bar, with all other laser parameters held constant. The maximum achievable gain occurs at the highest pressure point, with a consistent increase from 15 to 30 bars. However, note the gain density around 5.2 bars. While this outlier may initially appear to be a numerical artefact, Figure 2.11 demonstrates that this point is located precisely at the centre of the broadened spectrum. Whenever the central peak "splits" into two new peaks, the maximum gain momentarily decreases before these new peaks become dominant, causing the pressure scan to follow a new trend. The noise gains for pressures of 5.2, 5.5, and 5.6 bars are stacked to show the significant change in maximum gain as the central peak begins to split.

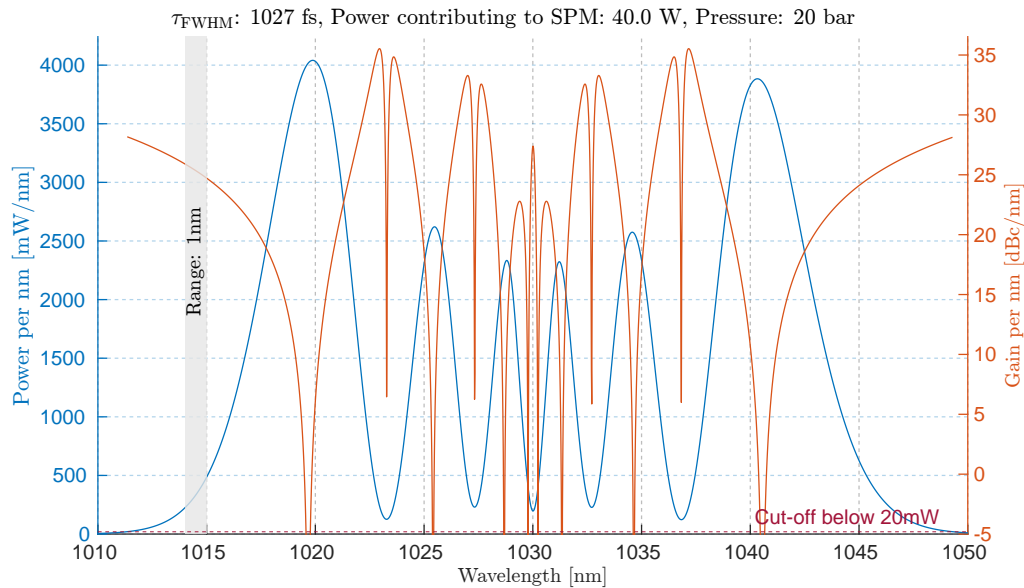


Figure 2.9: Power density per nanometer (left, blue) and noise gain per nanometer (right, orange) as a function of wavelength. The power density reaches 4 W, with the noise gain peaking at 35 dBc. The imposed cut-off at 20 mW causes some points at the spectral wings to be inaccessible. The fibre coupling efficiency is 82%.

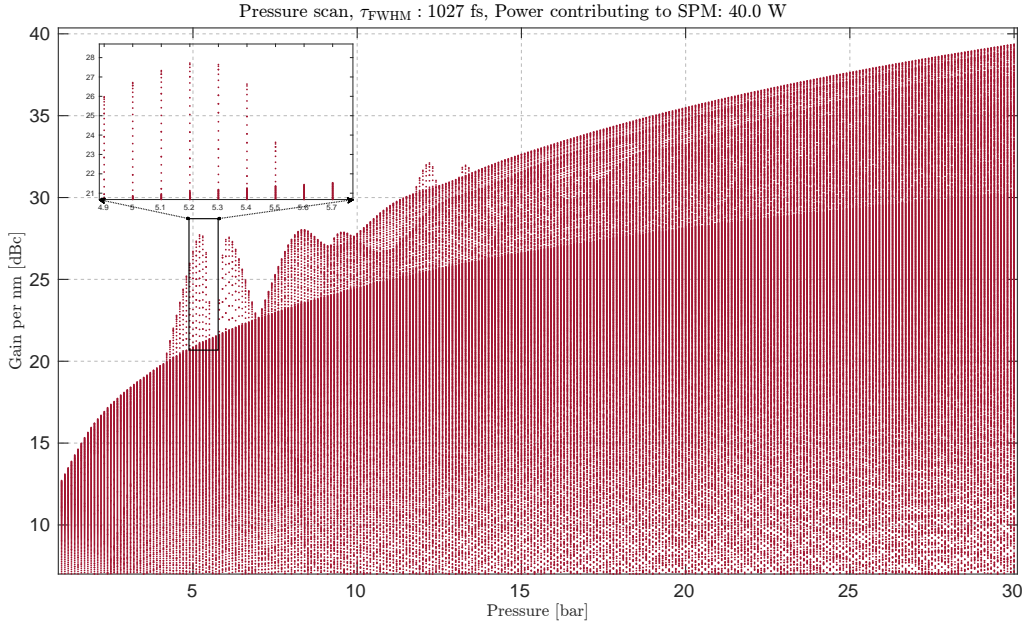


Figure 2.10: Pressure scan from 1 to 30 bars in steps of 0.1 bar. The simulation is run once for each pressure, and the gain density values are plotted along a vertical line. The parameters remain constant: 50 W input power, 82% fibre coupling efficiency, and 1027 fs pulse width with a cut-off at 20 mW.

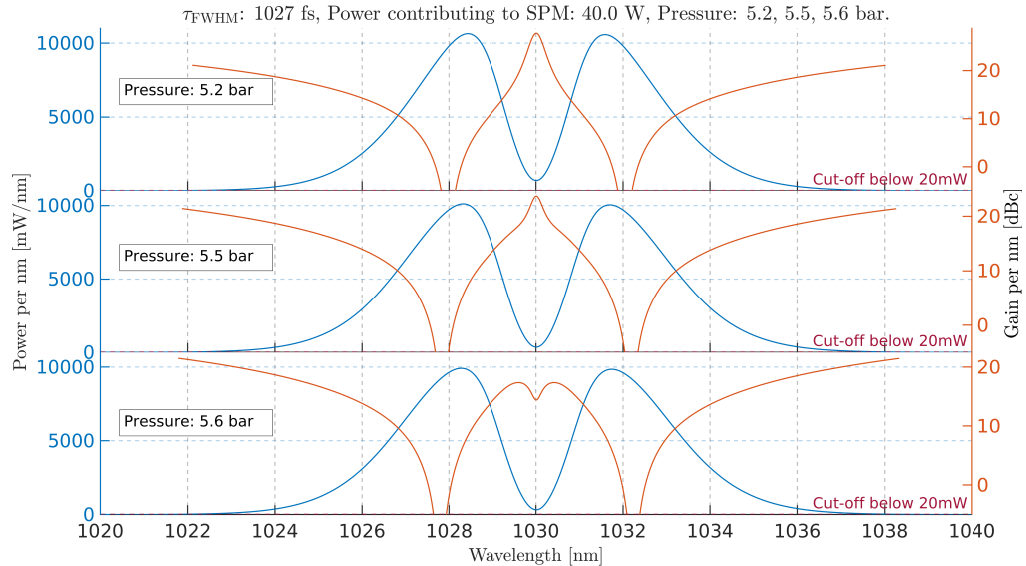


Figure 2.11: Power density per nanometer (left, blue) and noise gain per nanometer (right, orange) as a function of wavelength for three different pressures: 5.2, 5.5, and 5.6 bars. The central peak starts to split around 5.6 bars, leading to a sudden change in maximum gain. The fibre coupling efficiency is 82%.

## CHAPTER 3

# Setup, Characterization and Results

---

This chapter discusses the thesis's experimental setup, including the design of the oscillator, fibre coupling, grating spectrometer, and noise measurement techniques. The steps are discussed in the order of the beam path, starting from the laser cavity and ending in the detection setup.

## 3.1 Oscillator

The cavity design employs a two-pass geometry to achieve a repetition frequency of 19.7 MHz, a pulse duration of 1030 fs, and an average output power of 60 W. This two-pass configuration balances maximizing the gain per roundtrip and maintaining a manageable system complexity, as each additional pass requires two more mirrors, which can quickly crowd the oscillator setup.

The choice of repetition rate is crucial and not arbitrary. A higher repetition rate allows for noise measurements to extend to higher frequencies. Still, it also results in lower pulse energies and peak powers, which is not ideal for achieving significant spectral broadening. Conversely, a lower repetition rate enhances spectral broadening due to the increased pulse energies and peak powers; however, it limits noise measurements by restricting the maximum frequency components that can be effectively measured. Thus, a repetition rate of about 20 MHz offers a reasonable compromise between these competing factors.

The repetition frequency is determined by the distance from the output coupler to the end mirror,  $l = \frac{c}{2f_{\text{rep}}} = 7.6$  meters, where the factor of two accounts for the light being outcoupled only once per full roundtrip. The average output power is indirectly controlled, as the gain medium is assumed to be fixed. The output power relates to the intracavity power by  $P_{\text{intra}} = \frac{P_{\text{avg}}}{r}$ , where  $r$  is the output coupling rate, influencing the fluence on the end mirror or saturable absorber, in this case, a SESAM. A bare two-pass cavity, symmetric in the beam waist as a function of position, serves as the starting point. Figure 3.1 shows this

configuration with two passes on the disk, an output coupler, and an end mirror.

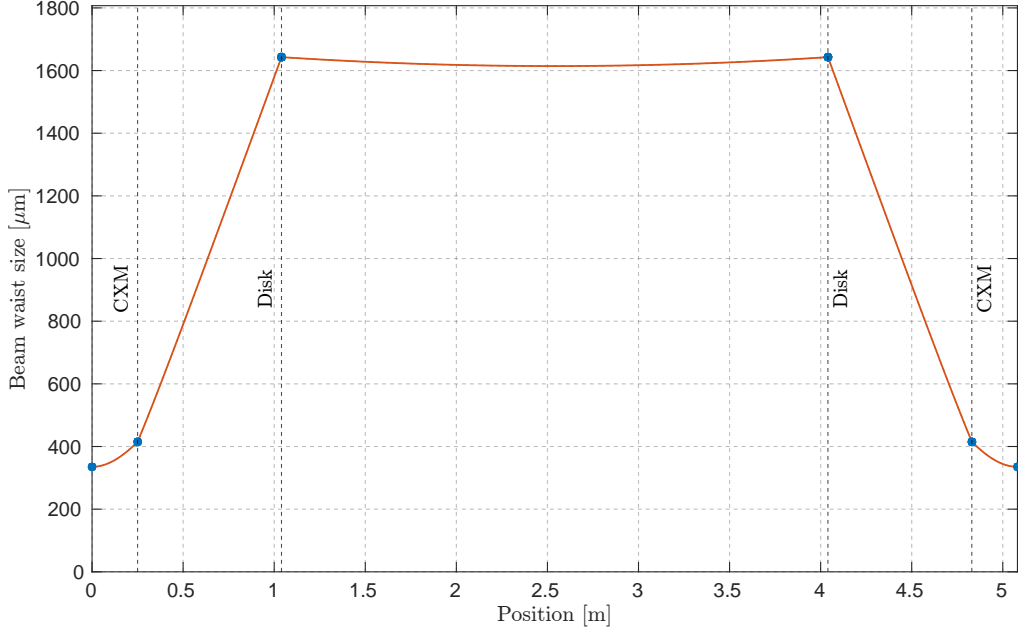


Figure 3.1: Evolution of the beam waist size (orange) within the simplest two-pass cavity in a symmetric configuration. The black dashed vertical lines and blue dots denote curved mirrors or the disk, with a nominal radius of curvature of -2 m. The beam size exhibits a symmetric pattern, repeating approximately every 2.5 meters. This configuration serves as the starting point for optimizing the final cavity design.

From this starting point, parameters such as distances between mirrors are adjusted, and additional mirrors are added to fit our needs. For stability, the beam must always focus at the ends of the cavity to maintain the periodicity of the beam waist.

To achieve soliton modelocking, sufficient self-phase modulation is needed to counteract the group delay dispersion. The B-integral [33] quantifies the SPM:

$$B = \frac{2\pi}{\lambda} \int n_2 I(z) dz, \quad (3.1)$$

There is no additional SPM medium in the cavity, which is unique compared to most low-power, non-thin disk lasers that achieve significant self-phase modulation (SPM) within the gain medium, as SPM through air propagation is negligible. In contrast, high-power TDLs usually require a vacuum to reduce undesirable SPM effects [34]. For stable mode-locking, a B-integral around 50 mrad is typically required, based on empirical results [25].

Figure 3.2 shows the final configuration of the TDL cavity, featuring a telescope to control the beam size on the SESAM and, consequently, the fluence on the SESAM. Group Delay Dispersion is introduced using Gires-Tournois interferometer style (GTI) mirrors. These mirrors, while often named after the classical GTI with an air gap, are chirped mirrors. They achieve the desired wavelength-dependent phase shift through a carefully designed, wavelength-dependent optical path difference [35].

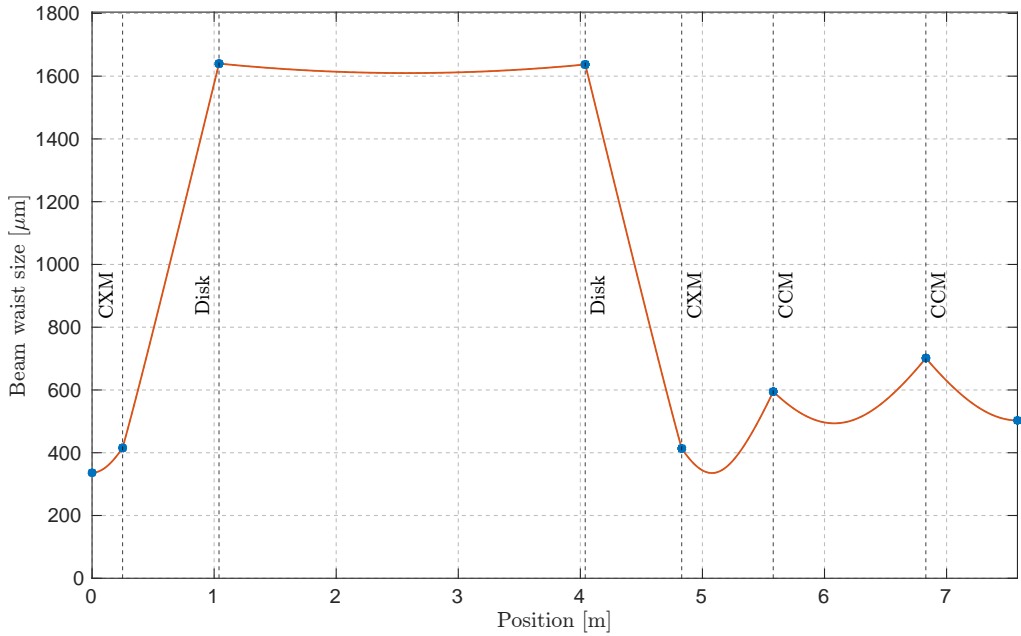


Figure 3.2: Beam waist evolution in the final cavity configuration, illustrating the change in beam waist size as the light travels through the cavity, starting from the output coupler and ending at the SESAM. Curved mirrors, the TDL disk, and SESAM and OC are depicted with a blue dots. Plane mirrors and plane GTI's are not shown.

Long-term stability in high-power oscillators also necessitates careful management of thermal effects, as increased power enhances both thermal lensing and disk bending. These effects result in a temperature-dependent radius of curvature, influenced by heating and gas convection in front of the disk [36]. Thermal lensing and gas convection effects are equally significant in an air-filled cavity. The cavity must operate in a regime where small variations in the disk's curvature do not lead to destabilization. As shown in Figure 3.3, no nearby singularities indicate a stable configuration.

Figure 3.4 schematically depicts the final cavity configuration.

To control the polarization of the laser output, a thin-film polarizer is introduced into the cavity. This ensures that only light with a well-defined polarization

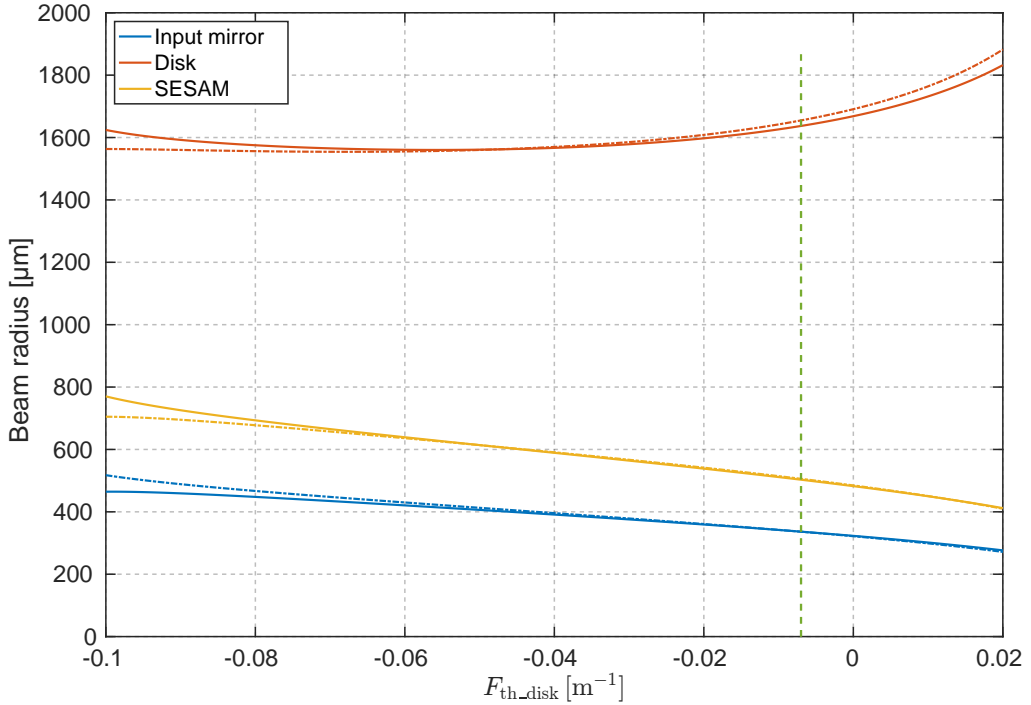


Figure 3.3: Beam radius on the SESAM as a function of its thermal lensing. The horizontal axis covers a very broad range, fully encompassing the laser’s operating range. The absence of singularities or rapid changes suggests a stable configuration with respect to thermal lensing. The operation point of the cavity is depicted as a dashed line.

can oscillate, improving the overall beam quality and stability of the cavity.

The efficiency of the laser system is crucial for evaluating its performance. The output power  $P_{\text{output}}$  is related to the pump power  $P_{\text{pump}}$  by the following equation:

$$P_{\text{output}} = \eta (P_{\text{pump}} - P_{\text{threshold}}), \quad (3.2)$$

where  $P_{\text{threshold}}$  is the laser’s threshold power, and  $\eta$  represents the slope efficiency. This key figure of merit approaches 38% at high pump powers. Figure 3.5 illustrates the output power and slope efficiency as a function of the pump power.

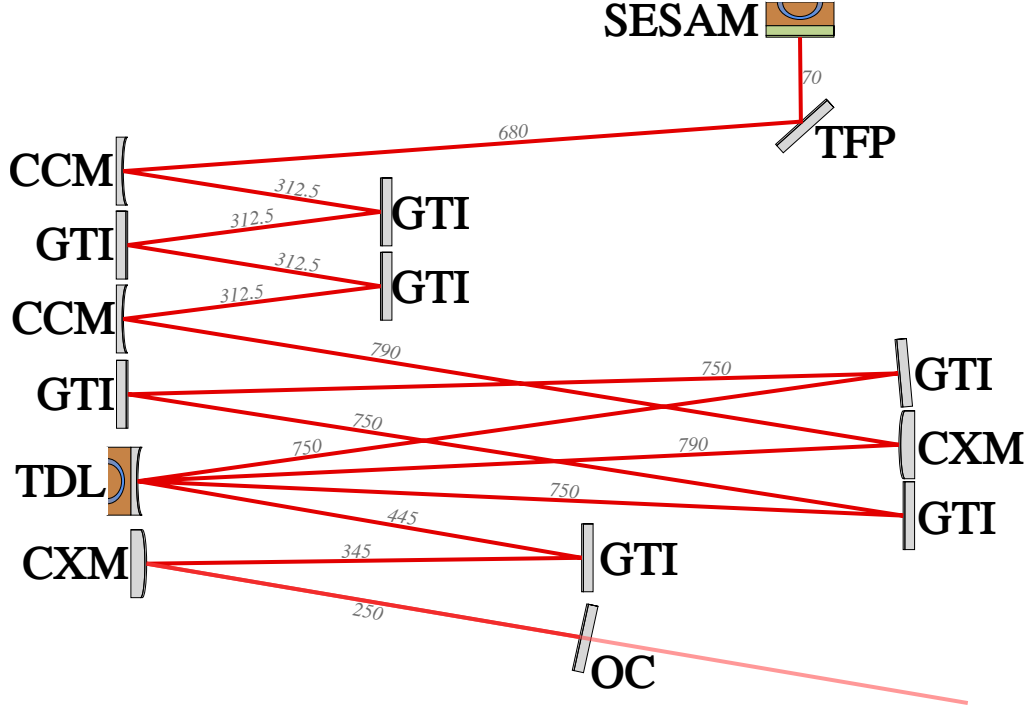


Figure 3.4: Schematic of the laser cavity and its components. GTI denotes the Gires-Tournois interferometer, TFP represents the thin-film polarizer, OC is the output coupler, CCM is the concave mirror, CXM is the convex mirror, and TDL stands for the thin-disk laser. The blue elements behind the SESAM and TDL indicate active water cooling. The path of the oscillating light is shown schematically, with distances in millimetres marked in grey.

Table 3.1: Parameters of the final laser cavity.

Parameter	Value
Average output power (no CW breakthrough)	60 W
Pulse duration	1030 fs
Repetition rate	19.7 MHz
Required GDD to counteract SPM	-15,550 fs <sup>2</sup>
Central wavelength	1030 nm

## 3.2 Beam Diagnostics

### $M^2$ Measurement

After the laser light exits the cavity, it is crucial to characterize the output beam quality. A small fraction of the laser power is extracted and directed towards the diagnostics setup. The key metric for beam quality is the  $M^2$  value, which

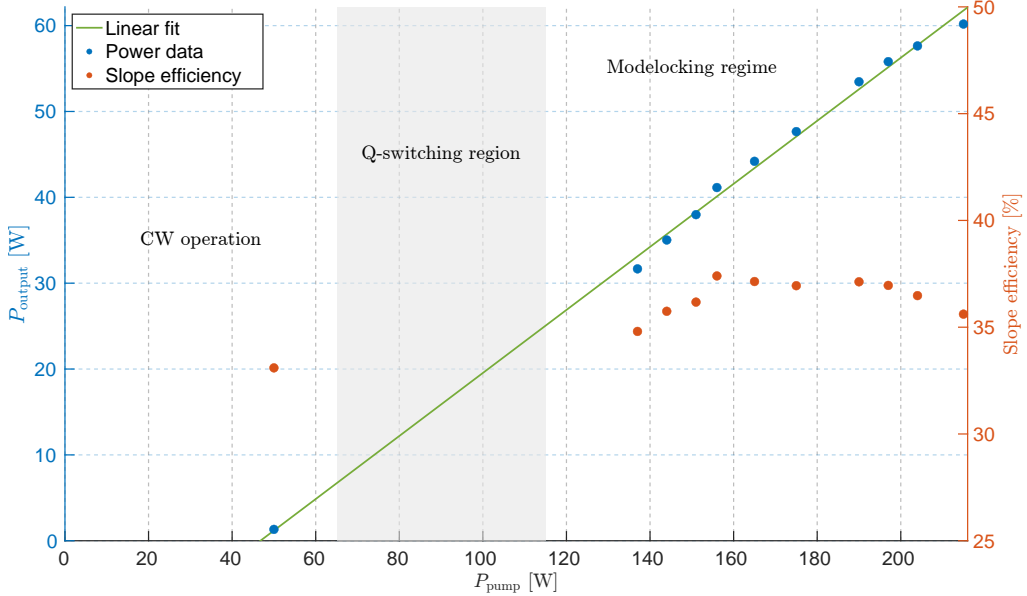


Figure 3.5: Output power (left) and slope efficiency (right) of the thin-disk laser as a function of pump power. The first data point is before modelocking has been achieved, while the grey-shaded area is the Q-switching regime (65 to 115 W). Therefore, no data has been recorded here.

quantifies how closely the laser beam approximates an ideal Gaussian beam [37]. An ideal Gaussian beam has an  $M^2$  value of 1, indicating minimal divergence and optimal focusability. A higher  $M^2$  value indicates greater beam divergence and reduced focusability. The relationship between the beam divergence angle  $\theta$ , the beam waist  $w_0$ , and the  $M^2$  value is given by:

$$\theta = M^2 \frac{\lambda}{\pi w_0}. \quad (3.3)$$

Figure 3.6 presents the results of the  $M^2$  measurement, yielding a value of  $M^2 < 1.1$ . This measurement was conducted by passing the laser beam through a focusing lens, after which a moving stage equipped with a slit profiler measured the beam width along the  $X$  and  $Y$  axes at various positions along the beam path. The collected data points were then fitted to calculate the  $M^2$  value.

### Spectrum Analyzer

A small portion of the output power, approximately 50  $\mu$ W, is directed to an optical spectrum analyzer (OSA) to measure the laser output spectrum. The OSA reveals that when the laser is mode-locked, the central wavelength is at 1029.75 nm with a full-width at half-maximum (FWHM) of 1 nm, consistent

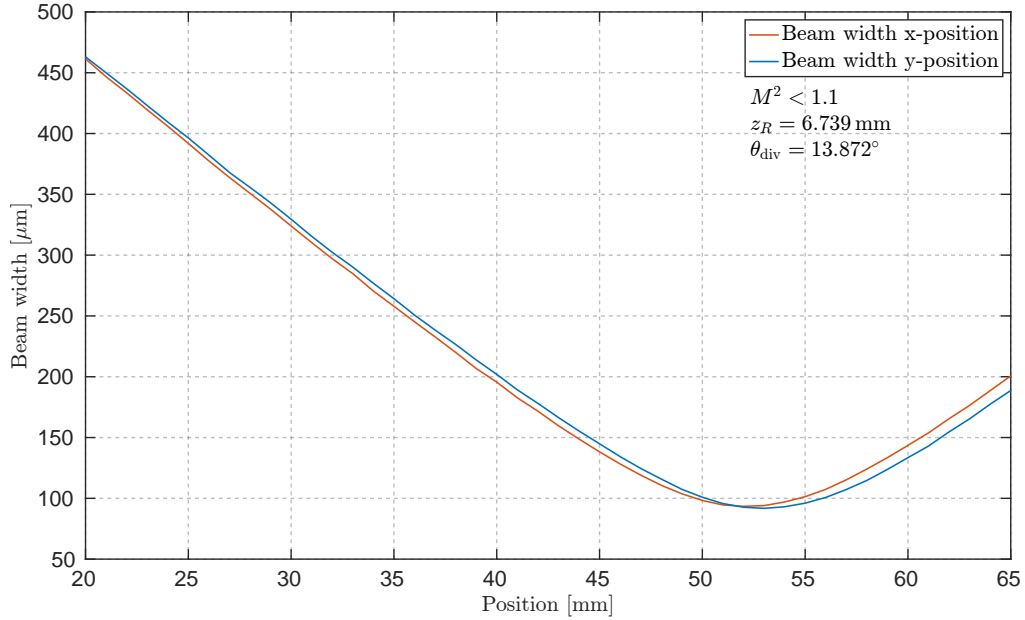


Figure 3.6: Results of the  $M^2$  measurement using a beam slit profiler. The stage moved a total of 45 mm to determine that  $M^2 < 1.1$ , with a Rayleigh length of  $z_R = 6.739$  mm at the focus. The divergence angle was calculated to be  $\theta_{\text{div}} = 13.872^\circ$ .

with the emission wavelength of Ytterbium. The laser operates in continuous wave mode at lower pump powers, displaying a narrow line-like spectrum.

Another small fraction of the laser power is directed to a microwave spectrum analyzer (MSA) to obtain the frequency spectrum, which includes multiple harmonics of the mode-locked signal. A photodiode converts the optical signal into an electrical one for analysis by the MSA. As expected, as shown in Figure 3.8, multiple peaks corresponding to harmonics of the repetition rate,  $f_{\text{rep}} = 19.7$  MHz, are observed. Figure 3.7 displays a single peak captured by the MSA, corresponding to the laser's repetition frequency of 19.7 MHz. The measurement was performed with a resolution bandwidth of 300 Hz.

See the appendix 4 for other diagnostics measurements done at different pump powers.

## Autocorrelation

We use an intensity autocorrelator to determine the pulse width and the temporal structure of the laser output. The methodology and principles behind this technique are discussed in detail in Appendix 4. The measured pulse width is approximately 1037 fs, close to the transform-limited pulse duration of 1000 fs, as

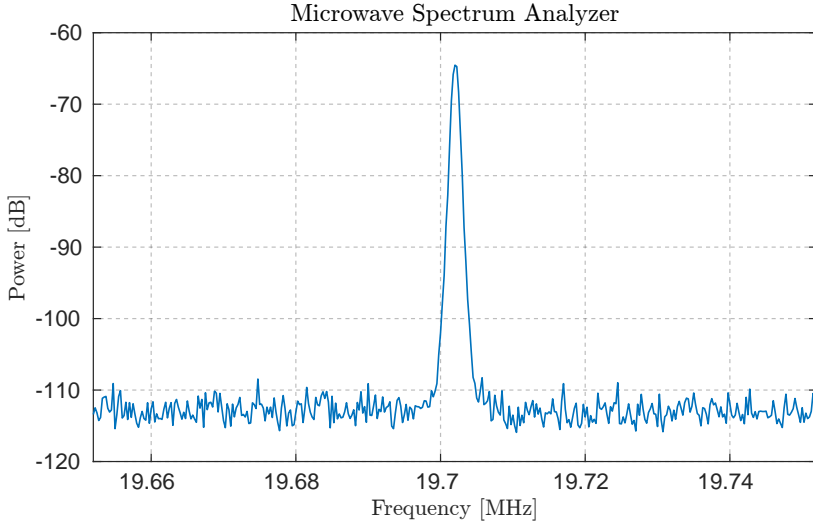


Figure 3.7: Zoomed view of the MSA output showing a single repetition frequency peak at 19.7 MHz, recorded with a resolution bandwidth of 300 Hz.

determined from the OSA measurement. Figure 3.8 shows the diagnostic results from the spectrum analyzers and the autocorrelator. The dashed fit represents an ideal soliton pulse.

### 3.3 Fibre Coupling

In this section, the path from the laser cavity to the hollow-core fibre is traced and explained in detail.

#### Mode-Field Diameter

The specified mode-field diameter (MFD) of the fibre is 42  $\mu\text{m}$ . To efficiently couple into the fibre, the beam needs to be collimated to a much smaller size compared to its size at the output coupler (OC). Simulations estimate the beam waist size at the output coupler to be 335  $\mu\text{m}$  in both the horizontal and vertical axes (beam waist sizes are given with respect to their  $1/e^2$  radius unless otherwise specified). Thus, a magnification factor of  $M = 16$  is needed. A straightforward method to reduce the waist size is to build a telescope consisting of two lenses with focal lengths  $f_1$  and  $f_2$ . The first lens is placed at a distance  $f_1$  from the OC, and the second lens is positioned  $f_1 + f_2$  from the first lens. Both lenses should satisfy  $M = \frac{f_1}{f_2} = 16$  to reduce the waist size to a radius of 21  $\mu\text{m}$ . A reasonable combination of lenses is  $f_1 = 2000$  mm and  $f_2 = 125$  mm, which should achieve this size. To verify that the desired waist size is reached, the single-plane beam

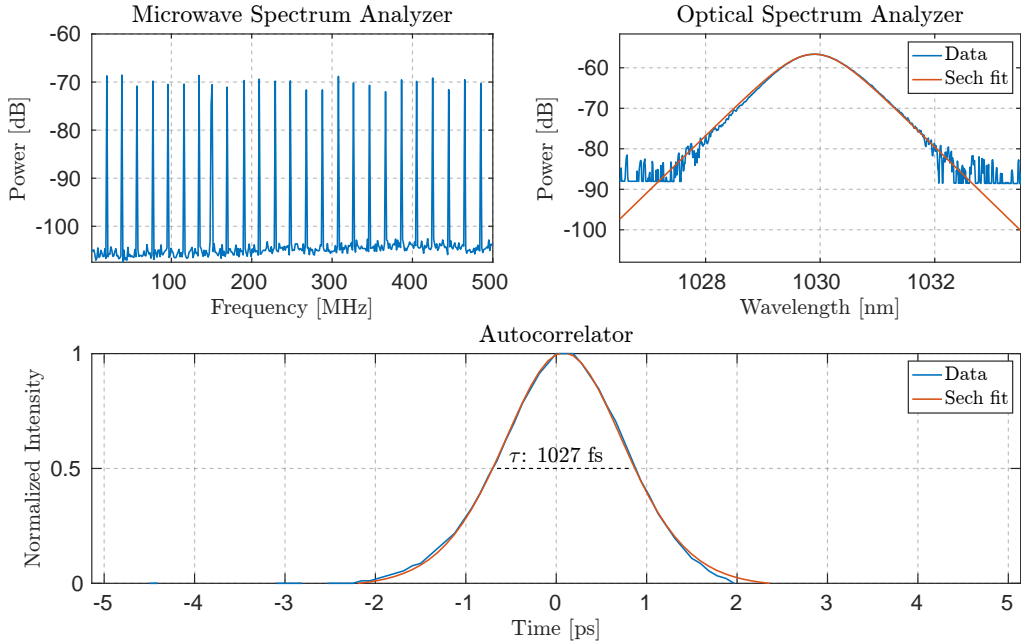


Figure 3.8: Combined diagnostic results from the microwave spectrum analyzer (MSA) measured with 1 kHz resolution bandwidth, autocorrelator, and optical spectrum analyzer (OSA). The MSA reveals multiple harmonics corresponding to the laser's repetition rate, confirming stable mode-locking. The autocorrelator provides the pulse width measurement, while the OSA shows the laser's output spectrum, highlighting a central wavelength of 1029.75 nm with a 1 nm FWHM, consistent with the emission wavelength of Ytterbium. The red line represents an ideal soliton pulse fit.

profiler Beam'R2 from DataRay is used, capable of profiling beams as small as 2  $\mu\text{m}$ . However, results showed that the beam was larger than expected at the focus and slightly elliptical, with a 4:3 ratio between the horizontal and vertical axes. This is likely due to the non-zero angle of incidence in the horizontal direction inside the oscillator, which caused the beam to become asymmetrical. This effect persisted even after replacing the SESAM, indicating that the SESAM was not the primary cause. To correct this issue, an additional telescope that works in only one axis, using cylindrical lenses, is required.

Two lenses should have focal lengths with an absolute ratio of 4:3. However, to avoid creating a focus between these two lenses (which could introduce additional artefacts due to high intensity), a combination of convex and concave lenses is used. This is realized using  $f_{1,\text{cyl.}} = 100 \text{ mm}$  and  $f_{2,\text{cyl.}} = -75 \text{ mm}$ , spaced at 100 mm and 125 mm behind the OC, respectively. Figure 3.9 shows the beam waist size of the horizontal and vertical axes, where position 0 is the OC of the laser cavity. The beam is assumed to be elliptical at the OC with a 4:3 ratio

between both axes.

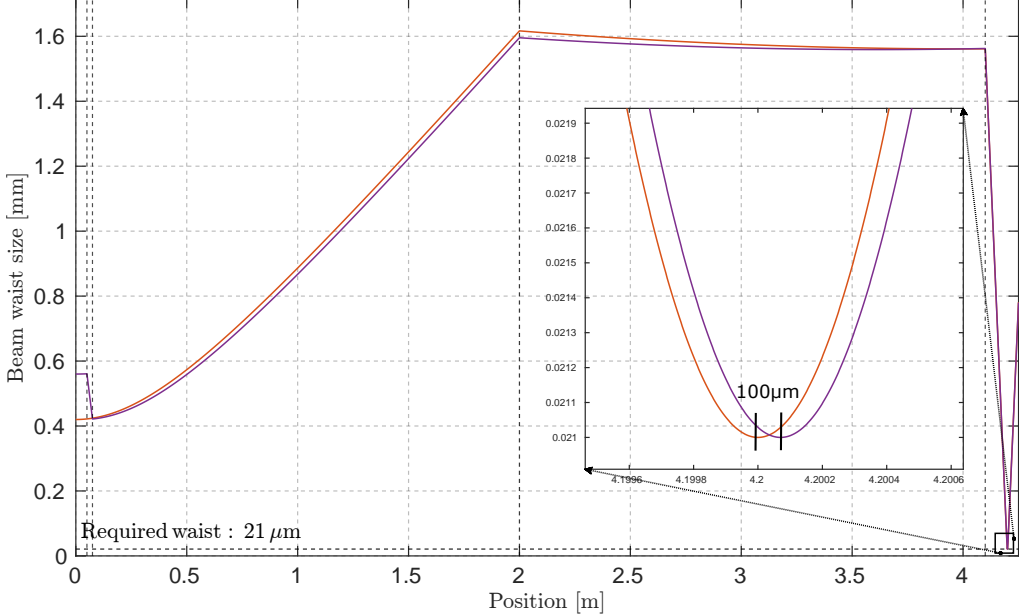


Figure 3.9: Beam waist evolution as the laser passes from the output coupler of the cavity through the telescope, which optimizes the beam for fibre coupling. The orange and violet curves represent the beam waist sizes in the horizontal and vertical axes, respectively. The zoomed-in section highlights slight astigmatism between the horizontal and vertical foci at the fibre's focal point.

The simulation suggests that this setup introduces slight astigmatism, with a spacing of roughly 100  $\mu\text{m}$  between the foci of the two axes. While strong astigmatism could significantly reduce coupling efficiency and increase the risk of damaging the fibre, this small amount of astigmatism does not appear to cause significant issues. This is evidenced by the fact that the experiments still achieved a good coupling efficiency of up to 85%. If astigmatism had been a significant issue, the coupling efficiency would be much lower.

### Power Tuning

Another important consideration is power tuning. Even if everything works as expected, it is dangerous to immediately send full power into the fibre, especially if beam stabilization has not yet been achieved. A common issue with SESAMs is Q-switching: initially, the output power can be finely tuned from 0 W to about 4 W before Q-switching occurs. Typically, the pump power is ramped up quickly to minimize time spent in the Q-switching regime, reducing the risk of damaging components or the thin-disk itself. However, this means the power cannot be slowly and continuously tuned for values above 4 W. A simple yet elegant solution

to this problem is to use a combination of a half-wave plate (HWP) and a thin-film polarizer (TFP). By rotating the polarization, the fraction of the beam that is reflected or transmitted by the TFP can be controlled. A second pair of HWP and TFP allows for even finer control. This way, the HWP can be adjusted to minimize power reaching the fibre at low laser output power. The laser can then be safely mode-locked, and the HWP can be rotated to increase the power directed into the fibre.

## Polarization

While the fibre has no defined birefringence, induced birefringence effects along preferential polarization angles might occur due to the non-radially symmetric structure of the photonic crystal in the fibre and fibre bending. Indeed, the input polarization can change the beam shape and far-field profile. Incorrect polarization also dramatically increases the fibre's sensitivity to touch. Therefore, a half-wave plate is placed before the fibre to control the input polarization.

## Fibre Coupling

As mentioned earlier, the specified MFD of the fibre is 42  $\mu\text{m}$ . This is a relatively large MFD compared to other optical fibres, meaning the beam position is less critical for efficient coupling into the fibre. However, the angular alignment becomes much more sensitive. Two coupling mirrors allow fine-tuning of the angular alignment, while a standard three-axis linear translation stage allows the fibre entry position adjustment. This setup keeps the coupling process relatively straightforward, unlike using a five-axis stage for the fibre, especially when the two coupling mirrors are already present.

## Pressure and Gas System

The simulations assume a pressure of 25 bars with Xenon in the fibre. However, at this pressure, Xenon costs approximately 4,000 CHF per litre, making it impractical for initial tests. A more cost-effective gas, Argon, was used at a pressure of 10 bars to ensure the gas control system functions properly. During testing, the system initially exhibited a minor leak, resulting in a pressure drop of 2 bars over 8 hours. Attempts to repair the leak led to further complications, making the system unable to hold pressures over 5 bars, requiring the entire system to be returned for a complete reconnection of the fibre.

### 3.4 Grating Spectrometer

As discussed in Chapter 2.6, applying high pressure to a gas with a high nonlinear refractive index and allowing the pulse to propagate will generally lead to significant spectral broadening. For example, a pulse that initially had a full-width at half-maximum (FWHM) of 1 nm may broaden to an FWHM of approximately 50 nm. Since the focus is on the spectral regions where the gain is high and the power is sufficient for measurement, it is essential to filter a specific part of the spectrum selectively. This can be accomplished using a grating spectrometer, which allows for precisely selecting the wavelength range of interest. The principle behind this setup is straightforward: the fibre output is directed onto a blazed grating, which disperses the light by making it disperse, causing different wavelengths to have distinct wavevectors. By using a narrow slit, we can effectively select the desired spectral region. Figure (3.10) shows the schematic working principle of this spectrometer. This section closely follows the principles outlined in [38].

A grating functions by altering the incident phase and amplitude of incoming light to separate different wavelengths. The interference pattern created depends on the grating's geometry. In this thesis, a blazed grating is used, characterized by its blaze wavelength, groove spacing  $d$ , and blaze angle  $\gamma$ . The angles are measured relative to the surface normal, and the groove spacing can be expressed in terms of groove density  $d = 1/N$ , where  $N$  is typically given in lines per millimetre. The blaze angle  $\gamma$  is the angle between the facet normal and the surface normal, and adjusting this angle allows for tuning the grating's efficiency.

The grating equation relates the angle of incidence  $\alpha_i$  with the diffraction angle  $\beta_m$ , depending on the diffraction order  $m$  and the wavelength  $\lambda$ :

$$d(\sin \alpha_i + \sin \beta_m) = m\lambda \quad (3.4)$$

No diffraction pattern is observed in the zeroth order mode ( $m = 0$ ), making this case uninteresting. In this mode, the only solution is  $\alpha_i = -\beta_m$ , meaning the angle of incidence equals the angle of diffraction, analogous to specular reflection on a flat surface. This result is independent of wavelength and thus provides no spectral information.

At twice the blaze angle, we find:

$$d \sin(-2\gamma) = m\lambda. \quad (3.5)$$

A special case is the so-called *Littrow configuration*, where the grating efficiency is maximized. This occurs when  $\alpha_i = \beta_m$  and  $m > 0$ . Referring to equation (3.4), we find:

$$2d \sin \theta_L = m\lambda_D, \quad (3.6)$$

where  $\theta_L$  is the Littrow angle, and  $\lambda_D$  is the design wavelength, defined as the wavelength at which the grating is most efficient. The Littrow angle depends on the most intense order ( $m = 1$ ), and at  $\lambda = \lambda_D$ , we have  $\theta_L = \gamma =$

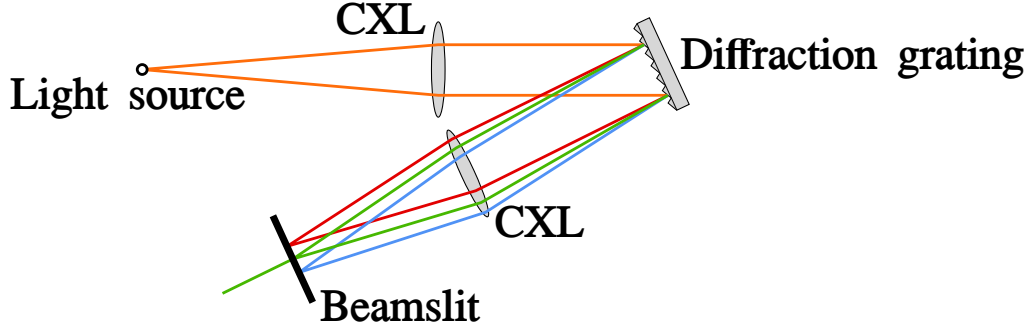


Figure 3.10: Schematic diagram of a grating spectrometer. The convex lens (CXL) focuses the incoming light and resolves the spectral overlap, allowing each wavelength to be detected at distinct positions on the detector.

$\arcsin\left(N \frac{m\lambda_D}{2}\right)$ . Since  $\arcsin$  returns real values only for inputs between  $-1$  and  $1$ , this also defines a maximum groove density  $N_{\max} \leq \frac{2}{m\lambda_D}$ .

The angular dispersion  $D$  is given by:

$$D = \frac{d\beta}{d\lambda} = \frac{Nm}{\cos\beta}. \quad (3.7)$$

Next, we analyze the free spectral range. Reflected light of different orders may overlap, but this can be avoided for the wavelength range  $[\lambda_1, \lambda_2]$  if:

$$\lambda_2 - \lambda_1 = \frac{\lambda_1}{m} \quad (3.8)$$

holds for  $\lambda_1 < \lambda_2$ . Fortunately, this is not an issue with  $m = 1$ , as can be easily verified by considering the central wavelength of 1030 nm.

Another crucial factor is the *spectral resolution*, which limits the minimum wavelength differences that can be resolved by using a diffraction grating. There are two approaches to determine whether two wavelengths can be resolved:

**1) Resolving Power** The resolving power is defined as  $R = \frac{\lambda}{\Delta\lambda} = mN_{ill}$ , where  $\Delta\lambda$  is the smallest resolvable difference from  $\lambda$ , and  $N_{ill}$  is the number of illuminated grooves. This allows us to estimate:

$$\Delta\lambda = \frac{\lambda}{mN_{ill}} = \frac{\lambda \cos(\theta_i)}{m2Nw}, \quad (3.9)$$

where  $w$  is the beam waist on the grating,  $\theta_i$  is the angle of incidence, and the factor of 2 accounts for the beam waist being a radius. With the beam size of this TDL, this results in a spectral resolution below 0.5 nm for a grating with 600 l/mm and a Littrow angle of 18 degrees. Figure (3.11) shows the beam

waist after the fibre, demonstrating that the chosen setup with lenses results in a collimated beam on the grating, justifying the approximation of ignoring the Gaussian nature of the beam.

**2) Gaussian Optics** First, assume the grating behaves like an ordinary mirror, not affecting the beam waist. Then, ray transfer matrix analysis simulation shows that the focus behind the second lens will have a waist  $w_{\text{exit}} = 50.4 \mu\text{m}$ . Now, consider the problem: If this behaviour holds for every spectral component, what must be the wavelength difference  $\Delta\lambda$  for their positions in the focus after the lens to differ by  $w_{\text{exit}}$ ? The spectrum will not be smeared if their separation is larger than their individual waist sizes. This problem simplifies near the Littrow configuration, as the projection of two spots from two spectral components onto a common surface is equal, even for different spectral components. The spatial distance between two wavelengths is:

$$\Delta x = f_2(\sin(\theta_2) - \sin(\theta_1)) = f_2 m N \Delta\lambda, \quad (3.10)$$

where  $\theta_i = \arcsin(m\lambda N - \sin(\theta_i))$  and  $f_2$  is the focal length of the lens after the grating. Setting  $\Delta x = 2w_{\text{exit}}$ , we obtain:

$$\Delta\lambda = 2 \frac{w_{\text{exit}}}{f_2 m N}, \quad (3.11)$$

which is approximately 0.3 nm. Since this value is lower than the resolution obtained using the resolving power, smearing due to the Gaussian nature of the beam is unlikely to be problematic, as the resolving power would not have permitted higher resolution in the first place.

In summary, this setup allows resolving spectral features as small as 0.5 nm.

### 3.5 Characterization

To fully characterize the laser, several key factors must be considered. Firstly, the photodiode (PD) must operate within its linear range, where its voltage response remains proportional to the incident power and does not become saturated. A low-pass filter might be necessary to suppress peaks at the repetition frequency, preventing potential damage to the oscilloscope or signal spectrum analyzer.

Suppose amplifiers are employed to enhance the signal. In that case, verifying that they provide consistent gain across the relevant frequency range is essential, meaning they should have a flat frequency response. Additionally, the repetition rate must not exceed the amplifiers' saturation limits. Since consistent gain is typically achievable only within specific frequency bands, multiple amplifiers might be required for different measurements, and their results may need to be combined at a common reference point.

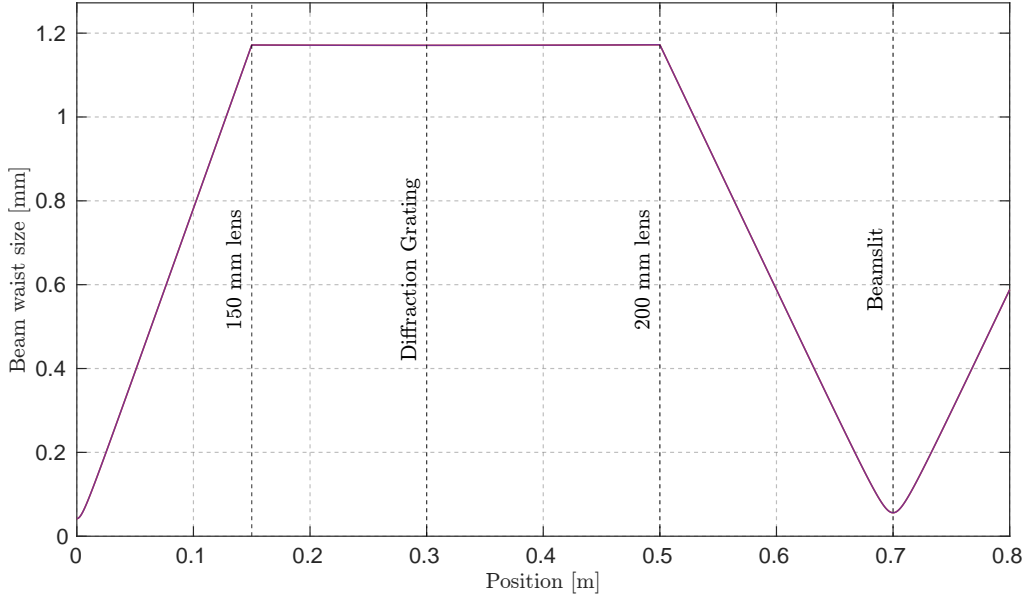


Figure 3.11: Evolution of the beam waist after exiting the fibre and passing through a 150 mm focusing lens, which collimates the beam to a large radius at the grating. The beam slit is positioned at the focal point after reflection from the grating to select a specific wavelength range.

### 3.5.1 Photodiode Characterization

Two photodiodes were evaluated for measuring the laser noise: Thorlabs' large-area ( $75.4\text{ mm}^2$ ) silicon photodetector DET100A/M and the FDS100 silicon photodiode. The DET100A/M operates over wavelengths from 350 to 1100 nm, with a rise time of 43 ns, while the FDS100, with a smaller active area of  $3.6\text{ mm} \times 3.6\text{ mm}$ , offers a faster rise time of 10 ns. Increasing the applied reverse bias enhances the photodiode's responsivity due to improved charge collection efficiency [39]. Silicon photodiodes are favoured for their low cost, low dark current, and high-speed performance. The DET100A/M is operated at a fixed reverse bias of 10 V, while the FDS100 may operate with a reverse bias of up to 25 V. The following measurements were done at 24 V reverse bias.

To assess the performance of the photodiodes, the average generated voltage response was measured against the incident power. The generated voltage was  $50\Omega$  terminated and measured using either a multimeter or an oscilloscope. The multimeter provides the average voltage, while the oscilloscope allows for peak voltage measurements. However, peak voltage measurements can be misleading due to noise and short-term disturbances, often resulting in artificially high readings. Figures 3.12 and 3.13 present the measured average voltages, with a reverse bias of 24 V applied to the FDS100 photodiode.

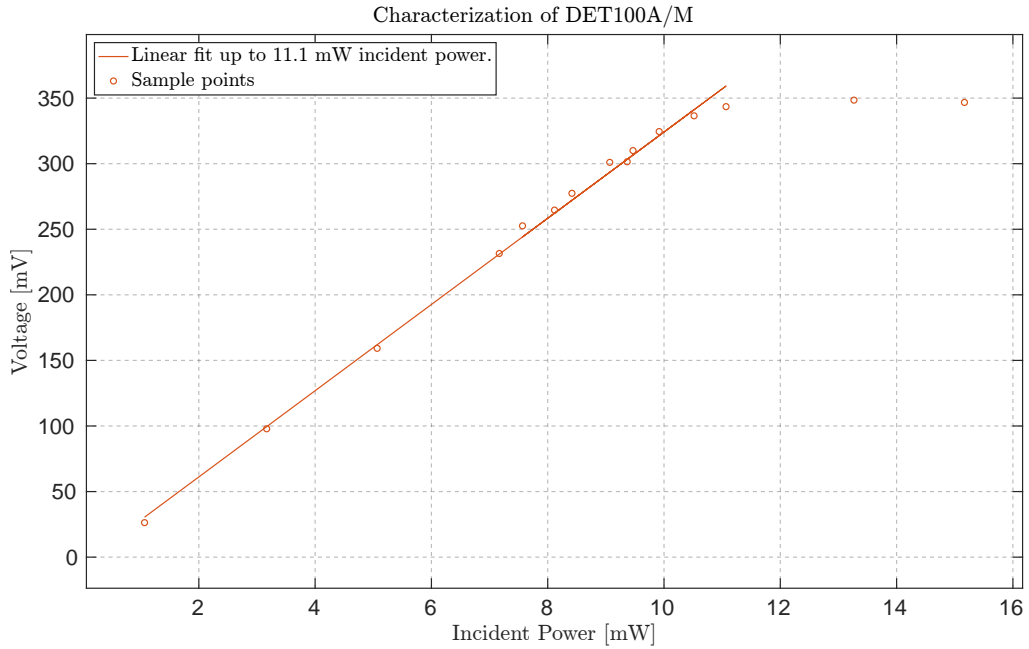


Figure 3.12: Characterization of the silicon photodiode DET100A/M, showing a linear response for chosen points up to 11.1 mW of incident power. Points where the photodiode is already saturated are excluded from the linear fit.

These results suggest that the small-area FDS100 photodiode should enable the measurement of lower shot noise levels. The shot noise limit, expressed in units of dBc/Hz, is given by:

$$S_{\text{shot}} = 10 \log_{10} \left( 2q \frac{R}{V_{\text{DC}}} \cdot 1 \text{ Hz} \right), \quad (3.12)$$

where  $q$  is the electron charge,  $R = 50 \Omega$  is the termination resistance, and  $V_{\text{DC}}$  is the generated average (DC) voltage. For a detailed derivation, refer to the discussion leading up to Eq. 3.19. Comparing the generated DC voltages at the maximum point of the linear range (1100 mV for DET100A/M and 320 mV for FDS100):

$$\Delta S_{\text{shot}} = 10 \log_{10} \left( \frac{1100}{320} \right) = 5.36 \text{ dBc}. \quad (3.13)$$

Therefore, in theory, the FDS100 photodiode should allow for the measurement of lower shot noise levels. However, the traces obtained were not as anticipated, so the noise measurements were ultimately performed with the DET100A/M photodiode. The characteristics of the chosen photodiode significantly influence the optimal measurement settings. With these measurements in hand, noise measurements can now be performed while ensuring that the photodiode operates within its linear range, avoiding saturation. Saturation of the photodiode would

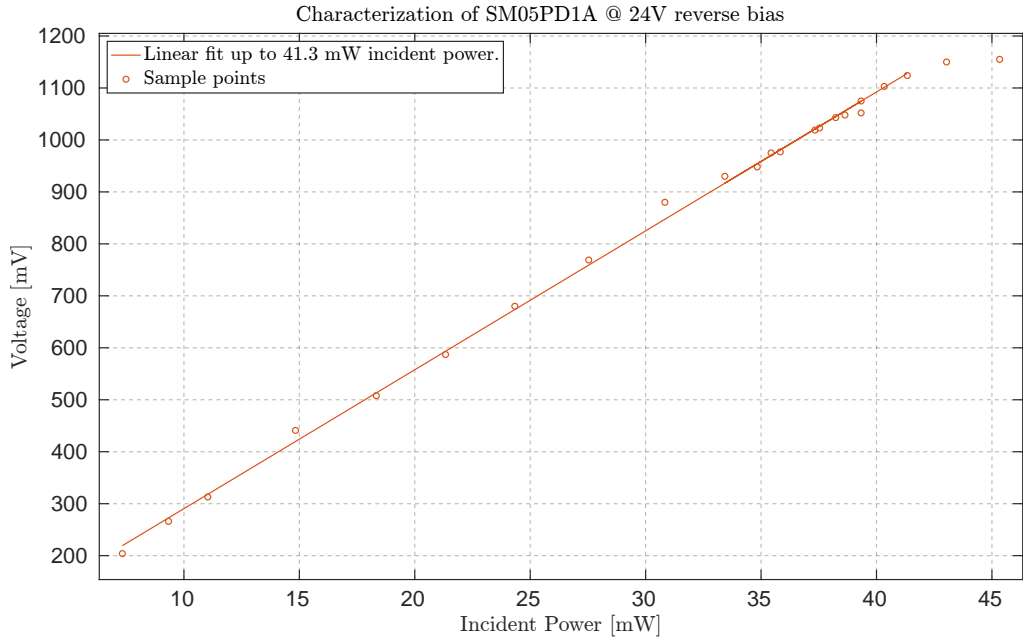


Figure 3.13: Characterization of the silicon photodiode FDS100, showing a linear response for chosen points up to 41.3 mW of incident power. Points where the photodiode is already saturated are excluded from the linear fit.

lead to an artificially lower shot noise level, potentially skewing the accuracy of the results.

### 3.5.2 Noise Characterization

Before delving into noise characterization, it is essential to differentiate between the various types of laser noise: shot noise, amplifier noise, and oscilloscope (or quantization) noise. Amplifier noise includes contributions from thermal (Johnson) noise and the amplifier's noise figure, increasing with the amplifier's gain and temperature. The noise power of the amplifier can be estimated as:

$$S_{\text{amp}} = (gR_{\text{load}})^2 I_{\text{Johnson}} \left( 10^{\text{NF}/10} - 1 \right) l_{\text{output}}, \quad (3.14)$$

where  $g$  is the amplifier's voltage gain,  $I_{\text{Johnson}}$  is the Johnson noise current, NF is the amplifier's noise figure, and  $l_{\text{output}}$  is the output loss factor. On the other hand, oscilloscope noise arises primarily from the quantization process and the oscilloscope's inherent noise floor. This includes limitations due to the number of bits used and the voltage resolution. The oscilloscope's power spectral density can be obtained by normalizing the RMS noise by its bandwidth. Oscilloscope noise can be reduced or minimized by choosing a high voltage resolution (e.g. a small voltage per division), e.g. zooming in on the oscilloscope as much as

possible. With the correction settings on the oscilloscope, the analysis reveals that shot noise is the dominant noise source, allowing us to neglect oscilloscope and amplifier noise in the following discussions safely.

The next step involves carrying out the noise measurement with the chosen photodiodes. During the initial setup, it was discovered that directly amplifying the photodiode's output voltage caused the oscilloscope to overload. A low-pass filter rated at 15 MHz—about 5 MHz below the laser's repetition frequency—was used to solve this. Since the RIN spectrum for solid-state lasers is usually much higher at low frequencies than the shot noise limit at high frequencies, it's challenging to analyze the whole spectrum in a single, sensitive measurement. To address this, we measured the RIN in both the low- and high-frequency regions separately, using different amplifiers optimized for each range. The power spectral densities from these measurements were then combined during post-processing. This noise measurement approach is similar to the method used in a previous study by Camenzind et al. [40].

### Low-Frequency Region

For the frequency range from 1 Hz to 100 kHz, we employed the DLPCA-200 transimpedance amplifier, set to a gain of 30 dB. This amplifier operates with a flat amplification profile from 1 Hz (DC) to 500 kHz. The DLPCA-200 is characterized by low noise, with an input noise voltage of  $4 \frac{\text{nV}}{\sqrt{\text{Hz}}}$ .

To convert the signal from voltage to dBc/Hz, we require the carrier spectral density  $S_c(f)$  and the signal spectral density  $S_V(f)$ . The carrier density is obtained by terminating the amplifier output with a  $50\Omega$  resistor and measuring the resulting DC voltage  $V_{\text{DC}}$  using a multimeter. The amplifier is then switched to AC coupling, so the oscilloscope does not overload. The carrier spectral density is calculated as follows:

$$S_c = \left( V_{\text{DC}} \cdot \frac{1}{2} \right)^2, \quad (3.15)$$

where the factor of  $1/2$  accounts for the effective resistance. The signal power spectral density  $S_V(f)$  is derived from the time-discrete signal, which is sampled at a rate  $f_s$  with  $N$  data points:

$$S_V(f) = \frac{|\mathcal{F}V(f)|^2}{Nf_s}, \quad (3.16)$$

which, like the carrier PSD, is expressed in units of volts squared. The spectral noise density is then calculated as:

$$S(f) = 10 \log_{10} \left( \frac{S_V(f)}{S_c} \right). \quad (3.17)$$

### High-Frequency Region

For frequencies above 60 kHz, the DUPVA 1-70 voltage amplifier was utilized, which provides a flat amplification profile up to multiple GHz. The flat amplification profile starting from 60 kHz has been experimentally confirmed in past experiments. In this higher frequency region, the measurement procedure is adjusted slightly, as only the AC part of the signal is amplified. The DC component is split off with a Bias-T, then terminated with a  $50 \Omega$  resistor, and measured with a multimeter for normalization.

When calculating the carrier spectral density in this region, the actual gain of the voltage amplifier must be considered. Although the DUPVA 1-70 was expected to deliver a 40 dB gain (corresponding to a voltage gain  $g = 100$ ), subsequent measurements revealed an actual gain of  $g \approx 86.23$ , corresponding to an amplification of 38.17 dB. Accounting for this, the carrier spectral density is given by:

$$S_c = (gV_{DC})^2. \quad (3.18)$$

To obtain a meaningful shot noise level, the DC voltage measured with this voltage amplifier is used. The shot noise level can be determined using:

$$S_{\text{shot}} = 10 \log_{10} \left( 2q \frac{R}{V_{DC}} \cdot 1 \text{ Hz} \right), \quad (3.19)$$

where  $R = 50 \Omega$  is the termination resistance and  $q$  is the electron charge. For the laser presented in this work, the shot noise limited detection is  $S_{\text{shot}} = -162 \text{ dBc/Hz}$ .

### Optimizing Sampling Rate for Accurate Noise Measurement

To conduct a meaningful noise measurement, a crucial factor to consider is the sampling rate of the measuring device—in this case, Teledyne Lecroy’s WavePro 254HD oscilloscope, which supports up to 20 gigasamples per second (GS/s). According to the *Nyquist-Shannon sampling theorem* [41], the sampling rate must be greater than twice the signal bandwidth to ensure accurate signal reconstruction and avoid aliasing. Given that we expect the laser’s noise to approach the shot-noise limit around the MHz frequencies—frequencies beyond which are less relevant for our purposes—one might initially assume that a sampling rate of a few megasamples per second would suffice to capture all relevant noise components. However, this assumption can be misleading.

To clarify this, it is useful to state the theorem more precisely in Shannon’s original form:

**Theorem 3.1** (Nyquist-Shannon Sampling Theorem). *If a signal  $x(t)$  contains no frequencies higher than  $B$  Hertz, then it can be completely reconstructed by a sequence of points spaced less than  $\frac{1}{2B}$  seconds apart.*

Thus, assuming that there is no significant information above a few megahertz could be problematic. Aliasing can cause noise from higher frequencies to be sampled in a way that it appears at lower frequencies, potentially interfering with the measurements at frequencies of interest. This is why merely selecting a low sampling rate may not be sufficient; careful consideration of the highest frequencies present in the signal is essential to avoid misinterpreting the noise characteristics.

The careful reader might also wonder why the highest available sampling rate was not used. There are practical constraints, such as the maximum data file size and the speed at which the data can be processed. The oscilloscope allows for saving up to  $5 \times 10^9$  data points per run, which inherently limits the duration of the measurement and, consequently, the minimum frequency that can be probed. Therefore, the goal is to choose the lowest sampling rate that avoids aliasing while maximizing the measurement duration.

A series of experiments were conducted to determine the optimal sampling rate for measuring the noise spectral density of the laser. Noise measurements were compared under two conditions: *a*) with the laser light input and *b*) with the laser light blocked. Figures 3.14 through 3.18 display these comparisons, each consisting of three subplots: the top subplot shows the noise spectral density with the laser light input, with the raw Fourier transform in grey and the averaged trace in orange (see Chapter 3.5.2 for the averaging procedure). The middle subplot shows the noise measurement with the beam blocked, again in raw (grey) and averaged (orange) traces. The bottom subplot presents the difference between the raw traces (grey) and the averaged traces (orange), with a black horizontal line indicating the zero mark.

The results indicate that a sampling rate of 250 MS/s is the minimum practical rate to balance the need to avoid aliasing with manageable data size and processing speed. At lower rates, such as 50 MS/s, the measured spectrum showed no meaningful data at 1 MHz, as evidenced by the meagre difference between the traces, indicating inadequate signal capture. A noticeable difference between the traces was only observed at sampling rates of 250 MS/s or higher.

Note that each trace consists of exactly  $10^8$  data points. The first trace, recorded with a sampling rate of 50 MS/s, spans a duration of 2000 ms, while the last trace, recorded at a sampling rate of 1 GS/s, covers only 100 ms. This consistent data size ensures that the results are directly comparable.

Because the x-axis is kept constant, the lowest possible frequency component is determined by the 50 MS/s sampling rate experiment, yielding  $\frac{1}{2000\text{ms}} = 0.5\text{ Hz}$ . The highest possible frequency component is dictated by the Nyquist-Shannon sampling theorem (see Theorem 3.1), which for the 1 GS/s trace is  $\frac{1\text{GS/s}}{2} = 0.5\text{ GHz}$ . Consequently, none of the previous experiments can access the full frequency range from 0.5 Hz to 0.5 GHz.

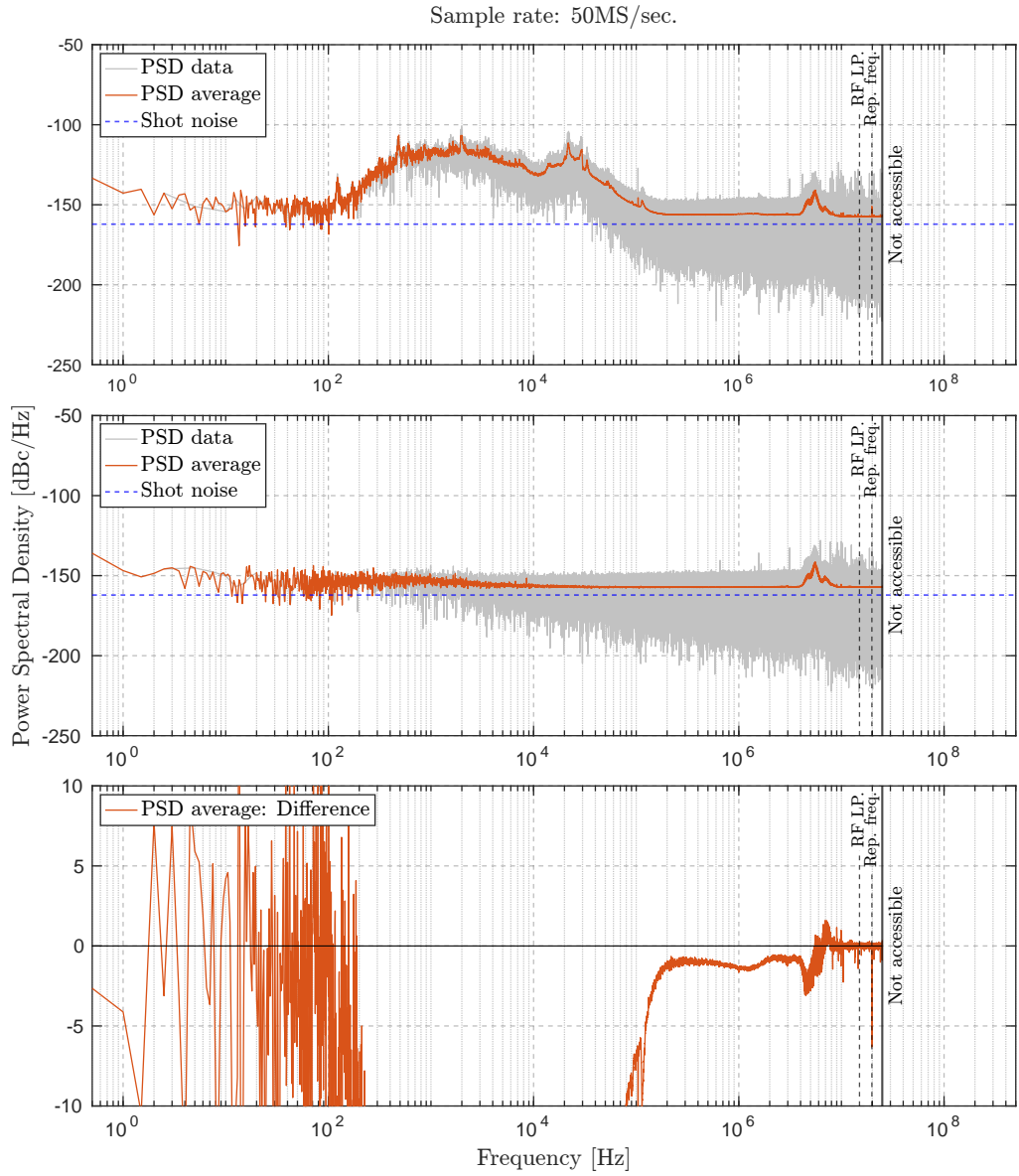


Figure 3.14: Noise measurement comparisons at a sampling rate of 50 MS/s: Top subplot shows the laser light input; middle subplot shows the blocked beam; bottom subplot displays the difference between raw and averaged traces. At this rate, the oscilloscope fails to capture meaningful data above 1 MHz because the difference is too low with 1 dB, indicating inadequate sampling.

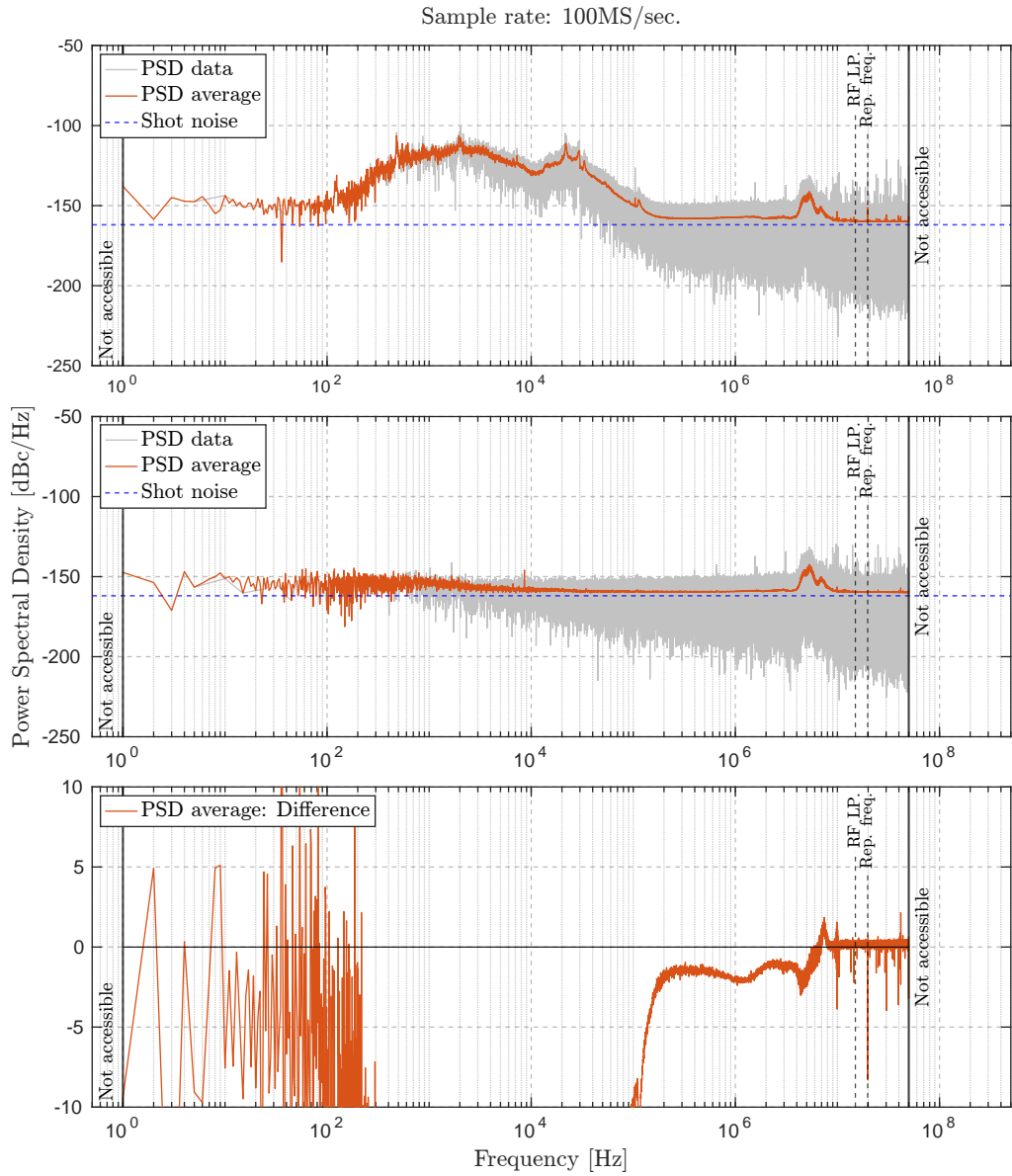


Figure 3.15: Noise measurement comparisons at a sampling rate of 100 MS/s: Top subplot shows the laser light input; middle subplot shows the blocked beam; bottom subplot displays the difference between raw and averaged traces. The higher sampling rate captures more accurate data than 50 MS/s but still shows signs of aliasing at higher frequencies.

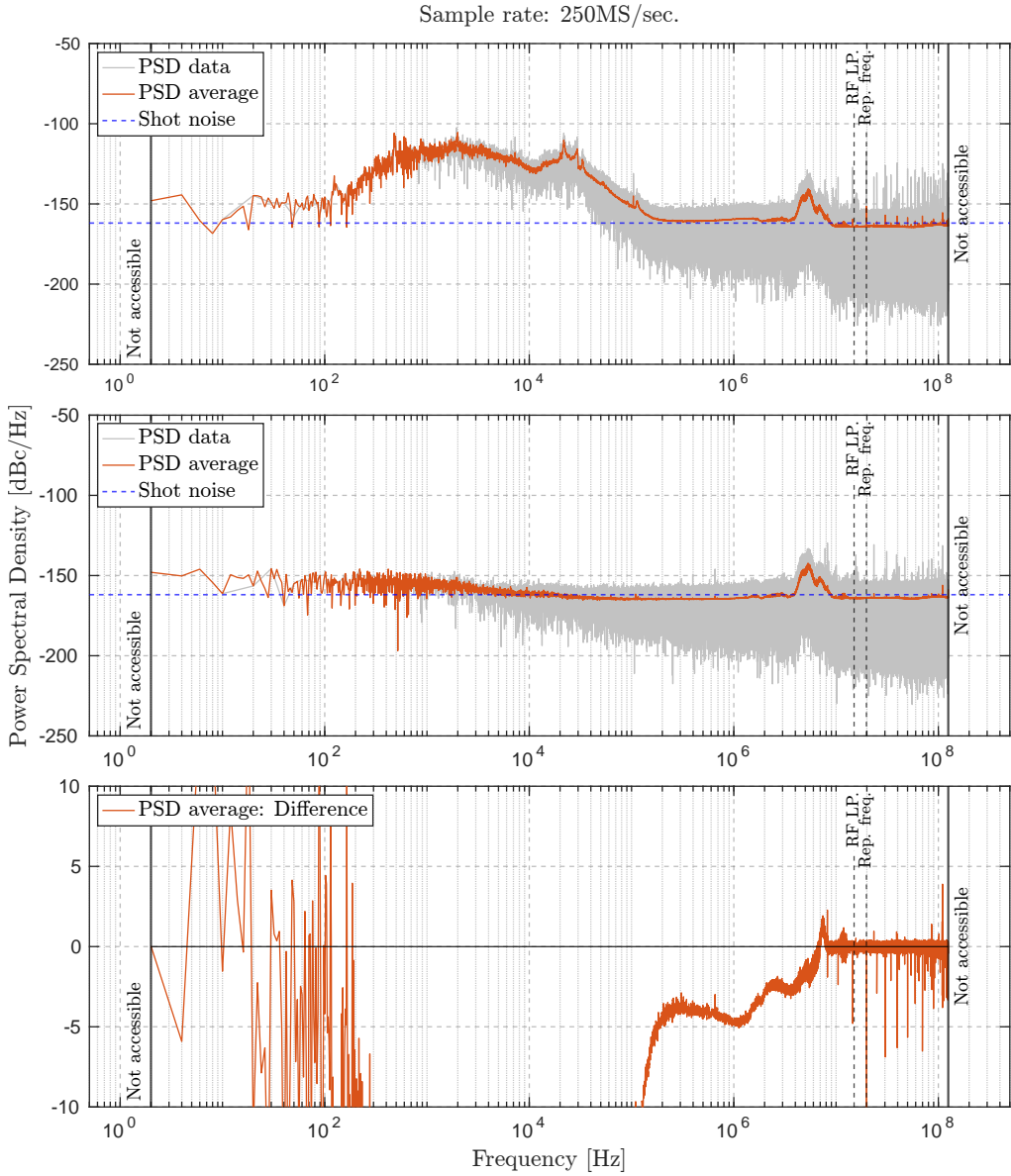


Figure 3.16: Noise measurement comparisons at a sampling rate of 250 MS/s: Top subplot shows the laser light input; middle subplot shows the blocked beam; bottom subplot displays the difference between raw and averaged traces. Due to the difference of around 5 dB between the averages of the traces, this sampling rate is identified as the minimum practical rate to avoid aliasing while maintaining manageable data size and processing speed.

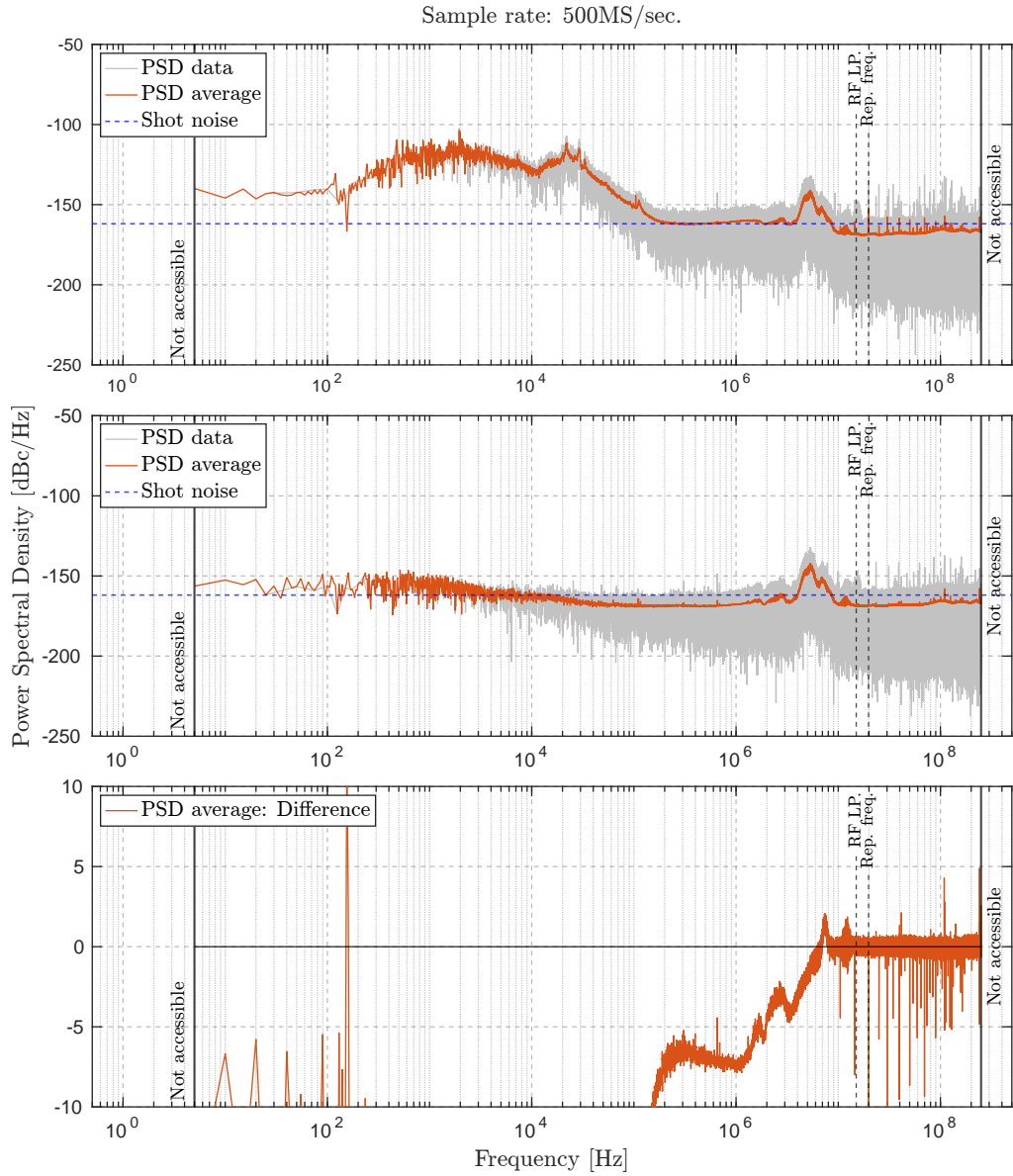


Figure 3.17: Noise measurement comparisons at a sampling rate of 500 MS/s: Top subplot shows the laser light input; middle subplot shows the blocked beam; bottom subplot displays the difference between raw and averaged traces. Aliasing effects are further reduced at this sampling rate, though larger data size may limit measurement duration.

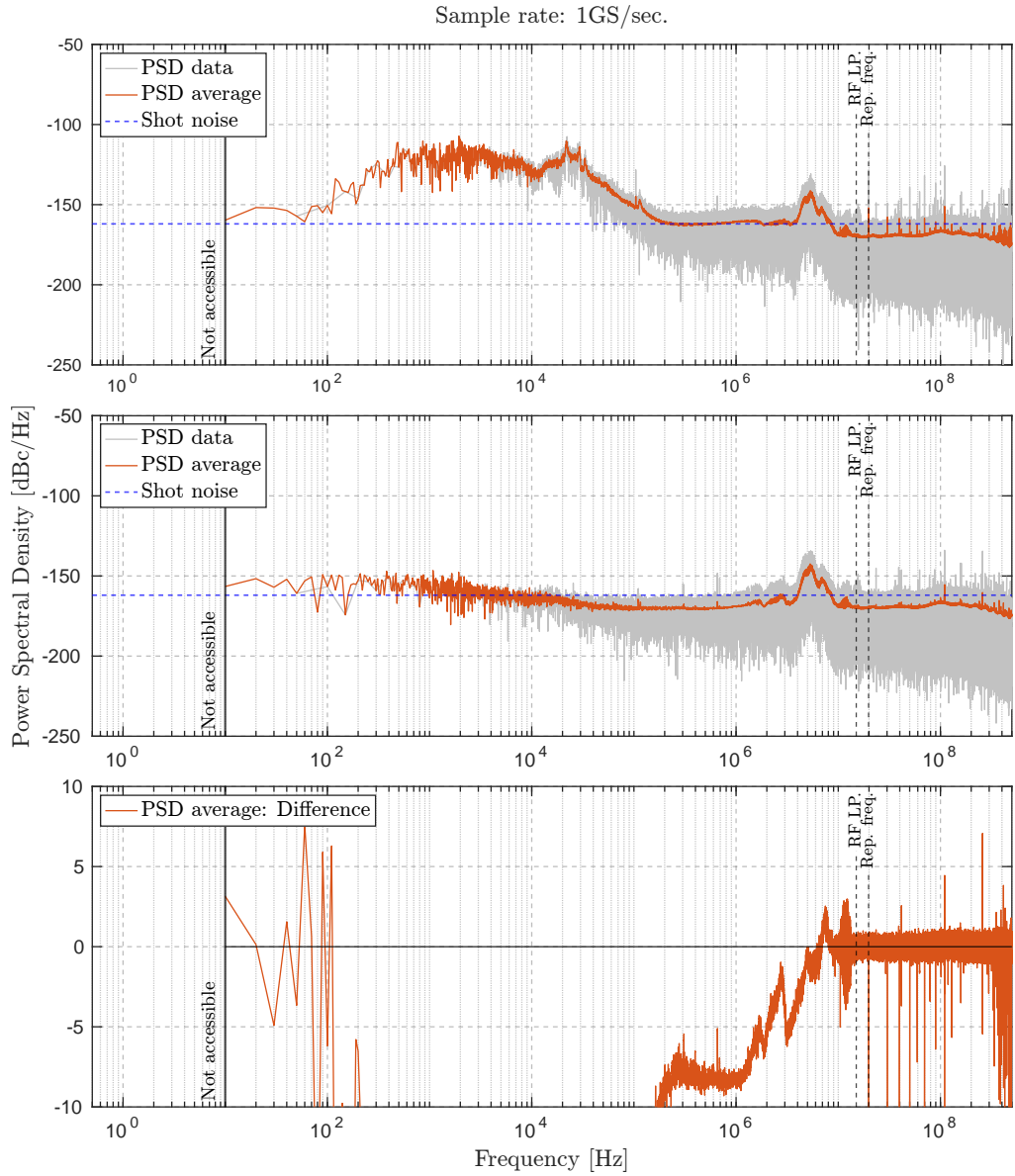


Figure 3.18: Noise measurement comparisons at a sampling rate of 1 GS/s: Top subplot shows the laser light input; middle subplot shows the blocked beam; bottom subplot displays the difference between raw and averaged traces. The highest sampling rate provides the most accurate data but at the cost of reduced measurement duration due to data size limitations.

### Resulting Noise Measurement

Based on the preceding discussions and the collected data, a good noise measurement can be conducted. Two traces were measured, one for each amplifier, and they are overlapped in the frequency range from 20 kHz to 500 kHz to determine the optimal switching point. Referring to the upper part of Figure 3.19, the blue trace represents the raw Power Spectral Density of the low-frequency part, while the orange trace corresponds to the raw PSD of the high-frequency part. The bottom part of the figure shows the averaged traces.

It is important to note that both traces were recorded with different sampling rates and measurement times, resulting in different frequency vector spacing for each measurement. This results in a spacing of 0.1 Hz for the lower frequency part, while the high-frequency measurement has a spacing of 20 Hz. The averaging procedure was chosen to smooth the data while preserving key characteristics. The details are provided in Table 3.2.

Table 3.2: Averaging settings for noise measurements.

Measurement Range	Low-Frequency	High-Frequency
Raw Data Range	Frequencies below 10 Hz	Frequencies below 10 kHz
Averaging Interval	10 Hz to 1 kHz: 100 logarithmically spaced intervals	10 kHz to 1 MHz: 100 logarithmically spaced intervals
Averaging Method	Moving average with sample points based on central interval: data points within 0.3% of the central frequency	Moving average with sample points based on central interval: data points within 0.2% of the central frequency
Fixed Averaging above...	...1 kHz: Fixed 59 sample points (5.9 Hz)	...1 MHz: Fixed 195 sample points (3.9 kHz)

These smoothing settings help to make trends more visible while preserving key characteristics, such as the harmonics of the repetition frequency. Due to the generally noisy nature of the data, finding an adequate averaging method can be challenging. Appendix 4 compares different methods for computing the average of the trace and provides details on the exact number of sample points taken for the average. Now that good settings have been found, the trace can be stitched together. A stitching mark at 80 kHz has been identified as optimal, as shown in Figure 3.20.

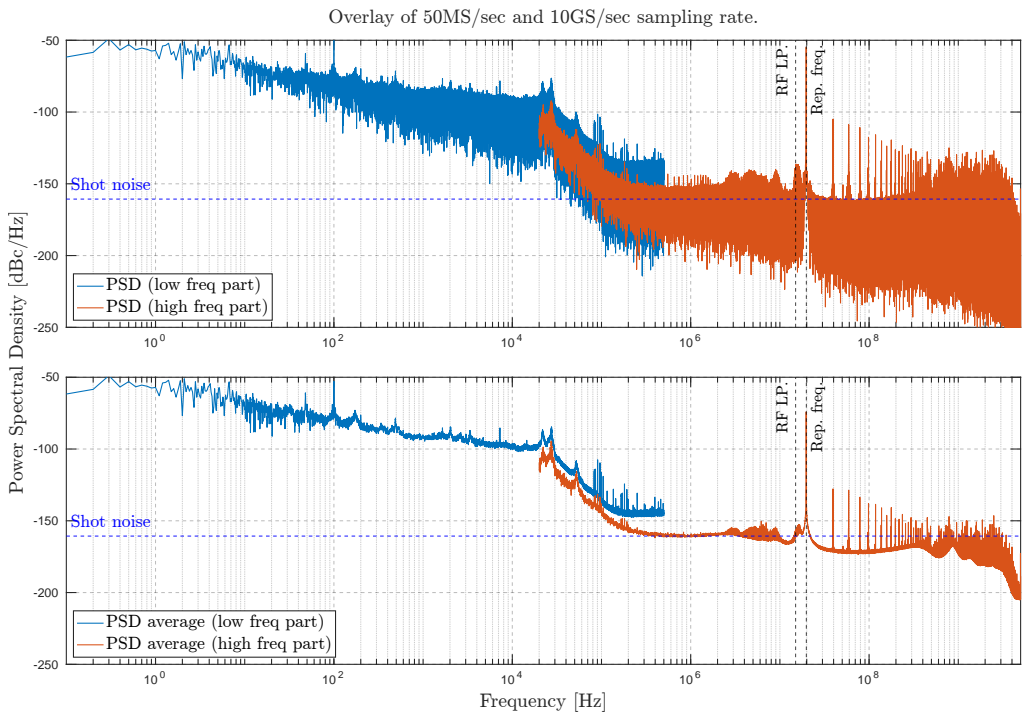


Figure 3.19: Top: The overlay of both raw traces for 50 MS/s and 1 GS/s sampling rates. The blue part represents the low-frequency measurement done with the DLPCA-200 amplifier, while the orange trace represents the high-frequency measurement done with the DUPVA1-70 amplifier. The range from 20 kHz to 500 kHz shows both traces. Bottom: A moving average has been applied over both traces to smooth the data with the procedure as explained above.

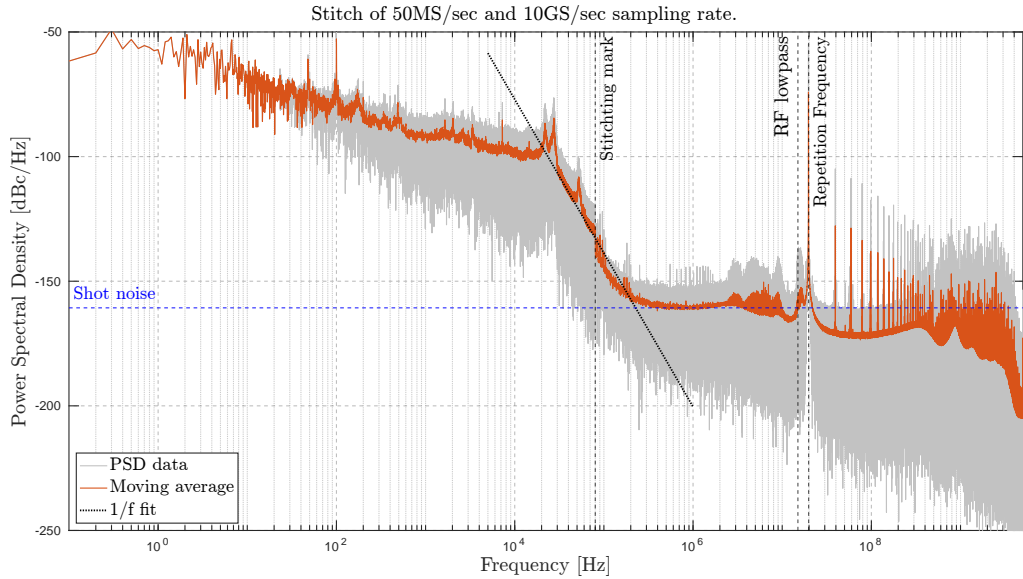


Figure 3.20: The stitch of both prior noise measurements at the stitching mark of 80 kHz. Grey represents the raw PSD data, while orange represents the moving average, according to the abovementioned procedure. A  $1/f$  fit is applied to show that the laser noise exhibits a  $1/f$  behaviour from 2 kHz to 200 kHz.

The averaged traces show a slight shift in power spectral density with respect to each other, which becomes even more apparent when stitched together. The  $1/f$  fit takes on a value of -200 dBc/Hz, which matches well with the expected real shot noise level of our TDL: If 7 mW incident power results in -162 dBc/Hz, then we expect 60 W to result in:

$$S_{\text{shot}}^{\text{true}} = -162 \text{ dBc/Hz} + 10 \log_{10} \left( \frac{7 \text{ mW}}{60 \text{ W}} \right) = -201.33 \text{ dBc/Hz}. \quad (3.20)$$

### 3.6 Technical Considerations

In this section, technical considerations are addressed, and while not directly related to the core research, they are crucial for successful experimentation. These practical aspects can often become sources of frustration in the lab, as they are necessary but can be more challenging than anticipated. By sharing these insights, I hope to shed light on some of the unexpected daily challenges that can arise and potentially delay progress in the project.

As previously mentioned, most of the laser's power will be directed into a hollow-core photonic crystal fibre (HCPCF), where the spectral broadening will occur. Given that this power is approximately 50 W, several precautions are necessary to prevent damage to the fibre. Additionally, the photodiode used for

noise measurement must be actively protected, as small spectral drifts could significantly increase the incident power, posing a risk of damaging the photodiode.

The HCPCF is integrated with GLOphotonic's Powerlink system, which offers a comprehensive solution allowing for pressures up to 30 bars, 50 W average input power, and water-cooling at the input side, all while maintaining a transmission efficiency of  $> 85\%$ . The fibre has a specified mode-field diameter (MFD) of  $42\mu\text{m}$ , necessitating precise beam collimation to match this size. However, improper positioning or angling of the laser beam can cause immediate and irreversible damage to the fibre, making active beam stabilization crucial.

### 3.6.1 Beam Stabilization

An active laser beam stabilization system from MRC is employed to achieve the required precision, utilizing a combination of two 4QD detectors and two controllable mirrors, referred to as actuators. Figure 3.21 illustrates the setup schematically.

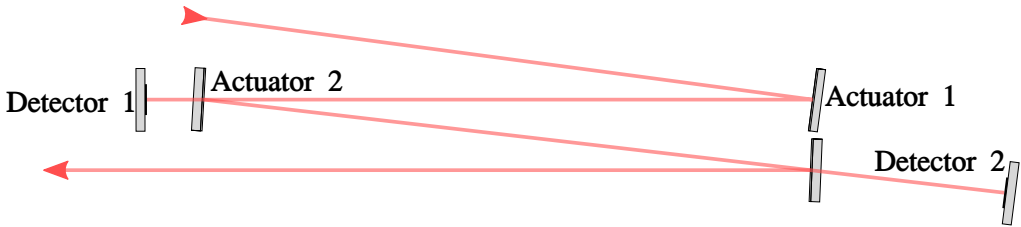


Figure 3.21: Schematic of the beam stabilization setup. The system utilizes two 4QD detectors and two actuators to stabilize the laser beam actively. Detector 1 receives input from the leakage of actuator 2, while detector 2 receives input from a subsequent mirror. The detectors continuously adjust the actuators to maintain the beam's position, compensating for any fluctuations in beam-pointing and ensuring precise alignment.

After being reflected by actuator 1, the laser beam reaches actuator 2, which then reflects it to the subsequent mirror. The movement of actuator 1 is controlled by detector 1, which receives input from the leakage of the mirror in front of actuator 2. Both detectors adjust their corresponding actuators to ensure the signal remains centred on their four photodiodes. This configuration compensates for beam-pointing fluctuations, thereby minimizing variations in beam position and angle.

To verify the effectiveness of the stabilization system, the fluctuations in beam position were compared with the stabilization system turned on and off. Figure 3.22 compares the unstabilized and stabilized horizontal and vertical positions.

As shown, the beam stabilization reduces the positional standard deviation from  $3.59\mu\text{m}$  and  $4.04\mu\text{m}$  to  $1.48\mu\text{m}$  and  $1.21\mu\text{m}$ , respectively, for the uncol-

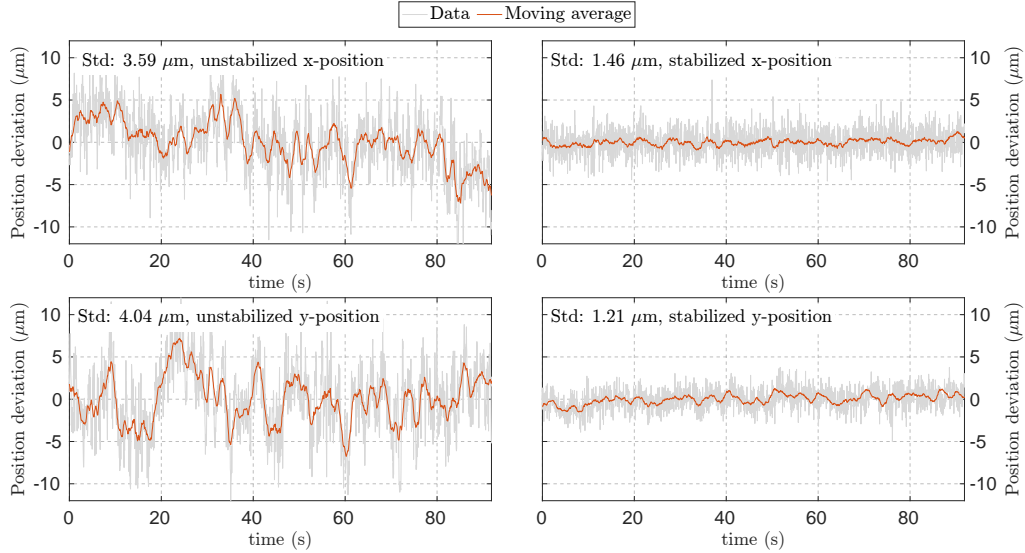


Figure 3.22: Comparison of beam position fluctuations in both x and y directions with and without active stabilization. The plots on the left show the fluctuations without stabilization, while the plots on the right show the reduced fluctuations with stabilization applied. The standard deviation for each case is indicated within the plots, demonstrating the effectiveness of the stabilization system in minimizing beam drift. The moving average is each over 30 data points, averaging over 1.3 seconds.

limited beam. This demonstrates that the laser beam fluctuations have been minimized to a safe level for directing the full signal into the fibre without causing damage. When we initially directed more than 5 W of power into the fibre, the laser occasionally shut down unexpectedly, triggering the interlock without an apparent cause. The issue was traced to the reflection of the fibre facet, which created a secondary light spot on the detectors. This caused the detectors to incorrectly interpret the beam position as outside their operational range. A straightforward solution was moving the detector away from the leaking mirror, ensuring the back-reflection bypassed the detector's sensitive area.

### 3.6.2 Interlock: Pump Diode

When the active laser beam stabilization system functions correctly, the laser beam couples into the fibre as intended. However, if there are significant drifts in the beam path, the beam position may move outside the working range of the actuators, rendering them unable to compensate for the misalignment. In such cases, the detectors may detect insufficient power, causing the actuators to default to a "zero position," which leads to the stabilization system shutting down. If the beam is accidentally blocked or the control system loses power, the piezo motors

drive the actuators to an extreme position. Both scenarios risk damaging the fibre and other optical components, making manual laser shutdown too slow to prevent potential damage. To address this, an interlock system has been implemented. Under normal operating conditions, the interlock circuit of the laser pump diode remains closed, allowing the pump laser to continue pumping the TDL gain medium. However, if any of the scenarios above occur, the circuit is opened, immediately stopping the pump diode and shutting down the laser. While this process is not instantaneous, it significantly reduces the risk of damage. The control system outputs a 5V signal when everything is functioning correctly or if the system has not been activated. Still, no signal is sent when the actuators are in the zero or extreme position, effectively serving as a TTL signal. This setup is easily managed using a solid-state relay (SSR). We initially experimented with MOSFETs and optocouplers, but they struggled to handle the 24V present between the interlock pins. The SSR proved ideal, as it can handle load voltages up to 230V.

However, in this configuration, the laser would never turn on because the beam stabilization cannot function without an active laser, and the pump diode cannot be activated without beam stabilization. To resolve this, a simple override switch was added to the system. The override temporarily bypasses the interlock, allowing the laser to turn on and the beam stabilization to operate. Once the stabilization is operational, the override switch is deactivated. The response time between the low TTL signal and the pump diode reaction is expected to be within the millisecond range, although it hasn't been explicitly measured. This interlock system provides the fastest safety mechanism to be implemented with relative ease and minimal complexity.

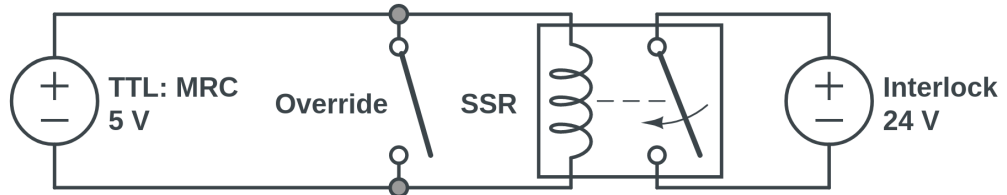


Figure 3.23: Electrical circuit of the pump diode interlock system, illustrating the components involved in safeguarding the laser setup. The circuit includes a 5V TTL voltage source, an override switch, a solid-state relay (SSR), and a 24V interlock. This configuration ensures that the pump diode is shut down in case of beam misalignment or stabilization failure, preventing potential damage to the fibre and optical components. The override switch allows for a controlled startup sequence, temporarily bypassing the interlock to activate the laser and stabilization system.

With this system in place, the only light that could potentially damage the

fibre or other optical components after an error is detected is the residual light already oscillating within the cavity.

### 3.6.3 Interlock: Photodiode

After the light exits the fibre, it passes through a grating spectrometer, which allows for the selection of a specific wavelength range of the spectrum using a narrow slit. As shown in Figure (2.7), the power within a 1nm slice of the spectrum can reach up to 3W. However, since the high-gain region typically exhibits lower power levels, this is the area where we aim to conduct the noise measurement using the photodiode. The challenge arises when the selected spectral slice shifts slightly, potentially moving into a region with higher power per nanometer. This shift could significantly increase the incident power on the photodiode, risking its destruction. To mitigate this risk, a second photodiode operating at a power level below the maximum incident power is used, which still ensures a linear voltage response. In the event of a spectral shift, the incident power on both photodiodes will increase. However, before the power reaches a level that could damage the noise-measuring photodiode, the second photodiode will trigger a warning that blocks the light. This interlock system is effective for gradual drifts, a conclusion supported by testing the setup over several hours of laser operation. The second photodiode generates a voltage signal serving as input to an MKRzero Arduino, functioning as an analog-to-digital converter (ADC). By defining an appropriate threshold voltage, the system controls a rotation mirror mount equipped with a D-shaped mirror. Depending on whether the voltage exceeds or falls below the threshold, the mirror rotates by 180°, effectively blocking or allowing the light to continue.

## Full Setup

Figure 3.24 provides a schematic overview of the experimental setup. This illustration includes key components such as active beam stabilization, power and polarization control, water cooling, and the grating spectrometer. The laser cavity, noise measurement, and diagnostic elements are represented schematically.

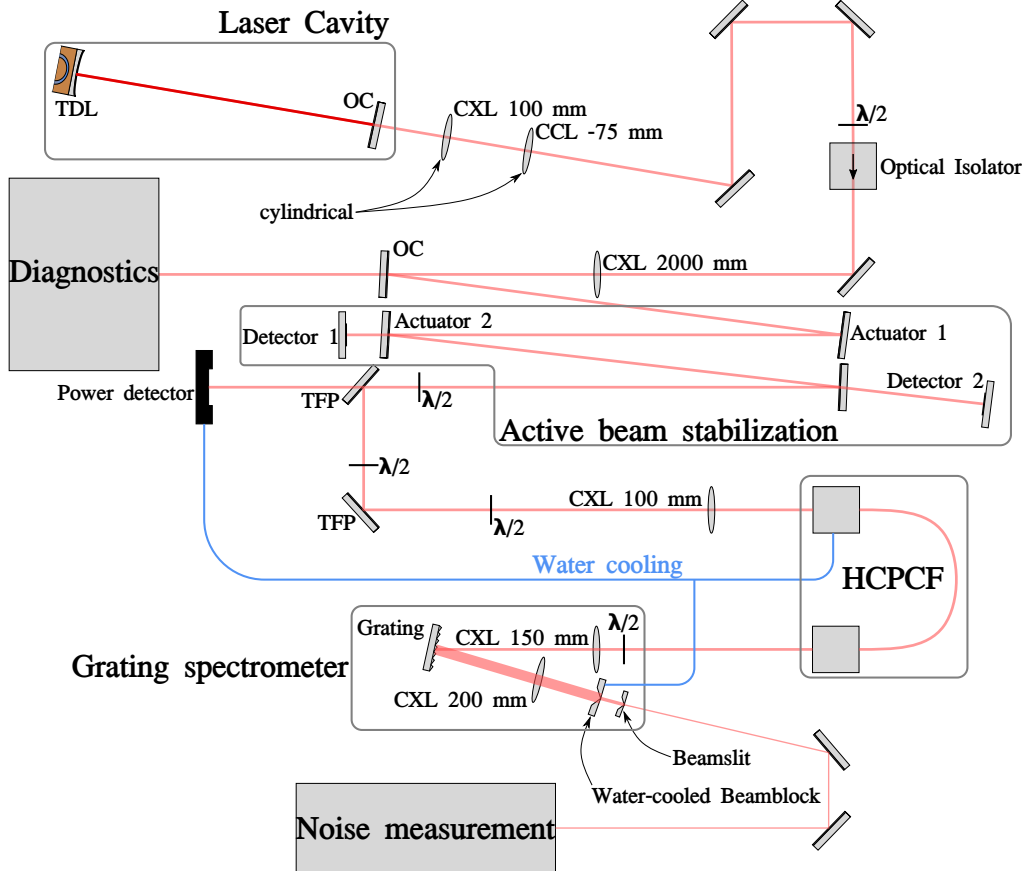


Figure 3.24: Schematic of the complete experimental setup, highlighting the active beam stabilization, power and polarization control, water cooling, and the grating spectrometer (distances not to scale). The laser cavity, noise measurement, and diagnostic components are shown schematically. CXL: convex lens, CCL: concave lens,  $\lambda/2$ : half-wave plate, OC: output coupler, TFP: thin-film polarizer, HCPCF: hollow-core photonic crystal fibre.

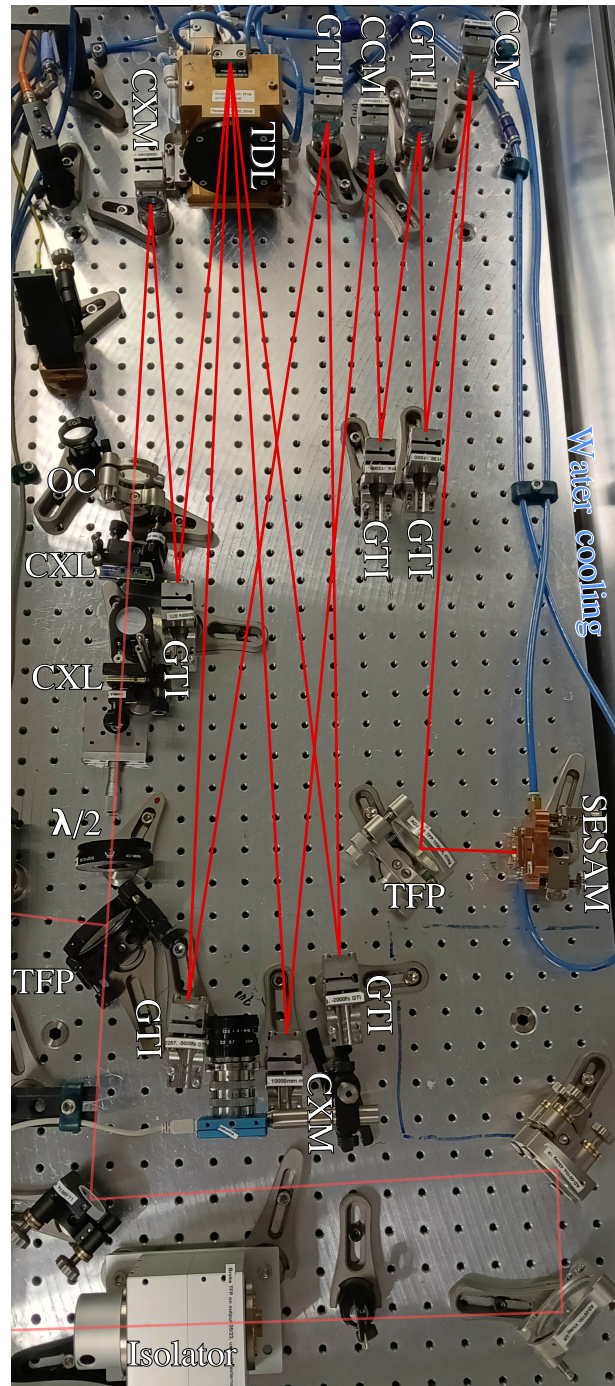


Figure 3.25: The final laser cavity as seen in the laboratory. The dark red path traces the laser light oscillating in the cavity, while the bright red shows the outcoupled light, indicating that the output power is 10% of the intracavity power.

## CHAPTER 4

# Conclusion and Outlook

---

In this project, a mode-locked thin disk laser was successfully designed, built, and characterized. The laser achieved an average output power of 60 W, a pulse duration of 1030 fs, and a repetition rate of 19.7 MHz. Mode-locking was accomplished using a sapphire-bonded SESAM. The chosen repetition frequency enables measurements up to a few MHz without interference from the fundamental repetition frequency peak while maintaining high peak powers needed for strong spectral broadening.

Spectral broadening simulations were developed, accounting for inherent fluctuations in the average output power of TDLs and pressure-dependent nonlinear refractive indices. The power and gain densities were calculated, and optimal parameters were identified to elevate the noise of the system. The simulations suggest a noise gain of 35 dBc peak value and spectral broadening with a full width at half maximum (FWHM) from 1.5 nm to 25 nm. In the wings of the spectrum, 29 dBc noise gain is achievable. The pressure dependence of the resulting spectrum and noise density was discussed in detail. Modulation instabilities were thoroughly examined and were found not to pose significant problems theoretically.

A telescope was constructed for the coupling into the fibre. This was set up to achieve a beam waist radius of 21  $\mu\text{m}$  at the fibre input, and a cylindrical telescope was implemented to correct the ellipticity of the beam. An active beam stabilization system, consisting of two actuators and two detectors, was installed, effectively reducing beam position fluctuations from a standard deviation of 3.59  $\mu\text{m}$  and 4.04  $\mu\text{m}$  to 1.46  $\mu\text{m}$  and 1.21  $\mu\text{m}$ , respectively. Polarization and power control into the fibre were achieved using a combination of thin-film polarizers and half-wave plates, resulting in a coupling efficiency of 82% at 36 W input power. The gas pressure system was tested but found to leak at a non-negligible rate, which prevented the final noise measurement (see below for details). A grating spectrometer, including a water-cooled beam block and custom slits, was designed and built with a predicted wavelength resolution of half a nanometer. Two different silicon photodiodes were characterized and tested.

The signal acquisition chain was developed to measure the shot-noise limit

of the laser at high (MHz) frequencies. Overloading made measurements with a signal source analyzer impossible due to the need to measure close to the repetition rate of the laser. Therefore, an oscilloscope was used for the final noise measurement. Here, the influence of different low-pass filters, voltage amplification and its added noise, and oscilloscope digitization noise was studied. To measure the achieved shot-noise level of  $-162$  dBc/Hz, optimal amplification and settings were determined. Furthermore, the final noise measurement, which consisted of two different measurement processes for low and high frequencies with different settings, was discussed. Here, the averaging of the signal is of increased importance when compared with SSA measurements.

Several interlocks were designed and implemented to prevent damage to electrical or optical components. One interlock protects the pump diode, and therefore the fibre, by using feedback from the beam stabilization stage, while another protects the photodiodes using an Arduino-controlled D-mirror.

Looking ahead, the immediate next steps are clear. At the time of writing, the fibre is still being repaired in France to address the gas leakage issue. Once the repair is complete, the following steps involve sending 50 W of average power through the fibre, using the grating spectrometer to select a specific wavelength range in the spectrum, and repeating the noise measurement with the settings identified as optimal. By comparing the unbroadened and broadened laser noise spectra, it should be possible to infer a record-low shot noise level (the lowest known to date to the best of our knowledge) of  $S_{\text{shot}} = (-162 - 29)$  dBc/Hz =  $-191$  dBc/Hz if measured in the wings, or  $S_{\text{shot}} = (-162 - 35)$  dBc/Hz =  $-197$  dBc/Hz if measured at the noise gain peak.

# Acknowledgements

I am sincerely grateful to Prof. Dr. Ursula Keller for allowing me to complete my master's thesis within her research group. Working on cutting-edge laser research has been an extraordinary experience, and I deeply value the time spent with the ULP group.

My deepest thanks go to my supervisor, Moritz Seidel, for his unwavering guidance throughout this thesis. His expertise and insights into the practical aspects of laser operation, especially thin-disk lasers, were invaluable. I am particularly thankful for the time he dedicated to answering my questions and his constructive feedback on the experimental work and the writing of this thesis.

I would also like to thank Dr. Christopher Phillips for his support in addressing the various challenges encountered in the lab and for the insightful discussions during the TDL meetings. His expertise in noise measurements and simulations was instrumental in advancing this work. I am also grateful to Sandro Camenzind for introducing me to Moritz and facilitating my initial contact with the ULP group. My heartfelt thanks go to all members of the ULP group for their warm and supportive attitude, which created an excellent learning and working environment. The high-quality equipment and positive atmosphere were crucial in acquiring valuable knowledge and experience for my future endeavours.

Finally, I thank my family and friends for their unwavering support throughout my studies. Their encouragement has been a constant source of strength and motivation.

# Bibliography

- [1] Encyclopaedia Britannica. “Laser - invention, light amplification, coherent beam.” Accessed: 28-July-2024. (2024), [Online]. Available: <https://www.britannica.com/technology/laser>.
- [2] T. H. Maiman, “Stimulated optical radiation in ruby,” *Nature*, vol. 187, p. 493, 1960. DOI: [10.1038/187493a0](https://doi.org/10.1038/187493a0).
- [3] M. C. Asplund *et al.*, “The 2018 nobel prize in physics: Optical tweezers and chirped pulse amplification,” *Analytical and Bioanalytical Chemistry*, vol. 411, no. 20, pp. 5001–5005, Aug. 2019, Epub 2019 May 29. DOI: [10.1007/s00216-019-01913-z](https://doi.org/10.1007/s00216-019-01913-z).
- [4] A. J. DeMaria *et al.*, “Self Mode-Locking of Lasers with Saturable Absorbers,” *Applied Physics Letters*, vol. 8, no. 7, pp. 174–176, Apr. 1966, ISSN: 0003-6951. DOI: [10.1063/1.1754541](https://doi.org/10.1063/1.1754541).
- [5] N. Picqué *et al.*, “Frequency comb spectroscopy,” *Nature Photonics*, vol. 13, no. 3, pp. 146–157, Mar. 2019. DOI: [10.1038/s41566-018-0347-5](https://doi.org/10.1038/s41566-018-0347-5).
- [6] U. Keller, *Ultrafast Lasers: A Comprehensive Introduction to Fundamental Principles with Practical Applications* (Graduate Texts in Physics). Springer International Publishing, 2022. DOI: [doi.org/10.1007/978-3-030-82532-4](https://doi.org/10.1007/978-3-030-82532-4).
- [7] S. Cuyvers *et al.*, “Mode-locked comb lasers for chip-scale spectroscopy,” *Compound Semiconductor*, 2021, Accessed: 2024-07-28.
- [8] M. Müller *et al.*, “10.4 kw coherently combined ultrafast fiber laser,” *Opt. Lett.*, vol. 45, no. 11, pp. 3083–3086, 2020. DOI: [10.1364/OL.45.003083](https://doi.org/10.1364/OL.45.003083).
- [9] P. Russbueldt *et al.*, “Compact diode-pumped 1.1 kw yb: Yag innoslab femtosecond amplifier,” *Opt. Lett.*, vol. 35, no. 24, pp. 4169–4171, 2010. DOI: [10.1364/OL.35.004169](https://doi.org/10.1364/OL.35.004169).
- [10] Y. Pfaff *et al.*, “Nonlinear pulse compression of a 200 mj and 1 kw ultrafast thin-disk amplifier,” *Optics Express*, vol. 31, no. 14, pp. 22 740–22 756, 2023. DOI: [10.1364/OE.489300](https://doi.org/10.1364/OE.489300).
- [11] S. Xu *et al.*, “High-repetition-rate and high-power efficient picosecond thin-disk regenerative amplifier,” *High Power Laser Science and Engineering*, vol. 12, e14, 2024. DOI: [10.1017/hpl.2023.97](https://doi.org/10.1017/hpl.2023.97).
- [12] A. Giesen *et al.*, “Scalable concept for diode-pumped high-power solid-state lasers,” *Applied Physics B*, vol. 58, no. 5, pp. 365–372, May 1994. DOI: [10.1007/BF01081875](https://doi.org/10.1007/BF01081875).

- [13] Y. Wang *et al.*, “High-power modelocked thin-disk oscillators as potential technology for high-rate material processing,” *Advanced Optical Technologies*, vol. 10, no. 4-5, pp. 247–261, 2021. DOI: [10.1515/aot-2021-0045](https://doi.org/10.1515/aot-2021-0045).
- [14] J. G. Sulewski, “Historical survey of laser dentistry,” *Dental Clinics of North America*, vol. 44, no. 4, pp. 717–752, 2000. DOI: [10.1016/S0011-8532\(22\)01317-9](https://doi.org/10.1016/S0011-8532(22)01317-9).
- [15] F. Emaury *et al.*, “Compact extreme ultraviolet source at megahertz pulse repetition rate with a low-noise ultrafast thin-disk laser oscillator,” *Optica*, vol. 2, no. 10, pp. 980–984, 2015. DOI: [10.1364/OPTICA.2.000980](https://doi.org/10.1364/OPTICA.2.000980).
- [16] R. Paschotta, *Tutorial: Fiber amplifiers*, RP Photonics Encyclopedia, Accessed: 2024-09-13, 2024.
- [17] M. Endo *et al.*, “Ultralow noise optical frequency combs,” *IEEE Journal of Selected Topics in Quantum Electronics*, vol. 24, no. 5, pp. 1–13, 2018. DOI: [10.1109/JSTQE.2018.2818461](https://doi.org/10.1109/JSTQE.2018.2818461).
- [18] P. Kwee *et al.*, “Optical ac coupling to overcome limitations in the detection of optical power fluctuations,” *Opt. Lett.*, vol. 33, no. 13, pp. 1509–1511, Jul. 2008. DOI: [10.1364/OL.33.001509](https://doi.org/10.1364/OL.33.001509).
- [19] M. J. Guy *et al.*, “Generation of femtosecond soliton pulses by passive mode locking of an ytterbium-erbium figure-of-eight fiber laser,” *Opt. Lett.*, vol. 18, no. 17, pp. 1447–1449, Sep. 1993. DOI: [10.1364/OL.18.001447](https://doi.org/10.1364/OL.18.001447).
- [20] H. A. Haus *et al.*, “Structures for additive pulse mode locking,” *J. Opt. Soc. Am. B*, vol. 8, no. 10, pp. 2068–2076, Oct. 1991. DOI: [10.1364/JOSAB.8.002068](https://doi.org/10.1364/JOSAB.8.002068).
- [21] “IEEE standard definitions of physical quantities for fundamental frequency and time metrology—random instabilities,” *IEEE Std Std 1139-2008*, pp. c1–35, Feb. 2009. DOI: [10.1109/IEEESTD.2008.4797525](https://doi.org/10.1109/IEEESTD.2008.4797525).
- [22] A. V. Oppenheim *et al.*, *Signals and Systems* (Prentice-Hall signal processing series). Prentice-Hall, 1983, Available: <https://books.google.ch/books?id=UQJRAAAAMAAJ>.
- [23] R. Paschotta, *Relative intensity noise*, RP Photonics Encyclopedia. DOI: <https://doi.org/10.61835/xx3>.
- [24] W. Schottky, “Über spontane stromschwankungen in verschiedenen elektrizitätsleitern,” *Annalen der Physik*, vol. 362, no. 23, pp. 541–567, 1918. DOI: <https://doi.org/10.1002/andp.19183622304>.
- [25] M. Seidel *et al.*, “Ultrafast yb:yag laser oscillator with gigahertz repetition rate,” *Opt. Express*, vol. 31, no. 21, pp. 34 313–34 324, Oct. 2023. DOI: [10.1364/OE.503697](https://doi.org/10.1364/OE.503697).
- [26] J. M. Dudley *et al.*, “Supercontinuum generation in photonic crystal fiber,” *Rev. Mod. Phys.*, vol. 78, pp. 1135–1184, 4 Oct. 2006. DOI: [10.1103/RevModPhys.78.1135](https://doi.org/10.1103/RevModPhys.78.1135).

- [27] M. Seidel *et al.*, “Factor 30 pulse compression by hybrid multipass multplate spectral broadening,” *Ultrafast Science*, vol. 2022, 2022. DOI: [10.34133/2022/9754919](https://doi.org/10.34133/2022/9754919).
- [28] J. Kerr, “Xl. a new relation between electricity and light: Dielectrified media birefringent,” *The London, Edinburgh, and Dublin Philosophical Magazine and Journal of Science*, vol. 50, no. 332, pp. 337–348, 1875. DOI: [10.1080/14786447508641302](https://doi.org/10.1080/14786447508641302).
- [29] R. Paschotta, *Nonlinear index*, RP Photonics Encyclopedia. DOI: [10.61835/ks8](https://doi.org/10.61835/ks8)?title="Thislinkwillreloadthecurrentpage..
- [30] G. P. Agrawal, *Nonlinear Fiber Optics*, 6th. San Diego: Academic Press, 2019, ISBN: 978-0-12-817042-7.
- [31] C. Brée *et al.*, “Method for computing the nonlinear refractive index via keldysh theory,” *Quantum Electronics, IEEE Journal of*, vol. 46, pp. 433–437, May 2010. DOI: [10.1109/JQE.2009.2031599](https://doi.org/10.1109/JQE.2009.2031599).
- [32] Á. Börzsönyi *et al.*, “Measurement of pressure dependent nonlinear refractive index of inert gases,” *Optics Express*, vol. 18, no. 25, pp. 25 847–25 854, Dec. 2010. DOI: [10.1364/OE.18.025847](https://doi.org/10.1364/OE.18.025847).
- [33] R. Paschotta, *B integral*. DOI: [10.61835/0qm](https://doi.org/10.61835/0qm).
- [34] M. Seidel *et al.*, “Ultrafast 550-W average-power thin-disk laser oscillator,” *Optica open*, May 2024. DOI: [10.1364/opticaopen.25745457.v1](https://doi.org/10.1364/opticaopen.25745457.v1).
- [35] R. Paschotta, *Gires–tournois interferometers*. DOI: [10.61835/zgy](https://doi.org/10.61835/zgy).
- [36] A. Diebold *et al.*, “Gas-lens effect in kw-class thin-disk lasers,” *Opt. Express*, vol. 26, no. 10, pp. 12 648–12 659, May 2018. DOI: [10.1364/OE.26.012648](https://doi.org/10.1364/OE.26.012648).
- [37] R. Paschotta, *M<sup>2</sup> Factor – RP Photonics Encyclopedia*, RP Photonics, Accessed: 2024-08-04, 2024. DOI: [10.61835/zxz](https://doi.org/10.61835/zxz).
- [38] Thorlabs, *Reflective diffraction gratings*, [https://www.thorlabs.com/newgroupage9\\_pf.cfm?guide=10&category\\_id=&objectgroup\\_id=8627](https://www.thorlabs.com/newgroupage9_pf.cfm?guide=10&category_id=&objectgroup_id=8627), Accessed: 2024-08-04.
- [39] Thorlabs, *FDS100 Si Photodiode Data Sheet*, Accessed: 2024-08-21, 2024.
- [40] S. L. Camenzind *et al.*, “Free-running yb:kyw dual-comb oscillator in a mopa architecture,” *Opt. Express*, vol. 31, no. 4, pp. 6633–6648, Feb. 2023. DOI: [10.1364/OE.482747](https://doi.org/10.1364/OE.482747).
- [41] C. E. Shannon, “Communication in the presence of noise,” *Proceedings of the IEEE*, vol. 72, no. 9, pp. 1192–1201, 1984. DOI: [10.1109/PROC.1984.12998](https://doi.org/10.1109/PROC.1984.12998).
- [42] *Shot noise*, [https://123.physics.ucdavis.edu/shot\\_files/ShotNoise.pdf](https://123.physics.ucdavis.edu/shot_files/ShotNoise.pdf), Accessed: 2024-08-04, 2017.

- [43] D. R. Spiegel *et al.*, “Shot-noise measurements of the electron charge: An undergraduate experiment,” *American Journal of Physics*, vol. 63, no. 6, pp. 554–560, Jun. 1995, ISSN: 0002-9505. DOI: [10.1119/1.17867](https://doi.org/10.1119/1.17867).
- [44] P. Welch, “The use of fast fourier transform for the estimation of power spectra: A method based on time averaging over short, modified periodograms,” *IEEE Transactions on Audio and Electroacoustics*, vol. 15, no. 2, pp. 70–73, Jun. 1967. DOI: [10.1109/TAU.1967.1161901](https://doi.org/10.1109/TAU.1967.1161901).

# Appendix

The purpose of this appendix is to offer additional context on certain topics that were considered too extensive to include in the main body of this thesis. Given that the primary focus of this thesis is experimental, theoretical aspects, including derivations and proofs, are provided here for completeness.

## Proof of Schottky's Theorem for Shot Noise

Schottky's theorem is a fundamental result in electronics, stating that the shot noise power spectral density (PSD) is proportional to the average current. This proof closely follows the approaches presented in [42], [43].

*Proof.* While current flow appears continuous, the discrete nature of charge carriers (such as electrons) leads to random arrival times at the detector, which can be modeled as a Poisson process. The current arriving at the detector at any given time can be expressed as

$$I(t) = \sum_j e\delta(t - t_j),$$

where  $t_j$  represents the random arrival times of the charge carriers. The Wiener-Khintchine theorem connects the autocorrelation function of a signal to its PSD:

$$S_x(f) = 2 \int_{-\infty}^{\infty} d\tau R_x(\tau) e^{-i2\pi f\tau} = 2\mathcal{F}(R_x(\tau))(f), \quad (4.1)$$

where the autocorrelation function is defined as

$$R_x(\tau) = \lim_{T \rightarrow \infty} \frac{1}{T} \int_{-T/2}^{T/2} dt x(t)x(t + \tau). \quad (4.2)$$

Applying this to the problem, with  $x(t) = I(t)$ , we have

$$\begin{aligned} R_{\text{shot}}(\tau) &= \lim_{T \rightarrow \infty} \frac{1}{T} \int_{-T/2}^{T/2} dt I(t)I(t + \tau) \\ &= \lim_{T \rightarrow \infty} \frac{e^2}{T} \sum_j \sum_k \int_{-T/2}^{T/2} dt \delta(t - t_j)\delta(t - t_k + \tau). \end{aligned}$$

Evaluating the integral:

$$\int_{-T/2}^{T/2} dt \delta(t - t_j) \delta(t - t_k + \tau) = \begin{cases} \delta(t_j - t_k + \tau), & \text{if } -T/2 < t_j < T/2, \\ 0, & \text{otherwise.} \end{cases}$$

This leads to

$$R_{\text{shot}}(\tau) = \lim_{T \rightarrow \infty} \frac{e^2}{T} \sum_j \sum_{\substack{k \\ -\frac{T}{2} < t_j < \frac{T}{2}}} \delta(t_j - t_k + \tau). \quad (4.3)$$

Care must be taken when evaluating this expression. For  $j = k$ , the times match, and we obtain  $\delta(\tau)$ . Assuming there are  $N$  terms for which the time constraint is satisfied, this yields a contribution of  $N\delta(\tau)$ . For  $j \neq k$ , the delta functions are randomly distributed, and with appropriate averaging, their contributions to eq. (4.3) cancel out. It is important to note, however, that this "appropriate averaging" is a non-trivial process, and therefore, it will not be elaborated upon here.

Thus, we are left with

$$R_{\text{shot}}(\tau) = N \frac{e^2}{T} \delta(\tau) = e \bar{I} \delta(\tau),$$

where  $\bar{I}$  is the average current, defined as the number of charges per unit time. The PSD is then obtained as

$$S_{\text{shot}}(f) = 2\mathcal{F}(e \bar{I} \delta(\tau))(f) = 2e \bar{I}.$$

This concludes the proof. □

It is worth noting that this result holds even if the current pulses are not modeled as delta functions but as square pulses. If the pulses have a duration  $\tau$ , the resulting PSD is given by (without proof)

$$S_{\text{shot}}(f) = 2e \bar{I} \left( \frac{\sin(\pi f \tau)}{\pi f \tau} \right)^2.$$

While this expression differs from the earlier result, it is important to consider that  $\tau$  is the mean transit time of electrons, typically on the order of 10 ps. Therefore, the cutoff frequency is  $f = 1/\tau \approx 100$  GHz, meaning that the assumption of shot noise being white noise is valid for most practical circuits.

## Modulation Instabilities

To begin the discussion, it is essential to recognize that the nonlinear coefficient,  $\gamma$ , is generally frequency-dependent, i.e.,  $\gamma = \gamma(\omega)$ . Additionally, approximating the dispersion as a polynomial truncated at the second order may not always be sufficient. This chapter closely follows the derivations and discussions in chapter 5.1 of [30]. Therefore, we start with a generalized form of the Nonlinear Schrödinger Equation (NLSE):

$$\frac{\partial \tilde{A}(\omega - \omega_0)}{\partial z} + i \left( k(\omega) - k(\omega_0) - \frac{\omega - \omega_0}{v_g(\omega_0)} \right) \tilde{A}(\omega - \omega_0) = -i\gamma(\omega) \mathcal{F}(|A|^2 A), \quad (4.4)$$

where  $v_g$  is the group velocity, and  $\omega_0$  represents the centre or envelope frequency of a pulse. Let  $\Omega = \omega - \omega_0$ . To ensure consistency in Equation 4.4, note that the term in brackets simplifies to  $\frac{k''}{2}\Omega^2$ , given that  $k' = 1/v_g$ .

Consider a continuous wave (CW) centred around  $\omega_0$ :

$$\frac{\partial \tilde{A}_{\text{cw}}}{\partial z} = -i\gamma(\omega_0) \mathcal{F}(|A_{\text{cw}}|^2 A_{\text{cw}}) = -i\gamma(\omega_0) P_0 A_{\text{cw}}, \quad (4.5)$$

where the field normalization ensures that the absolute square of the amplitude represents the power in the fibre. This leads to a nonlinear phase shift:

$$\tilde{A}_{\text{cw}}(z) = \tilde{A}_{\text{cw}}(z=0) e^{-i\gamma(\omega_0)P_0 z}.$$

Next, we express the electric field as a perturbation:

$$A(z, t) = [A_{\text{cw}} + a(z, t)] e^{-i\gamma(\omega_0)P_0 z}, \quad (4.6)$$

where the perturbation  $a(z, t)$  is small, allowing us to neglect second and higher-order terms. Substituting this into the  $|A|^2 A$  term in the NLSE gives:

$$|A|^2 A \approx (|A_{\text{cw}}|^2 A_{\text{cw}} + 2|A_{\text{cw}}|^2 a + A_{\text{cw}}^2 a^*) e^{-i\gamma(\omega_0)P_0 z}. \quad (4.7)$$

Thus, the NLSE becomes:

$$\begin{aligned} & -i\gamma(\omega_0)|A_{\text{cw}}|^2 \tilde{a}(\Omega) + \frac{\partial \tilde{a}(\Omega)}{\partial z} + iK(\Omega)\tilde{A}(\Omega) = \\ & -i\gamma(\omega_0 + \Omega) [2|A_{\text{cw}}|^2 \tilde{a}(\Omega) + A_{\text{cw}}^2 \tilde{a}(-\Omega)^*], \end{aligned} \quad (4.8)$$

where the dispersion term simplifies by defining:

$$K(\Omega) = k(\omega_0 + \Omega) - k(\omega_0) - \frac{\Omega}{v_g(\omega_0)}.$$

If  $\gamma(\omega)$  is frequency-independent, we obtain a matrix equation by substituting  $\Omega \rightarrow -\Omega$ :

$$\begin{aligned} \frac{\partial}{\partial z} \begin{bmatrix} \tilde{a}(\Omega) \\ \tilde{a}(-\Omega)^* \end{bmatrix} &= i \begin{bmatrix} -K(\Omega) & 0 \\ 0 & K(-\Omega) \end{bmatrix} \begin{bmatrix} \tilde{a}(\Omega) \\ \tilde{a}(-\Omega)^* \end{bmatrix} \\ &\quad + i\gamma P_0 \begin{bmatrix} -1 & 1 \\ 1 & 1 \end{bmatrix} \begin{bmatrix} \tilde{a}(\Omega) \\ \tilde{a}(-\Omega)^* \end{bmatrix}. \end{aligned} \quad (4.9)$$

The eigenvalues of the resulting coupling matrix indicate the gain for spectral sidebands at frequency shifts of  $\pm\Omega$ :

$$\lambda_{\pm} = \frac{i}{2} \left( K(-\Omega) - K(\Omega) \pm \sqrt{K(-\Omega) + K(\Omega)} \sqrt{4\gamma P_0 + K(-\Omega) + K(\Omega)} \right), \quad (4.10)$$

which reduces to:

$$\lambda_{\pm}^{\text{standard}} = \frac{i}{2} \left( \sqrt{\beta_2 \Omega^2} \sqrt{4\gamma P_0 + \beta_2 \Omega^2} \right), \quad (4.11)$$

in the standard case where  $K(\Omega) \approx \beta_2 \Omega^2$ . For negative group velocity dispersion (GVD) ( $\beta_2 < 0$ ), the term under the square root becomes negative until the frequency shift  $\Omega$  reaches a sufficient value. The gain and loss parts of the eigenvalues depend on  $K(\Omega) + K(-\Omega)$ , which involves only even orders of dispersion.

By defining  $\Delta k(\Omega) = K(-\Omega) + K(\Omega) = k(\omega_0 - \Omega) + k(\omega_0 + \Omega) - 2k(\omega_0)$ , we express the gain eigenvalues as:

$$\lambda_{\pm}^{\text{gain}} = \frac{1}{2} \sqrt{-4\gamma P_0 \Delta k(\Omega) - \Delta k(\Omega)^2}. \quad (4.12)$$

The parameter  $\gamma P_0$  is associated with the CW intensity, indicating the presence or absence of modulation instability gain at different frequencies. As shown in Figure 4.1, the behaviour of the modulation instabilities is characterized by the wavenumber shift and the corresponding power gain across different optical frequencies. The figure illustrates how the instabilities predominantly exhibit significant gain far from the central optical frequency of the laser, indicating that these instabilities are not relevant in the frequency range of interest.

## Autocorrelator

As pulse durations become shorter than 1 ps, which is beyond the electronic time resolution, measuring pulse width using purely electronic means becomes increasingly difficult [6]. A widely used method for characterizing ultrashort pulses is intensity autocorrelation, which employs second harmonic generation (SHG), as depicted in Figure 4.2. The following description closely follows the explanation provided in [6].

In this method, a beamsplitter divides the incident laser beam into two beams of identical intensity. One of the beam paths is delayed relative to the other by a time  $\tau$ . Both beams are then focused into a nonlinear crystal where they overlap in both space and time. Due to the nonlinear properties of the crystal, SHG occurs, generating a signal at twice the frequency of the original beam ( $2\omega$ ). The intensity of this SHG signal depends on the time delay  $\tau$  between the two pulses.

It can be shown that the SHG signal is minimal when the pulses do not overlap temporally and reaches a maximum when they are perfectly overlapped in time. Due to momentum conservation and the non-collinear configuration of the incident beams, the frequency-doubled signal appears spatially between the two original beams. An aperture can be used to isolate and measure only the SHG signal's intensity:

$$I_{2\omega}(\tau) \sim \int_{-\infty}^{\infty} |E(t)E(t+\tau)|^2 dt = \int_{-\infty}^{\infty} I(t)I(t+\tau)dt. \quad (4.13)$$

Since this intensity is symmetric with respect to the delay, i.e.,  $I_{2\omega}(\tau) = I_{2\omega}(-\tau)$ , the autocorrelation measurement cannot reveal asymmetries in the pulse. To accurately extract the pulse duration, an assumption about the pulse shape is required, as the autocorrelation trace alone does not provide detailed information about the pulse's shape or structure.

## Diagnostics Measurements

This section presents various measurements from the optical spectrum analyzer (OSA), microwave spectrum analyzer (MSA), and autocorrelator for completeness. The results are shown in Figures 4.3 to 4.6.

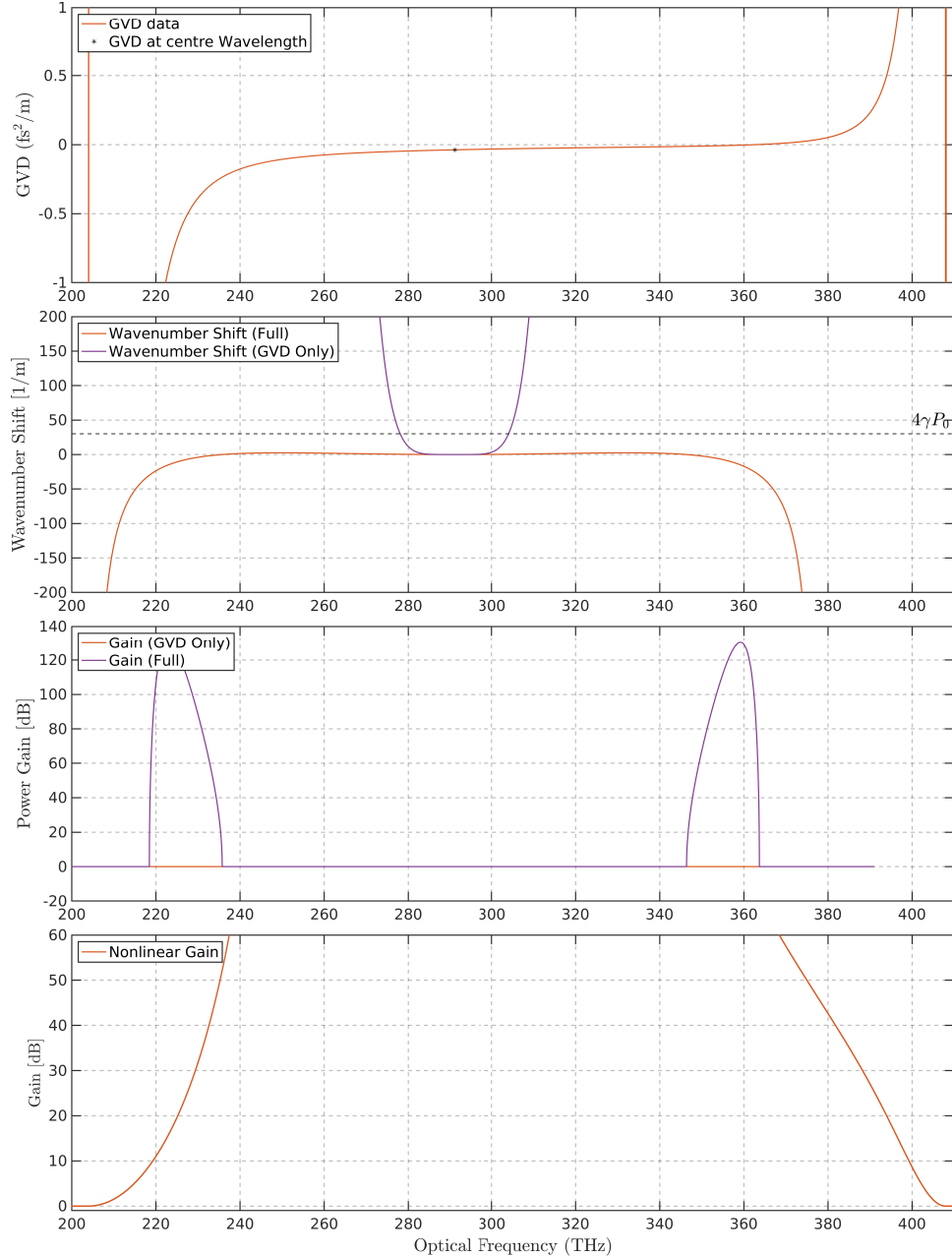


Figure 4.1: Overview of modulation instabilities in the fibre. (a) The group velocity dispersion (GVD) data shows the raw GVD values across different optical frequencies, with a marker at the centre wavelength highlighting the GVD used in calculations. (b) Wavenumber shift as a function of optical frequency, comparing the full model and the model considering only the GVD contribution. The horizontal dashed line represents the constant term  $4\gamma P_0$ . (c) Power gain in dB for the cases considering only GVD and the full model, showing significant differences away from the centre frequency. (d) Nonlinear gain across optical frequencies, illustrating the gain behaviour influenced by nonlinear effects. The x-axis is shared among all subplots, representing optical frequency in THz.

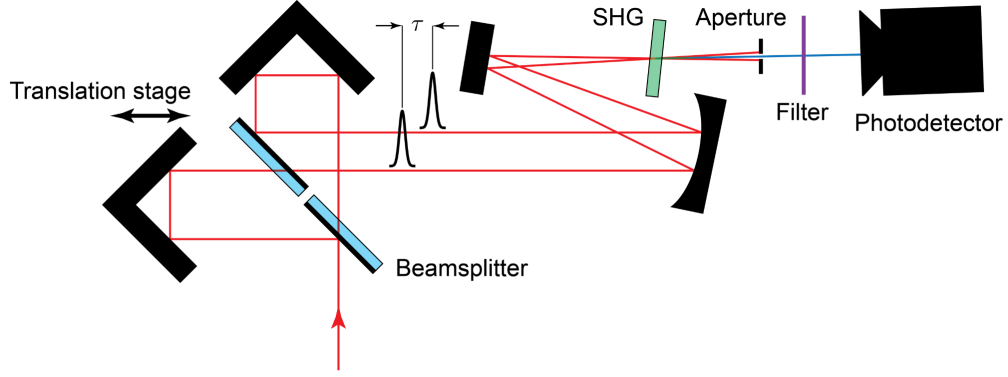


Figure 4.2: Schematic of the intensity autocorrelation setup used to measure ultrashort pulse durations [6]. The setup utilizes a beamsplitter to divide the laser beam into two identical beams with a controllable delay  $\tau$ . Both beams are focused into a nonlinear crystal to generate a second harmonic generation signal at  $2\omega$ , which depends on the temporal overlap of the pulses. An aperture is used to isolate and measure the SHG intensity, which provides information about the pulse duration.

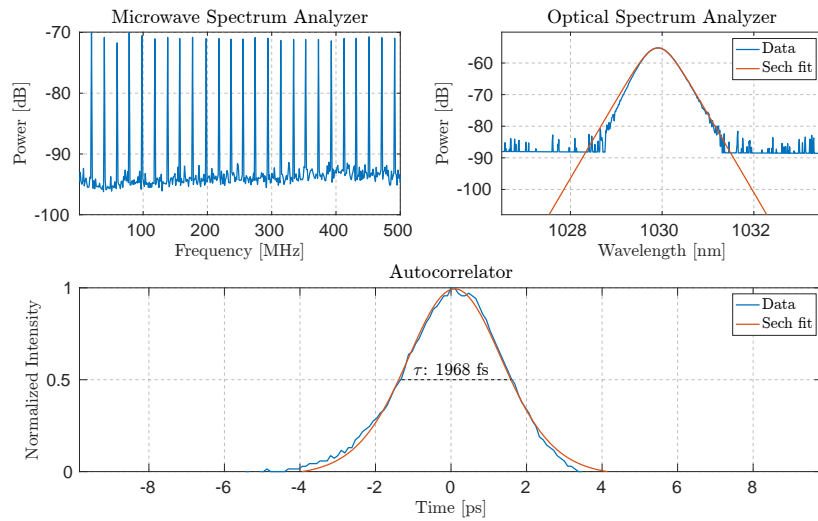


Figure 4.3: Combined diagnostic results from the microwave spectrum analyzer (MSA) with a resolution bandwidth of 3 kHz, autocorrelator, and optical spectrum analyzer (OSA). The red line indicates an ideal soliton pulse fit. Measurement performed at 132 W pump power.

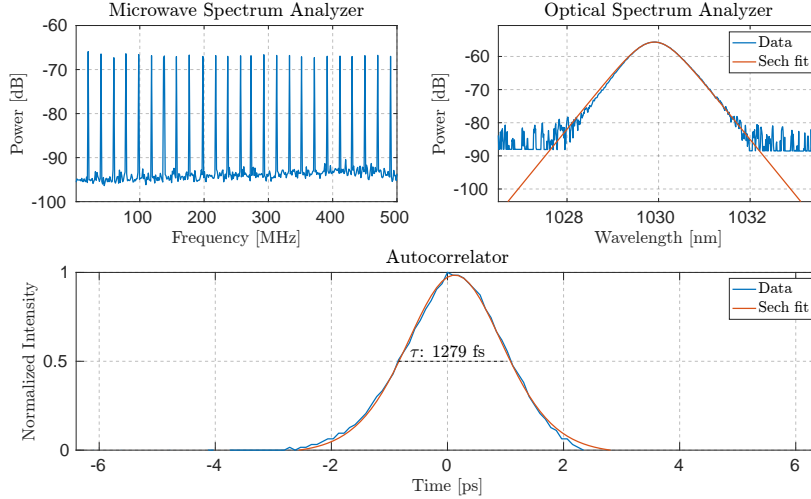


Figure 4.4: Combined diagnostic results from the microwave spectrum analyzer (MSA) with a resolution bandwidth of 3 kHz, autocorrelator, and optical spectrum analyzer (OSA). The red line indicates an ideal soliton pulse fit. Measurement performed at 173 W pump power.

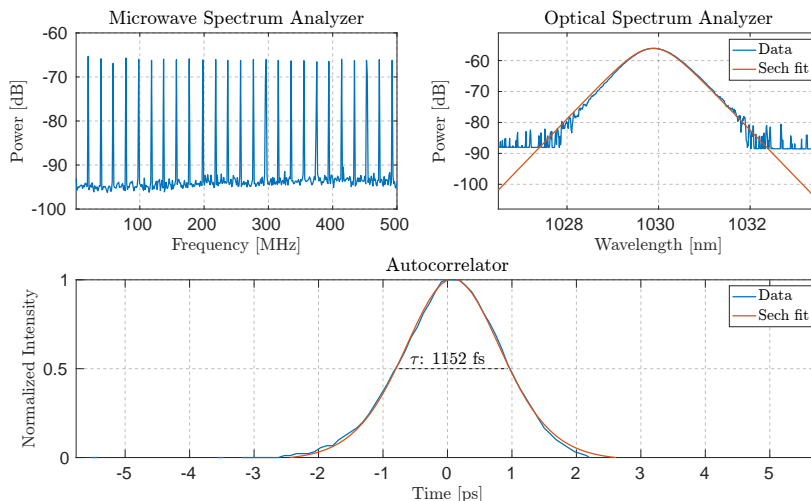


Figure 4.5: Combined diagnostic results from the microwave spectrum analyzer (MSA) with a resolution bandwidth of 3 kHz, autocorrelator, and optical spectrum analyzer (OSA). The red line indicates an ideal soliton pulse fit. Measurement performed at 191 W pump power.

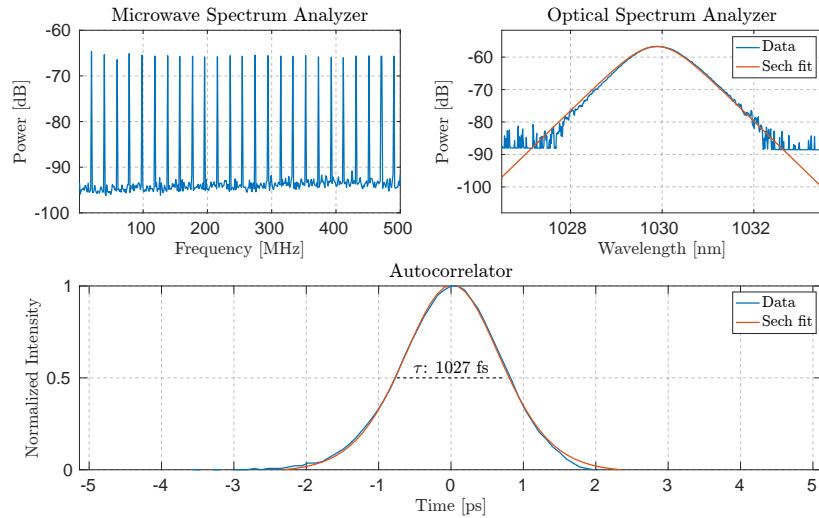


Figure 4.6: Combined diagnostic results from the microwave spectrum analyzer (MSA) with a resolution bandwidth of 3 kHz, autocorrelator, and optical spectrum analyzer (OSA). The red line indicates an ideal soliton pulse fit. Measurement performed at 214 W pump power.

## Comparison of Averaging Methods for Noise Measurements

The choice of averaging method for noise measurements, as discussed in Chapter 3.5.2, may not be immediately intuitive. Therefore, a comparison of three different averaging methods is presented here. The first method involves using a moving average with a constant number of sample points over the entire trace. For the low-frequency trace, this method uses 20 sample points, corresponding to an averaging range of 2 Hz. For the high-frequency trace, 200 sample points are used, corresponding to an averaging range of 4 kHz. While this method is sufficient to observe trends and the shot-noise-limited behavior of the laser, it introduces excessive smoothing at the low-frequency end of both traces. Moreover, the "smoothness" of the curves diminishes at higher frequencies. Even more problematic, some characteristic peaks in the high-frequency trace between 20 kHz and 100 kHz are smeared out to the point of disappearance. In contrast, the second method, which uses an increasing number of sample points, maintains consistent "smoothness" throughout the entire frequency range, preserving key characteristics of the noise curve while still allowing observation of the laser's shot-noise-limited behavior. This comparison is illustrated in Figure 4.7.

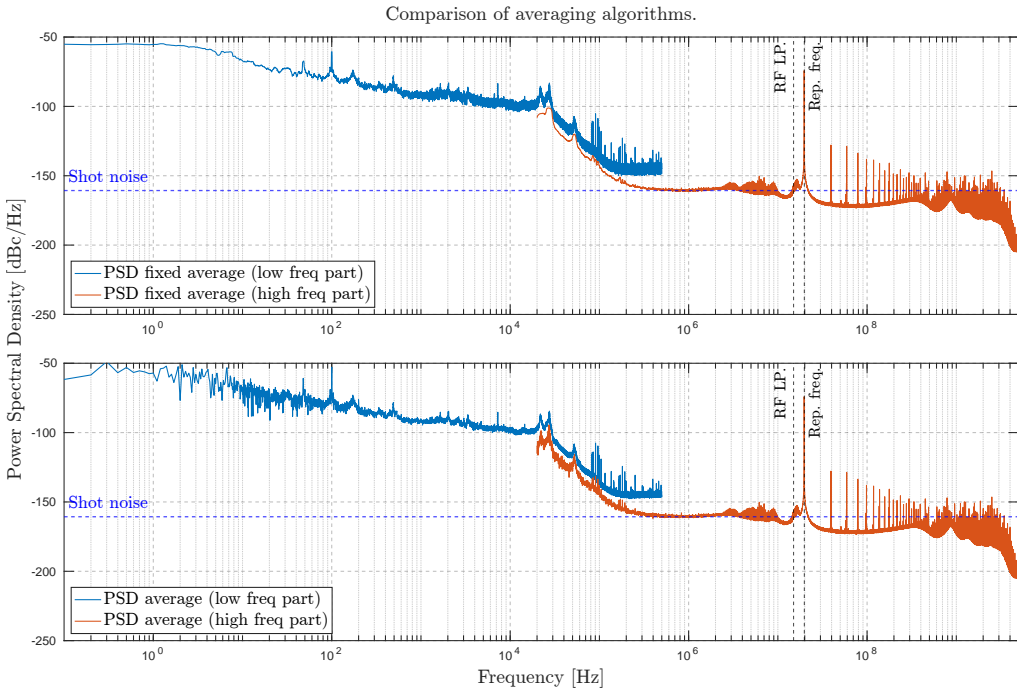


Figure 4.7: Top: Overlay of high-frequency (orange) and low-frequency (blue) traces with constant averaging. Bottom: Overlay of high-frequency (orange) and low-frequency (blue) traces with adjusted averaging as described in Chapter 3.5.2.

The next method compared is *Welch's method* for calculating the power spectral density. This method estimates the power of a signal based on periodogram spectrum estimates [44]. Welch's method utilizes the Fast Fourier Transform (FFT) to estimate power spectra by averaging modified periodograms of overlapping data segments. As shown in Figure 4.8, Welch's method divides the signal into 100 segments of equal length with 80% overlap, applies a Hanning window to each segment, computes their periodograms, and averages them to produce a smooth spectral estimate. This approach effectively reduces variance and captures noise characteristics in a non-stationary signal. [44]

Figure 4.8 compares the PSD estimates obtained using the averaging method described in Chapter 3.5.2 and Welch's method. While both methods aim to provide a stable spectral estimate, Welch's method benefits from segment averaging, which tends to smooth out fluctuations, particularly in the overlapping region. In contrast, the earlier-described method offers a good balance of detail across the entire frequency range while preserving key characteristics of the noise spectrum.

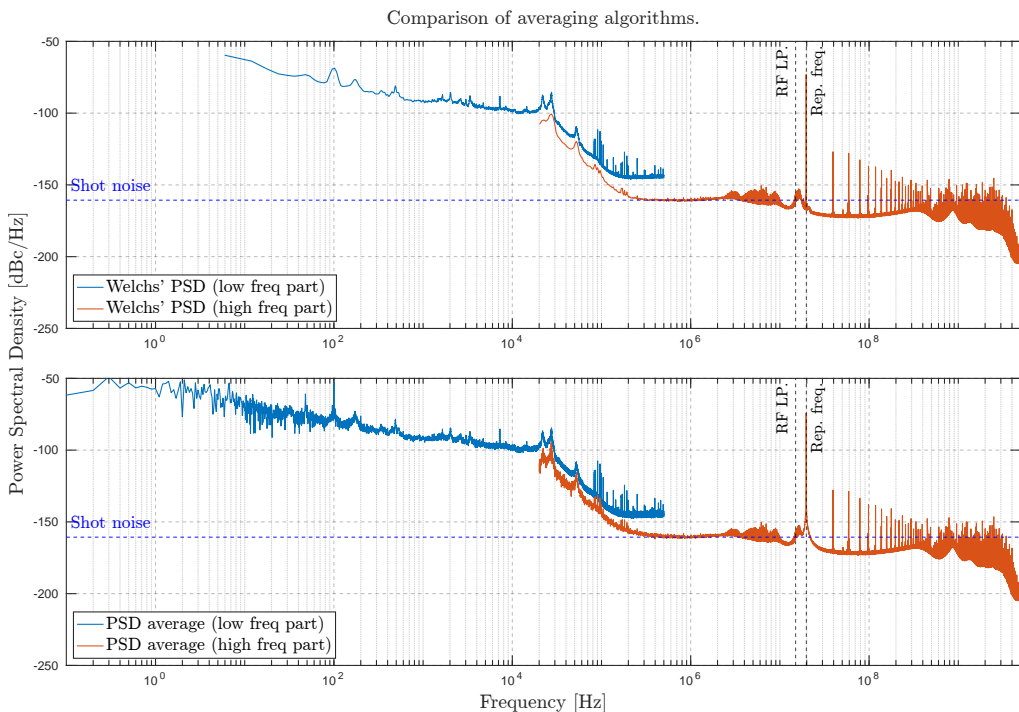


Figure 4.8: Top: Overlay of high-frequency (orange) and low-frequency (blue) traces using Welch's method to estimate the PSD of the signal, with Hanning windows applied to each of the 100 segments with 80% overlap. Bottom: Overlay of high-frequency (orange) and low-frequency (blue) traces with adjusted averaging as described in Chapter 3.5.2.

Lastly, the number of sample points used for averaging is shown in Figure 4.9 for the low-frequency part (top) and the high-frequency part (bottom). The left vertical axis represents the number of averaged sample points for each interval, while the right vertical axis indicates the corresponding frequency range. For the low-frequency measurement, the frequency vector is spaced by 0.1 Hz, resulting in a factor of 0.1 between these two axes. For the high-frequency part, where the frequency vector is spaced by 20 Hz, the factor between the axes is 20.

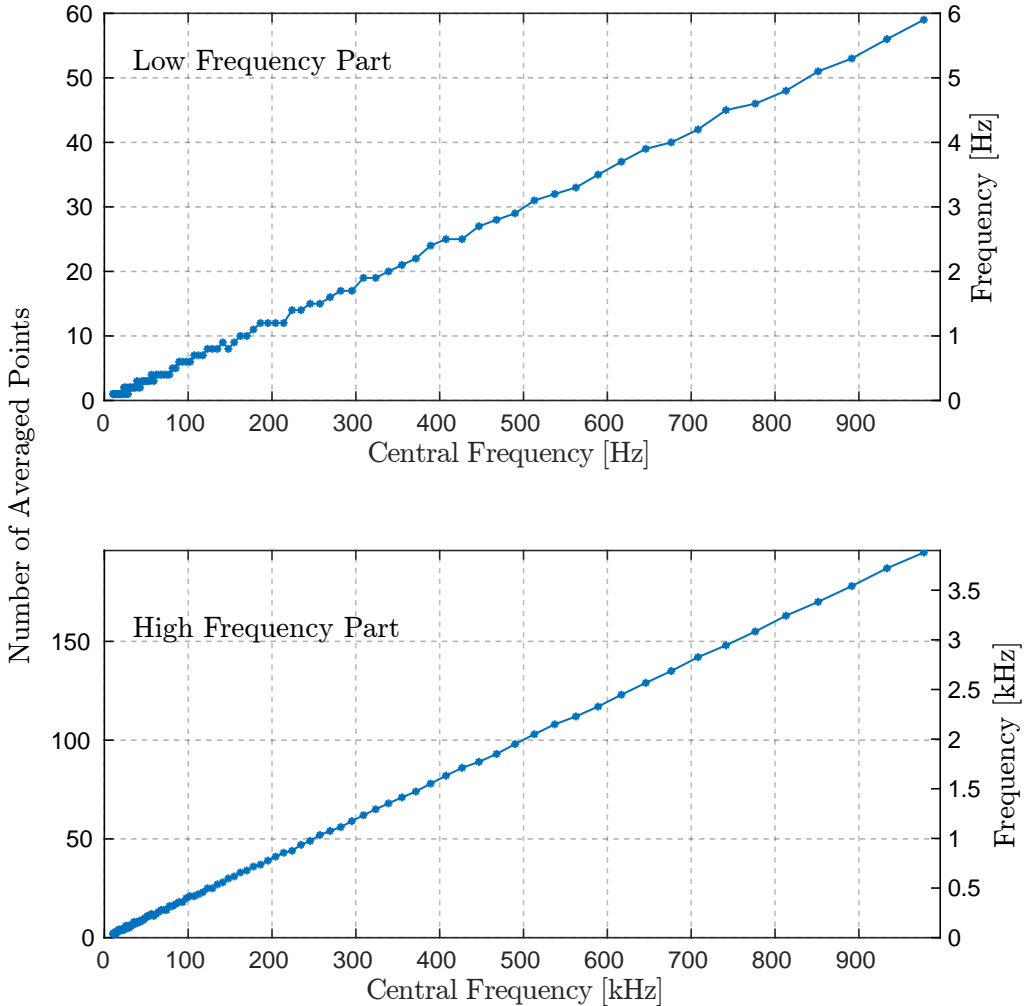


Figure 4.9: Top: Number of sample points used for averaging as a function of the central frequency for the low-frequency measurement. The right vertical axis indicates the corresponding frequency range. Bottom: Same representation for the high-frequency measurement. Settings are detailed in Chapter 3.5.2.

**Declaration of originality**

The signed declaration of originality is a component of every written paper or thesis authored during the course of studies. In consultation with the supervisor, one of the following three options must be selected:

- I confirm that I authored the work in question independently and in my own words, i.e. that no one helped me to author it. Suggestions from the supervisor regarding language and content are excepted. I used no generative artificial intelligence technologies<sup>1</sup>.
- I confirm that I authored the work in question independently and in my own words, i.e. that no one helped me to author it. Suggestions from the supervisor regarding language and content are excepted. I used and cited generative artificial intelligence technologies<sup>2</sup>.
- I confirm that I authored the work in question independently and in my own words, i.e. that no one helped me to author it. Suggestions from the supervisor regarding language and content are excepted. I used generative artificial intelligence technologies<sup>3</sup>. In consultation with the supervisor, I did not cite them.

**Title of paper or thesis:**

Shot Noise Measurements in High-Power Modelocked Thin-Disk Lasers

**Authored by:**

*If the work was compiled in a group, the names of all authors are required.*

Last name(s):

Köberlin

First name(s):

Marcel

With my signature I confirm the following:

- I have adhered to the rules set out in the Citation Guide.
- I have documented all methods, data and processes truthfully and fully.
- I have mentioned all persons who were significant facilitators of the work.

I am aware that the work may be screened electronically for originality.

Place, date

Zürich, 16.09.2024

Signature(s)

M. köberlin

<sup>1</sup> E.g. ChatGPT, DALL E 2, Google Bard

<sup>2</sup> E.g. ChatGPT, DALL E 2, Google Bard

<sup>3</sup> E.g. ChatGPT, DALL E 2, Google Bard

*If the work was compiled in a group, the names of all authors are required. Through their signatures they vouch jointly for the entire content of the written work.*